2019

Optically Transparent Antennas and Filters for Smart City Communication

Ryan B. Green

Optically Transparent Antennas and Filters for Smart City Communication

This dissertation is submitted in partial completion of the requirements for the degree of Doctor of Philosophy at Virginia Commonwealth University

by

Ryan Benjamin Green

Bachelor of Science, Electrical Engineering, Mississippi State University, 2011
Master of Science, Electrical and Computer Engineering, Mississippi State University, 2013

Director: Erdem Topsakal, Ph.D.
Professor and Chair, Department of Electrical and Computer Engineering

Committee in Charge:
Sherif Abdelwahed, Ph.D., Professor, Department of Electrical and Computer Engineering

Ibrahim Guven, Ph.D., Assistant Professor, Department of Mechanical and Nuclear Engineering

Nastassja Lewinski, Ph.D., Assistant Professor, Department of Chemical and Life Sciences Engineering

Umit Ozgur, Ph.D., Professor, Department of Electrical and Computer Engineering

Virginia Commonwealth University
Richmond, Virginia
April, 2019

Acknowledgement

First, I would like to thank my advisor, Dr. Erdem Topsakal. His help and guidance in not just my Ph.D. work, but my undergraduate, master's work, and professional development cannot be measured. Throughout my time here at VCU he has pushed me beyond my comfort zone, making me a better person in the process. I also thank him for giving me the opportunity to teach students, not just in the classroom, but also in the research team we have built here since arriving from Mississippi.

I would like to thank my committee: Dr. Abdelwahed, Dr. Guven, Dr. Lewinski, and Dr. Ozgur who have helped refine this work. Additionally, I would like to thank Dr. Lynn Secondo for reading this work and helping me refine it before the defense.

I would also like to thank those who helped explain basics of semiconductors to me and make portions of this research in the cleanroom in the College of Engineering: Mykyta Toporkov, MD Barkat Ullah, Kai Ding, Justine Drobitch, Michelle Guzman, Supapon Hia, Joshua Pitchford, Ranjita Timsina, and Jessi Shaffer. This work would have been impossible to do without your help.

I would also like to thank my colleagues here at VCU, who are too numerous to name. You all have allowed me to keep calm and cool as I have completed my four years here at VCU. You have made me feel welcome and accepted here.

I would like to thank my friends and family, both in Richmond and beyond, for their unwavering support throughout my graduate school experience. In good times and bad, my family has been there for me, offering me guidance and support in the difficult decisions I have had to make in my entire academic career.

Dedication

Soli Deo Gloria

Table of Contents

Table of Figures

Table of Tables

List of Abbreviations

AI	Artificial Inteligence
AZO	Aluminum-doped zinc oxide
cm	Centimeters
dB	Decibels
dBi	Decibels with respect to an isotropic radiator
FOM	Figure of Merit
FSS	Frequency selective surfaces
Ga	Gallium
Gbps	Giga Bits Per Second
GHz	Giga Hertz
GZO	Gallium-doped zinc oxide
Hz	Hertz
IoT	Internet of Things
ISM	Industrial Scientific and Medicine
ITO	Indium tin oxide
LTE	Long Term Evolution network
MIMO	Multiple In Multiple Out
min	Minute
mm	Millimeter
mmWave	Millimeter wavelength
nm	Nanometer
P-MBE	Plasma enhanced molecular beam epitaxy

PNA	Programmable Network Analyzer
RF	Radio frequency
s	Seconds
S	Siemens
sccm	Standard cubic centimeters per minute
TCO	Transparent Conductive Oxide
μm	Micrometer
V	Volts
W	Watts
Zn	Zinc

List of Symbols

°	Degree
A_{mesh}	Area of meshed conductor
A_{solid}	Area of solid shape
D	Directivity
E	Electric field intensity
E_i	Incident Electric field intensity
E_{mat}	Transmitted Electric field intensity in material
$E_{mat\ ref}$	Reflected Electric field intensity in material
E_r	Reflected Electric field intensity
E_T	Transmitted electric field intensity
G	Gain
G_A	Gain of Antenna array
G_E	Gain of antenna array element
G_R	Gain of receiving antenna
G_T	Gain of transmitting antenna
H_i	Incident Magnetic field intensity
H_{mat}	Transmitted Magnetic field intensity in material
$H_{mat\ ref}$	Reflected Magnetic field intensity in material
H_r	Reflected Magnetic field intensity
H_T	Transmitted magnetic field intensity
L	Length of Antenna
m*	Effective mass of electron

n	Number of elements in antenna array
N_e	Carrier concentration
P_{in}	Power supplied to the antenna terminals
P_{loss}	Power loss due to antenna efficiency
P_R	Power received
P_{rad}	Radiated power from antenna
P_T	Power transmitted
q_e	Charge of an electron
R	Resistance
R_1	Radius of reactive near field
R_2	Radius of radiating near field
R_3	Radius of far field
R_a	Resistance of antenna
R_s	Sheet Resistance
S_{11}	Scattering parameter for port 1 port 1, also known as Return Loss
S_{21}	Scattering parameter for port 2 port 1, also known as Return Loss
t	Thickness of film
T	Transparency
t_L	Thickness of lines in meshed antenna length
t_W	Thickness of lines in meshed antenna width
U	Radiation intensity
W	Width of antenna
Z_0	Characteristic impedance of transmission line

Z_G	Impedance of signal generator
Z_L	Impedance of load
α	Attenuation constant
β	Phase constant
γ	Propagation constant
Γ	Reflection coefficient
δ	Skindepth
$\Delta\varphi$	Phase shift
ε_0	Freespace permittivity
ε_{eff}	Antenna efficiency
ε_{re}	Effective permittivity
η	Characteristic impedance of material
η_0	Characteristic impedance of free space
θ	Angle from z axis in cartesian coordinate system
λ	Wavelength
μ_0	Freespace permeability
μ_e	Electron mobility
σ	Conductivity
σ_{dc}	Conductivity at direct current (f = 0 Hz)
σ_{opt}	Conductivity at optical frequency
τ	Transmission coefficient
τ_e	Electron relaxation time
φ	Angle in x-y plane in cartesian coordinate system

ω	Angular frequency
ω_p	Plasma frequency

Abstract

OPTICALLY TRANSPARENT ANTENNAS AND FILTERS FOR SMART CITY COMMUNICATION

Ryan B. Green

This dissertation is submitted in partial completion of the requirements for the degree of Doctor of Philosophy at Virginia Commonwealth University.

Virginia Commonwealth University, 2019

Director: Erdem Topsakal, Ph.D., Professor and Chair, Electrical and Computer Engineering

Incremental usage of mobile devices demand for faster data rates and more reliable coverage. A new generation of wireless networks (5G) is being explored to solve this issue and to realize the concept of smart cities. The smart city concept seeks to alleviate urban challenges including infrastructure and network capacity. The frequencies proposed for the upcoming 5G network would result in shorter broadcast distances and network dead zones. Additional access points and signal repeaters, embedded into existing infrastructure, help mitigate these issues through embedding transparent antennas into the windows by means of transparent conductive oxides (TCOs). Transparent antennas possess, however a major challenge: low gain. The technology and processes that make an opaque antenna transparent contribute to the inefficiency of the antenna via more resistive materials, thinner conductive materials, or meshing effects. These inefficiency decreases the antenna gain, limiting the efficacy of the antenna. This lower gain can be countered by means of employing antennas in an antenna array, boosting the gain and even giving the array the ability to beam form for the upcoming 5G network. One issue inherent in the smart city implementation is the large network dead zones due to scattering effects at 5G frequencies. These dead zones can be countered with strategically placed transparent reflectors

embedded into the glass surfaces of city high-rises. Using frequency selective surfaces (FSSs) for these transparent reflectors will allow for the adequate reflection of 5G frequencies while allowing for outdoor to indoor 4G LTE communication to still exist. To study the effects transparent materials have on antenna and FSS performance, three antennas and two FSSs were designed, simulated, fabricated, and measured. Each design uses gallium-doped zinc oxide (GZO) for the transparent conductive material. These antennas and frequency selective surfaces were designed to operate on various frequency bands ranging from Industrial Scientific Medicine bands (2.4 GHz ISM band and 5.8 GHz ISM band) to proposed 5G frequency bands (25-27 GHz). Furthermore, an antenna array was designed and assembled using the 5.8 GHz ISM band antennas to study the performance and efficacy of using TCOs to make an optically transparent, beamforming antenna array.

This dissertation shows there are significant effects due to the carrier concentration and film thickness on antenna and filter efficiency and resonance strength. If the conductivity of the film is too low or if the thickness is too low, electromagnetic devices will not possess a resonance. However, if the film thickness is too thick, the transparency diminishes. This dissertation proposes a figure of merit model for both TCO antennas and TCO filters. A 4x1 GZO antenna array was constructed to operate at 5.8 GHz (ISM band), and the results show approximately 10dBi of lower aperture gain between a copper version of the array and the GZO version of the array. However, the 4x1 GZO array shows an approximate 12dBi increase in gain over a single GZO antenna element.

The technology developed in this dissertation has a broader impact other than for smart cities and the upcoming 5G network. Transparent antenna arrays offer sight insensitive military communication systems, keeping the communication network safer from jamming and spoofing

from an enemy combatant. Additionally, transparent antennas can also be used in eye-worn medical and commercial devices to monitor eye health and other various health signs.

Chapter 1: Smart Cities, Internet of Things, and Optically Transparent Antennas and Filters

1.1. Introduction

A new generation of wireless networks has been proposed to offer Gigabits of data in seconds and better network coverage. With the growing usage of wireless devices and smart devices, this new network is quickly turning from proposal to large market demand. 5G, the fifth generation of wireless networks, seeks to solve these problems and to bring about the concept of smart cities. There are several definitions of the term "smart city". One definition is that a smart city observes and manages the use and condition of city infrastructure to better optimize the distribution of resources, maintenance, security, and services provided [1]. Infrastructure, in this definition, includes transportation infrastructure (roads, bridges, airports, subways, etc.), communication networks, and resource distribution infrastructure (water, power, etc.) Another definition is the connection of physical, information technology, economic, and social infrastructures to use the collective intelligence garnered to benefit the community [2]. According to both definitions smart cities seek to alleviate several of the infrastructural and economic challenges (including efficient use of roads, power grid, and communication networks) through the implementation of artificial intelligence (AI), data analytics, and wireless technology. Some examples of smart city initiatives being rolled out include the research into self-driving cars and smart traffic signals that use sensors and AI to more efficiently manage automotive and pedestrian

traffic. Some concepts of a smart city include better management and access to alternative transportation methods (e.g. public use bicycles, busses, and trains, etc.) using wireless technology [3] [4]. Additionally, a smart city seeks to implement new services that makes the standard of living better for those living in a city, including smart transportation [5] [6], smart environment, and smart education [4].

Smart cities will be realized as an application of the Internet of Things (IoT), a network of interconnected wireless devices ranging from smart devices to cars and appliances, on a city level. This rollout of smart city services will require infrastructural upgrades including additional sensors for traffic flow and power usage, additional data storage and analysis facilities, as well as an upgraded wireless network. This increased dependence on wireless technology will lead to greater network and internet usage than already exist. To begin addressing these issues, 5G is anticipated to provide larger data speeds and channel access necessary to have a smart city.

The 5G network will utilize frequencies between 20 GHz and 300 GHz [7] [8]. While these higher frequencies allow download speeds as high as 20 Gbps [7], they also bring challenges to providing reliable geographical coverage. As the frequency increases, the broadcast distances decreases due to signal attenuation. Shorter broadcast distances and signal scattering effects will necessarily be counteracted through more base stations and network access points per capita geographically than the current LTE network has. As a result, there will be more and more communication infrastructure (towers, antennas, amplifiers, etc.) needed for the 5G rollout. This extra equipment needed for 5G runs into another challenge: placement. Because of the increased density of access points, finding locations able to facilitate more network towers and stations becomes a challenge. As a result infrastructure has to be constructed, integrated into existing towers, and integrated into other existing structures (light posts, buildings, etc.). Because the use

of existing infrastructure is optimal, another thing to consider is the aesthetic effect these base stations have. While antenna towers are necessary for broadcast, their presence is considered a detriment to the look of the area and even property values are affected by cell towers nearby. Disguising cellular base stations into existing urban, suburban, and rural environments have been a method for a long time. Figure 1 shows common methods to hide antennas from the public. Methods include disguising these radiating elements to resemble trees [9], placing a camouflaging pattern on them, or even building a structure around them to hide the base station's shape.

Figure 1 Cellular network base stations disguised to either blend in with the environment or meet city ordinances (a) Cellular network antenna with brick camouflaging pattern [10], (b) Cellular network antenna disguised to look like a tree, (c) Cellular network antenna covered with brick patterned material to look like a stone obelisk to meet city and county ordinances on building exteriors [11].

For urban environments, one method to disguise 5G antennas is to make them transparent and incorporate both antenna and circuitry into the glass. Optically transparent antennas are not a new form of research. Transparent antennas were once considered for satellite and automotive

communication as early as the 1990s, but recently the concept has garnered new attention in the realm of smart city communication and medical telemetry.

Transparent antennas not only answer aesthetic concerns, but can also be used to help mitigate other challenges inherent to a 5G implementation using mmWave frequencies. First, a major challenge is the communication between outdoor base stations and indoor end users. At these wavelengths, the 5G signal will be susceptible to higher reflection and higher scattering effects [12]. This yields a smaller signal intensity indoors from an outdoor access point. Shown in Figure 2(a), the incoming signal is almost entirely reflected or scattered when the wave encounters a building. Only a small portion of the incoming wave is transmitted through the window, and in many cases, the signal quality is not high enough for consumer electronics to receive effectively. Using a 5G signal booster (Figure 2(b)) can alleviate the poor signal quality of outdoor to indoor communication. A 5G signal booster utilizes a window mounted antenna that takes the incoming signal from the base station, amplifies it, and rebroadcasts it within the indoor space. Similarly, the signal booster will take a 5G signal from an end user and rebroadcast this signal on the window mounted antenna to the base station outside. Signal boosters are not new and have been used for boosting weak television, Wi-Fi, and 4G LTE signals. However the need for signal boosting will be a more common occurrence due to 1) the pervasiveness of the reflection and scattering at mmWave frequencies and 2) older buildings unable to upgrade the communications infrastructure to allow 5G speeds to come through coaxial wall outlets. As a result of this pervasiveness, optical transparency of the window mounted antenna is an attractive option for retrofitting existing buildings to be 5G friendly.

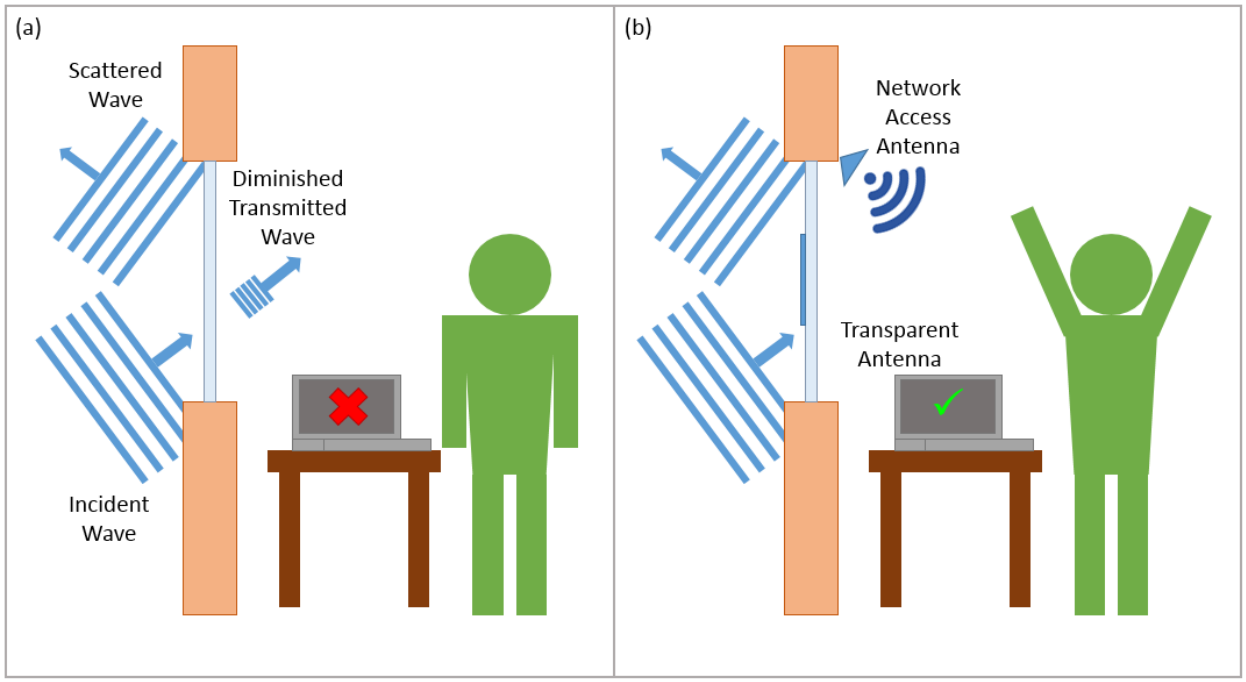

Figure 2 5G signal repeater for outdoor to indoor communication. (a) Outdoor 5G signals are scattered at the boundary of the building. The transmitted wave into the room is too low to have a 5G enabled device to operate on the network. (b) Outdoor 5G signal is being received by optically transparent antenna and rebroadcast into the room. The newly transmitted wave is strong enough to have 5G enabled device to operate on the network.

While the transmitted signal from outdoor to indoor may be too small for consumer electronics to adequately receive and demodulate, better reception technology (more expensive than what is economical for consumer electronics) in the hands of one with malicious intentions can still receive the signal. These problems are more prevalent in areas that need wireless network security, such as classified sensitive information technology or hospitals (Figure 3). In such circumstances, optically transparent conductors can be used to create frequency selective surfaces that can provide private network security while allowing other network usage [13] - [16]. For example, one area where 5G could make great impact is within the area of medical devices and medical telemetry. Creating an IoT network in a hospital provides doctors, nurses, and patients' better control and monitoring of vital medical sensors and also provides better care in the case where an issue arises. The 5G network is a perfect candidate for a private medical wireless network within a hospital, clinic, or nursing home. However, if someone with malicious intent was to use

a high grade receiver, medical data can be collected. Moreover, another could use a spoofer or jammer to violate the security of the private network. However, for visitors or the patient with a personal device, the access to another internet enabled wireless network would be beneficial. To mitigate this concern while allowing other network access, an optically transparent frequency selective surface (FSS or filter) can be used to block incoming 5G signals through the window, stop outgoing 5G signals from leaving the room, and allow other network access.

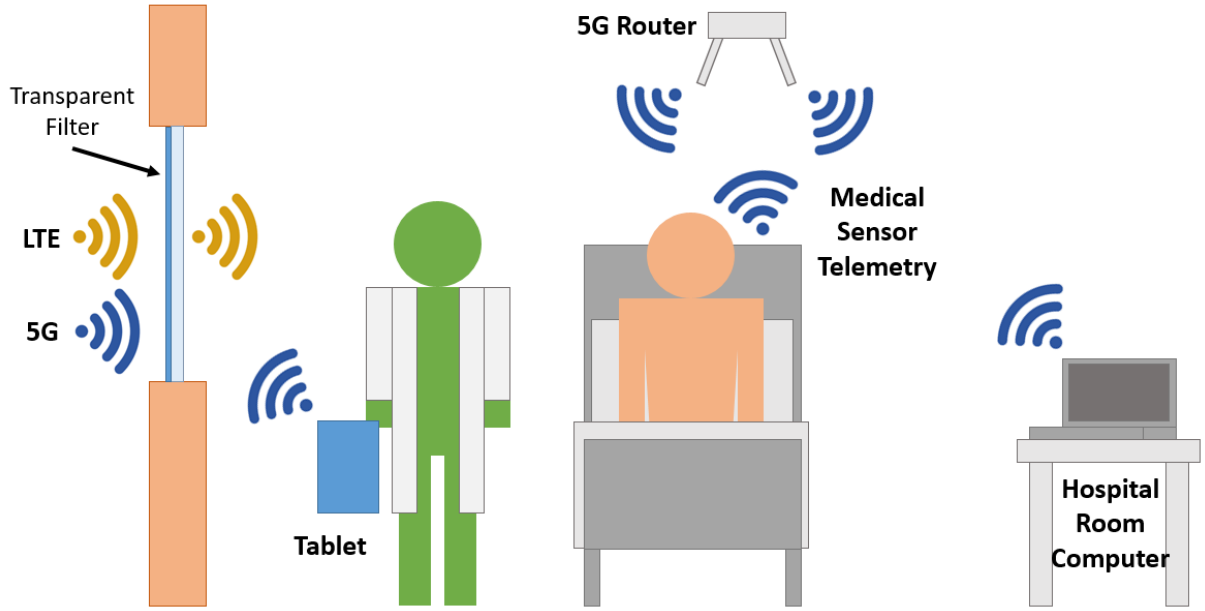

Figure 3 5G band stop filter applied to hospital room windows. External and internal 5G signals not allowed to transmit through the window while other communication protocols (4G LTE) are allowed to. This allows medical sensors on a private 5G network within the hospital to operate while allowing other communications networks into the room that are not utilizing 5G frequencies.

The last potential challenge discussed here is the communication network dead zones created in the initial rollout of the 5G network. In its first implementation, the 5G network will more than likely have base stations in strategic locations to allow for the most coverage in a city. However, not all base stations and access points will be built at the same time to provide consistent coverage. A more practical solution is to build the 5G network piece by piece as it become profitable to implement the network in certain parts of the city. Furthermore, the first rollout of 5G will more than likely use traditional looking base stations with either digital antenna arrays or

Multiple in Multiple out (MIMO) antennas on cellular towers to initially keep installation costs by telecommunication companies to a minimum. This method of installation will result in inconsistent geographical coverage due to both the physical distance from a base station, or network dead zones caused by the reflection and scattering effects (Figure 4 (a)). In the second or third phases of network rollout, certain buildings can act as signal repeaters, network access points, or base stations. If strategically picked for having both a geographical advantageous location and having a large amount of glass exteriors, optically transparent antennas can be used as an aesthetically neutral way of removing access to dead zones.

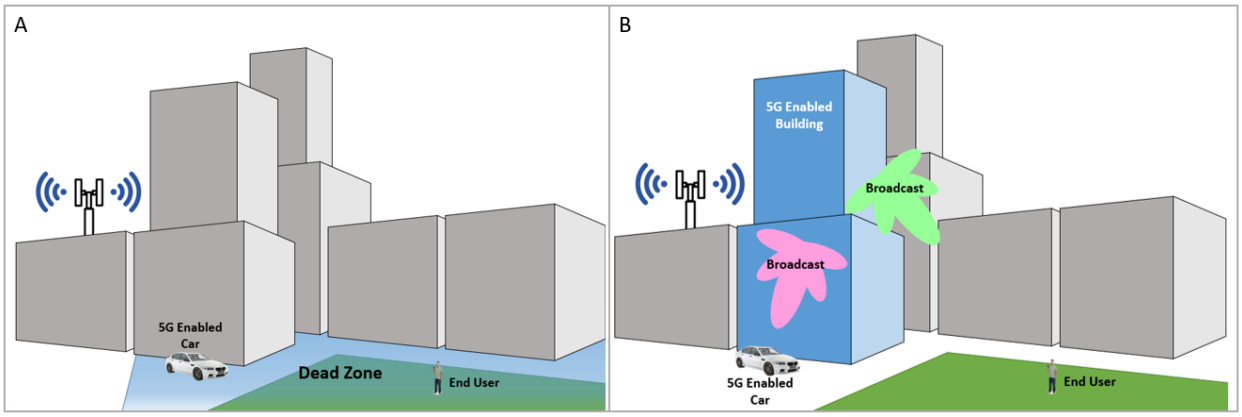

Figure 4 5G base station and end user (a) Potential dead zone created when building is between base station and end user. (b) Building signal repeater establishing network access to end users in previous dead zone.

While the benefit of transparent antennas is notable for the upcoming 5G network and 5G network, there is a major bottleneck with transparent antennas. This bottleneck is the antenna efficiency inherent in transparent antennas. Because transparent antennas are fabricated from either a meshed conductor or thin conducting films, the added conductor losses cause these antennas to be more inefficient than their opaque counterparts. As a result, the antenna gain for transparent antennas suffer. One method to counter lower antenna gain is by use of an antenna array, a periodic structure where antennas are placed in a pattern to boost signal quality, antenna gain, and beam forming. While this concept of a transparent antenna array has been explored in

the context of transparent meshed antennas, a beam steerable antenna array made from transparent conducting films has not been explored.

1.2. Research Questions, Specific Aims, and Overview of Work

Because transparent conducting films have not been explored in the context of an antenna array, this dissertation seeks to answer the following questions.

Research Questions:

1. How do the material properties (thickness and carrier concentration) of transparent conducting oxides effect the resonant frequency, gain, and efficiency of an antenna?
2. How do the material properties (thickness and carrier concentration) of transparent conducting oxides effect the aperture gain of an antenna of an antenna array?
3. How do the material properties of transparent conducting oxides effect the performance of frequency selective surfaces?

This dissertation examines these questions by design, simulation, and fabrication of various antennas and filters using highly gallium-doped zinc oxide (GZO) thin films. To do this, the following specific aims have been identified and investigated.

1. Design, simulate, and fabricate three antenna topologies out of GZO. Simulate the antenna performance for each topology for various changes in carrier concentration and film thickness.
2. Design, simulate, and fabricate a 4 by 1 antenna array out of one antenna topology investigated in Aim 1. Perform beamforming scans at various beam angles.
3. Design, simulate, and fabricate a band-stop and band-pass frequency selective surface and characterize their performance.

To meet the goals of the specific aims to answer these research questions, this dissertation presents the study, design, fabrication of optically transparent electromagnetic devices. The remaining chapters will discuss the background of optically transparent conductive films and their prior use in antennas (Chapter 2), the design, fabrication and comparison of three antenna designs made of highly doped gallium-doped zinc oxide (Chapter 3), the design, fabrication, and operation of periodic structure, including frequency selective surfaces and antenna array, made of highly doped gallium-doped zinc oxide (Chapter 4), and a discussion of transparent conductive oxides as a viable material for transparent electromagnetic devices (Chapter 5).

Chapter 2: A Brief Background on Optically Transparent Antennas

2.1. Introduction

The development of transparent antennas was initially motivated by the need for transparent windshield-embedded antennas to provide radio reception and even wireless mobile network access to automobiles without the need of a traditional hood mounted monopole antenna or roof mounted antenna [17]. Utilizing the windshield would not hinder the automobile aerodynamically or aesthetically, and provide radio and network access. Another emerging application of the transparent antennas is solar cell integration for satellite communication [18]. A major innovation in satellite technology, the CubeSat, garnered immense interest from researchers. The CubeSat is a small satellite chassis (for 1U CubeSat, the size is $10\times10\times10$ cm^3) [19], whose small size requires innovative approaches to optimize onboard power, communication, and sensory systems. Logically, one of the innovations was to install transparent antennas overlaid on the solar panel to allow maximum power harvesting while providing reliable satellite to ground communications and reducing the payload.

Due to the demands for high optical transparency, two major designs have emerged for transparent antennas, meshed and thin film antennas, as discussed below.

2.2. Meshed Antennas

Meshed antennas are fabricated using traditional metal-based conductors (copper, silver, etc.) with patterned holes or gaps within the antenna topology allowing light to transmit through the gaps (see Figure 5). Topologies explored for meshed transparency include meshed patches with solid ground planes [18] [20] – [26], meshed patches with meshed ground planes [17] [22] [26] – [30], planar monopoles [31] – [33], and coplanar topologies [34] [35] among many others. In most cases, the meshed antenna takes traditional topologies with the conductor meshed to desired transparency. However, the meshed antenna performance (gain, return loss, efficiency) differs from that of its solid counterpart, and therefore, there is a tradeoff between antenna performance and meshing characteristics performed in order to make the antenna transparent.

The first tradeoff in performance is associated with antenna gain. The meshing of a rectangular patch is shown in Figure 6 In this model, meshing consists of M number of lines of thickness t_W along one of the axes of the patch and N number of lines of thickness t_L along the other axis.

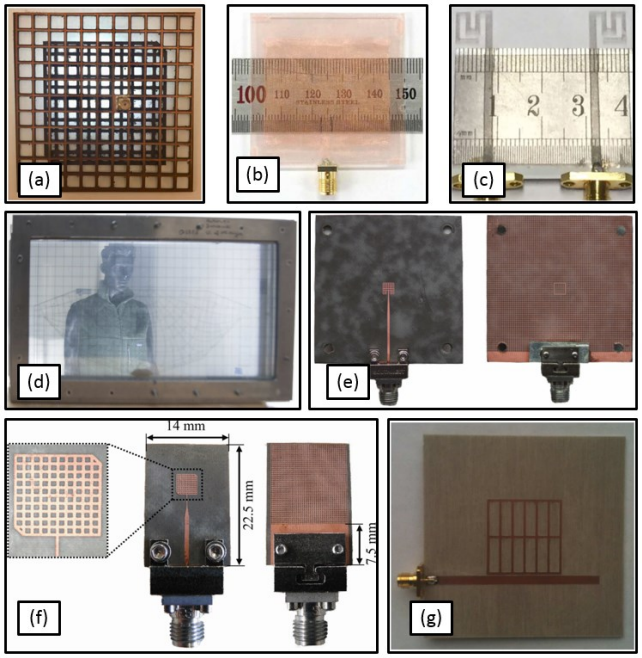

Figure 5 Meshed Antennas for Solar Cell and Window Integration. (a) Meshed patch antenna (conductor, ground, and substrate) for L1 band CubeSat applications [36] (b) Meshed patch antenna for WLAN band [37] (c) Micro-metal mesh MIMO antenna [38] (d) Meshed Monopole antenna for UHF communication [32] (e) Rectangular Meshed Patch antenna for 24 GHz [28] (f) Circularly Polarized Rectangular Meshed Patch antenna for 24 GHz [23](g) Single element proximity fed meshed patch antenna for 2.45 GHz [39].

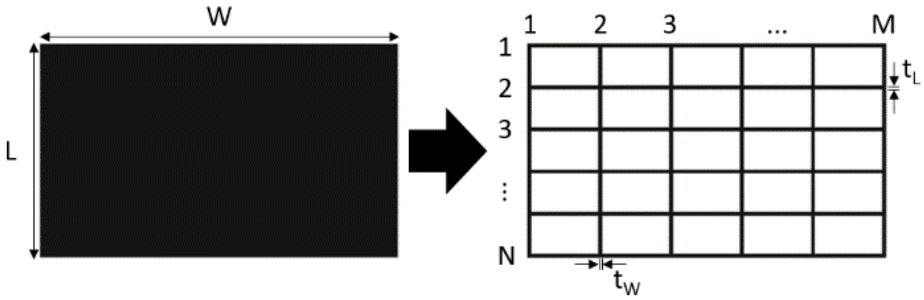

Figure 6 Rectangular Patch and Rectangular Meshed Patch.

The transparency of a mesh antenna can be calculated as the ratio of the difference in areas between the solid shape A_{solid} and the meshed conductor A_{mesh} to the area of the solid shape. In the case of a uniform rectangular mesh, the transparency is dependent on the line thicknesses t_W and t_L [8] [18]:

$$T = \frac{A_{Solid} - A_{Mesh}}{A_{Solid}} = \frac{L \cdot W - L \cdot M \cdot t_W - W \cdot N \cdot t_L + M \cdot N \cdot t_L \cdot t_W}{L \cdot W}. \quad (2.1)$$

As the transparency of a rectangular patch increases, the gain of the antenna decreases. Yasin et al. [40] fabricated several copper patch antennas (45mm × 37 mm) with various transparencies. The gain of the solid antenna was 7.32 dBi. As the transparency increased from 70% to 95%, the measured gain decreased from 6.52 dBi to 4.90 dBi; therefore, the decrease in gain was 0.80 dBi and 2.42 dBi for 70% and 95% transparency, respectively. Similar results were obtained by Arellano [24]for a coplanar fed rectangular patch. In his study, the increase of transparency from 94% to 94.8% resulted in a gain degradation from approximately 4.7 dBi to 4.1 dBi. Arellano [24] also reported that the antenna efficiency decreased from about 60% to 56%.

Another tradeoff for meshed antennas is in the resonant frequency [22] [28]. Clasen and Langley [22] studied this relationship for a solid patch antenna radiating at 1.48 GHz. The antenna was then meshed to various transparencies ranging from approximately 10% to 75%. It was found that the 10% transparency shifted the resonant frequency to 1.46 GHz, and at 75% the resonant frequency decreased further to 1.25 GHz. This study indicates that the relationship between the transparency and resonant frequency is not linear. As a result, the increased transparency of an antenna requires smaller antenna footprints to remain at the required resonant frequency.

2.3. Thin Film Antennas

Unlike meshed antennas, thin film antennas owe their transparency to the materials that have high optical transparency and low electrical resistivity. There is a large variety of the materials used for thin film antennas, including conductive inks, conductive polymers, such as silver coated polyester film (AgHT) [41] – [46], and transparent conductive oxides (TCOs). The TCOs, including indium doped tin oxide (ITO), Al-doped ZnO (AZO), and Ga-doped ZnO (GZO), show great promise as materials for transparent antennas due to their relatively low resistivity (of

the order of 10^{-4} Ω cm) and high transparency (85%-90% and higher) in the visible range [47]. ITO, the most common TCO used worldwide in flat-screen monitors, light-emitting diodes, and photovoltaic devices [48] , has found application as a material for transparent antennas [41] [49] – [59]. Although ITO is an excellent transparent conductor [60] [61], indium shortages are expected in the very near future. The prices of indium increased 27% between 2010 and 2014 [62], which fueled the search for alternative materials. AZO and GZO are considered to be the most promising candidates due to their high optical transparency and low resistivity, comparable to those of ITO [63] – [71].

Table 1 lists physical properties of ITO, AZO, and GZO films. The conductivity of a TCO at a frequency (ω) is determined by equation (2.2). In this equation, N_e is the carrier concentration, q_e is the charge of an electron, τ_e is the electron relaxation time, and m^* is the effective mass of an electron. The direct current conductivity (σ_{dc}) is determined by equation (2.3) where μ_e is the electron mobility. Table 1 shows the properties of the most conductive ITO, AZO, and GZO films grown.

$$\sigma = \frac{N_e q_e^2 \tau_e}{m^*} \frac{1}{1+j\omega\tau_e} \tag{2.2}$$

$$\sigma_{dc} = N_e \mu_e q \tag{2.3}$$

Table 1 Physical properties of highly conductive TCOs.

Property	ITO	AZO	GZO
N_e (cm^{-3})	13.8×10^{20} [60]	15×10^{20} [63]	14.6×10^{20} [65]
μ_e ($cm^2/V\cdot s$)	53.5 [60]	47.6 [63]	31 [65]
σ_{dc} (S/m)	1.18×10^6 [60]	1.14×10^6 [60]	1.23×10^6 [65]
Band gap (eV)	3.78-3.80 [61]	3.51-3.86 [64]	3.51 [65]
Transmittance in the visible range (%)	>80% [60]	>88% [63]	>90% [65]
m*	$0.35\cdot m_0$ [72]	$0.24\cdot m_0$ [64]	$0.31\cdot m_0$ [65]
ε_∞	4.0 [72]	-	4.0 [73]
τ_e (sec)	3.30×10^{-15} [60]	-	2.56×10^{-14} [73]

Very recently, optically transparent antennas based on both AZO [74] and GZO [75] have been demonstrated. Among these demonstrations, AZO antennas were fabricated to operate at 11 and 45 GHz, and a GZO antenna operated at 2.4 GHz. The popular topologies explored for thin film antennas include patches [42] [59], coplanar patches [41] [44] [45] [74] [76], dipoles [75] [77] [78], bowties [79], monopoles [52] [56] – [58], PIFA [80], and slots [53]. A variety of topologies are shown in Figure 7.

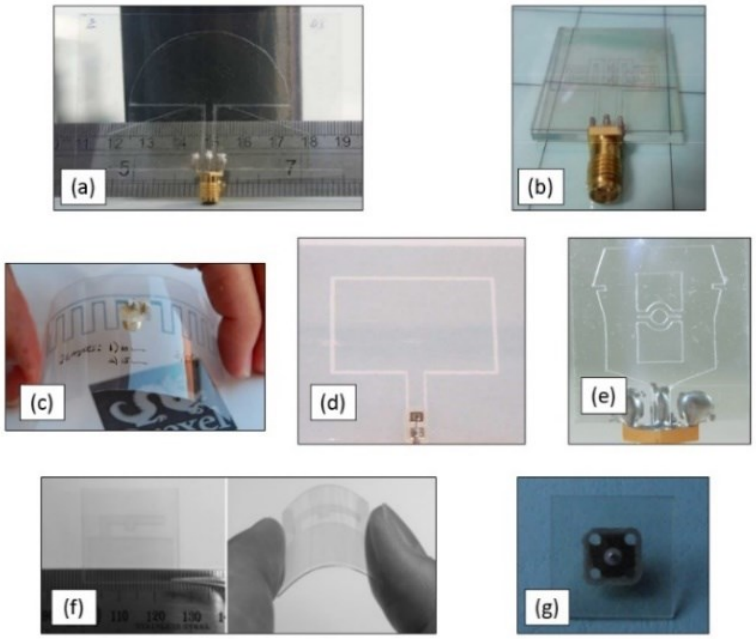

Figure 7 Thin film antennas for various applications. (a) Coplanar waveguide fed AgHT-8 monopole antenna for 3GHz-7GHz [44] (b) Coplanar waveguide fed dual band antenna for 2.4GHz and 5.8 GHz [76] (c) Meandering Dipole polymer antenna for 900 MHz [81] (d) Coplanar waveguide fed AgHT-4 patch antenna for 2.2 GHz [41] (e) Coplanar waveguide fed AgHT-8 monopole antenna for 2GHz-9GHz [45] (f) IZTO/Ag/IZTO planar inverted-F antenna for 5.2 GHz [80] (g) Rectangular Patch ITO antenna for 9.85 GHz [78].

For antenna application, the TCO film should be thin enough to be transparent in the visible range and thick enough to operate efficiently in the microwave range. It should be noted that optical properties of a material depend on the wavelength of light. At frequencies higher than the plasma frequency ω_p, the material is a transparent dielectric, since electrons cannot respond to fast electromagnetic oscillations. At frequencies lower than ω_p, a material behaves as a metal. Plasma frequency is defined as

$$\omega_p = \sqrt{\frac{N_e q_e^2}{\varepsilon_\infty \varepsilon_0 m^*} - \frac{1}{{\tau_e}^2}} \tag{2.4}$$

where N_e is the electron concentration, q_e is the electron charge, ε_∞ is the high-frequency dielectric constant, ε_0 is the dielectric permittivity of vacuum, m^* is the electron effective mass, and τ_e is the

electron relaxation time. For the most transparent conducting oxides, the plasma frequency falls in the near-infrared range (λ = 0.78 μm to 2.5 μm) [82]. At frequencies much lower than the plasma frequency, the conductivity can be calculated by equation (2.3). As seen from Figure 8, showing typical conductivity of TCOs as a function of wavelength for a wide spectral range [83], TCOs are transparent insulators in the visual spectrum, due to their low conductivity at optical frequencies. For this reason, TCO films of few micrometers in thickness offer sufficient transparency for visible light.

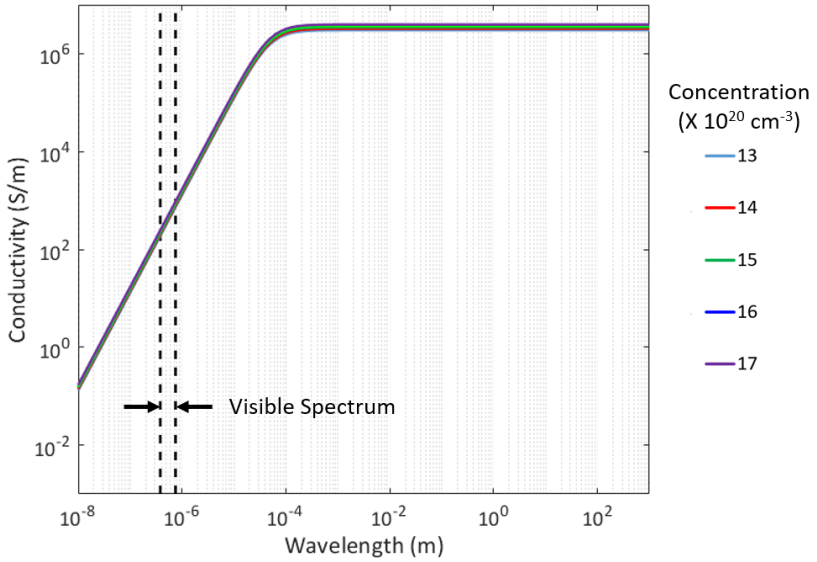

Figure 8 A typical transparent conducting oxide conductivity as a function of wavelength for frequencies ranging from the ultra violet through the microwave regime.

The optical transparency T reduces exponentially as the film thickness t increases according to the formula,

$$T(\omega,t) \cong e^{\frac{-t}{\delta}} = e^{-\alpha t} \tag{2.5}$$

where δ is the skin depth, and α is the absorption coefficient (Note: This transparency does not include the surface reflection losses of the material). The skin depth for optical wavelengths is determined below in equation (2.6). In this equation m^* is the effective mass of an electron, ε_∞ is

the high frequency permittivity of the material, ω is the optical frequency ($\omega = 2\pi f$), τ_e is the electron relaxation time, q_e is the charge of an electron, and N_e is the carrier concentration.

$$\delta \approx \frac{2m^*\sqrt{\varepsilon_\infty}}{377q_e^2}\frac{\omega^2\tau_e}{N_e}. \tag{2.6}$$

The absorption coefficients for ITO and doped zinc-oxide films are similar and thus yield comparable transparency levels. Figure 9 shows a comparison of GZO and ITO transparency versus film thickness. The thickness dependences of the optical transparency are calculated for ITO and GZO using carrier concentration values between 1×10^{20} cm^{-3} to 5×10^{20} cm^{-3}, using the mobility of 55.3 cm^2 for ITO and 31 cm^2 for GZO, effective electron mass of $0.35\cdot m_0$ for ITO and $0.31\cdot m_0$, for GZO, and the relaxation time of 3.30x10^{-15} seconds for ITO and 2.56x10^{-14} for GZO (from Table 1).

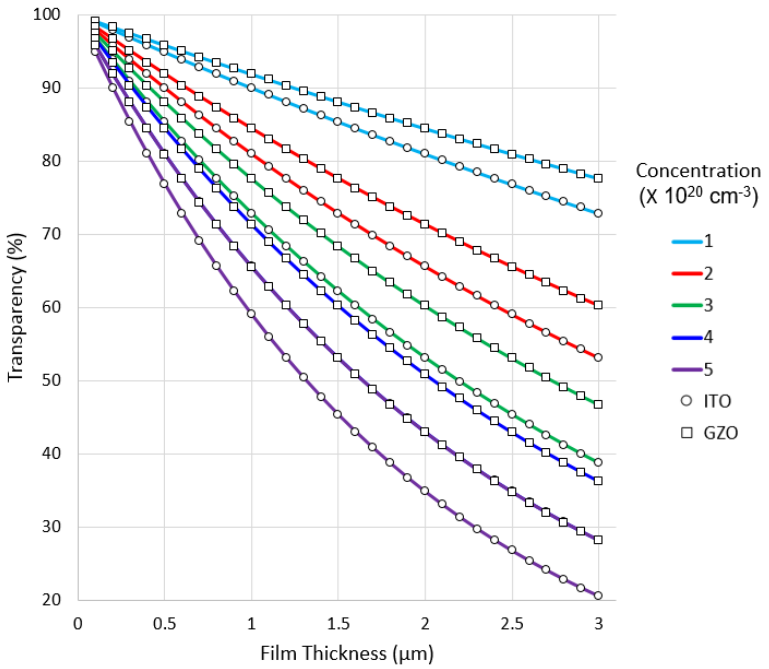

Figure 9 Transparency of ITO and GZO films versus film thickness for various carrier concentrations (N_e) at 500nm wavelength of light.

Because concentration affects both transparency and conductivity, understanding the relationship between the transparency and conductivity is important. Below in Figure 10, the

transparency of a TCO is shown over varying film thicknesses and conductivities. As shown, the transparency decreases as the film thickness increases. On the other hand, to perform efficiently in the microwave range, the film thickness should comprise at least several skin depths. If the frequency of electromagnetic wave ω is below ω_p, the skin depth is given as (2.7) [84]

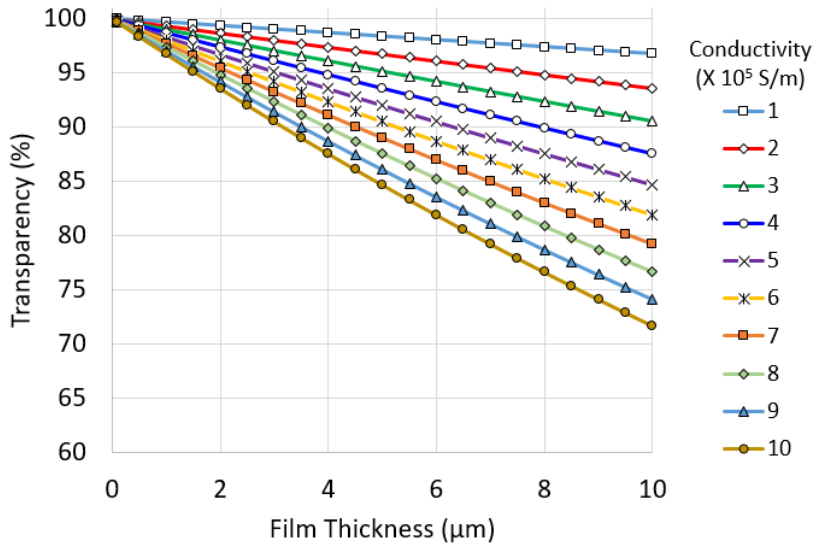

Figure 10 TCO Transparency versus film thickness for various conductivities ranging from 1×10^5 S/m to 1×10^6 S/m.

$$\delta = \sqrt{\frac{2}{\omega\mu_0\sigma}} \quad \text{for } \omega < \omega_p \,, \tag{2.7}$$

where μ_0 is the free space permeability, and σ is the conductivity of the material. The skin depth decreases with increasing material conductivity, and highly conductive TCOs are preferable for antennas.

Below, the antenna efficiency is assessed as a function of film thickness for different designs of rectangular patch topology. The sheet resistance R_S [85] is the major factor, because the sheet resistance is a function of conductivity σ and thickness t of the film:

$$R_S = \frac{1}{\sigma\delta\left(1-e^{\frac{-t}{2\delta}}\right)} \tag{2.8}$$

This sheet resistance calculation is utilized due to the film thickness being thinner than the skin depth of the conducting material for RF frequencies. The resistance of a radiating shape is given as

$$R = R_S \int_0^L \frac{dl}{W(l)} . \tag{2.9}$$

In the case where the shape is rectangular (width W is a constant), the equation simplifies to $R = R_s(L/W)$, where L is the length of the rectangular shape. The efficiency of an antenna is $\varepsilon_{eff} = R_a/(R_a+R)$ where R_a is the antenna resistance (R_a = 50 Ω).

Figure 11 shows the efficiency versus thickness plots calculated under the assumption that the film has a conductivity of 3×10^5 S/m [75] and the antenna operating frequency is 2.4 GHz. One can see that the efficiency increases as the thickness of the film increases. Also seen from Figure 11 is that the antenna efficiency decreases with increasing length to width ratio.

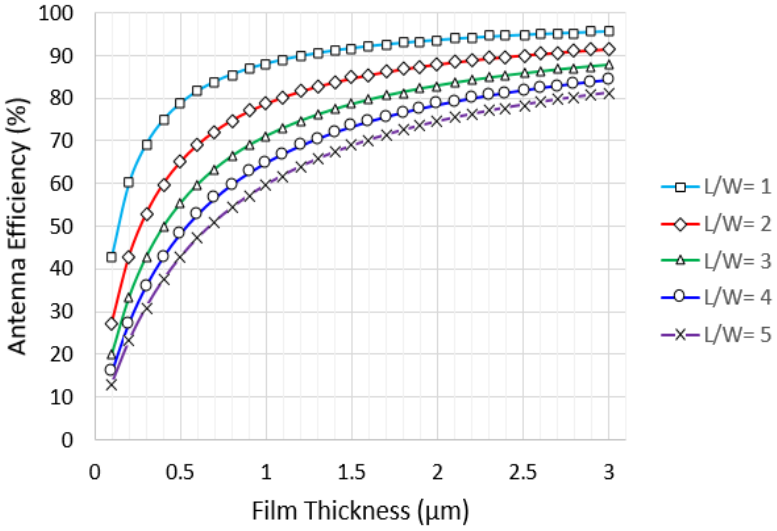

Figure 11 Antenna efficiency versus film thickness calculated for film conductivity of 3×10^5 S/m and antenna resonant frequency of 2.4 GHz.

One more parameter determining the thin film antenna efficiency is the resonant frequency. For a given material conductivity, lower skin depths can be achieved by increasing the frequency of operation. Figure 12 shows plots of antenna efficiency v44ersus microwave frequency for the range between 1 GHz and 50 GHz for different *L*/*W* ratios. As the resonant frequency increases, the antenna efficiency also increases, however, at a decreasing rate. As before, when the length of the antenna increases with respect to the width, the antenna efficiency decreases drastically.

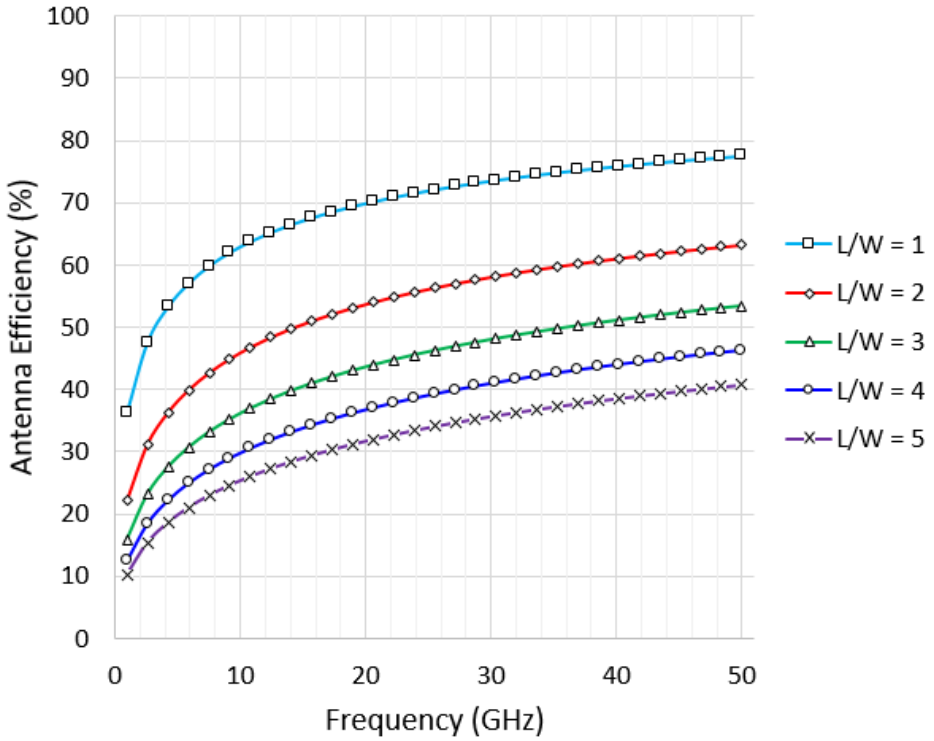

Figure 12 Antenna efficiency versus resonant frequency calculated for film conductivity of 3×10^5 S/m and film thickness of 1.5 µm.

2.4. Transparent Antenna and FSS Figure of Merit

Because transparency decreases while antenna efficiency increases with increase of film thickness, a judgement has to be made as to what film thickness is necessary. A figure of merit

(FOM) for transparent films is proposed in Li *et. al.* [86] that seeks to minimize the conductivity at optical wavelengths while maximizing the conductivity for the film at DC. This FOM, σ_{DC}/σ_{opt}, was developed to determine film transparency and film conductivity relations for the purpose of low frequency or DC electronics. However, because this FOM was not developed with antennas and electromagnetic devices in mind, it does not account for film thickness which greatly affects efficiency. A new FOM, accounting for transparency (equation (2.5)) and antenna efficiency (ε_{eff}), is necessary. Because antenna efficiency and transparency can be considered on equal grounds of importance for and optically transparent antenna, the product of these two terms can be used as the FOM. This product is shown below in equation (2.10),

$$FOM_{ant} = T(\omega_{opt}, t) * \varepsilon_{eff} \, . \tag{2.10}$$

The radiated efficiency is dependent on the antenna topology, film thickness, and film conductivity, making the FOM different for each design. However, for this study, if the antenna topology is assumed to be a rectangular shape with L and W as the length and width respectively, the FOM reduces to equation (2.11) below. In this formula, R_a is the antenna resistance (usually set to 50 ohms), σ is the DC conductivity of the film, δ is the skin depth at the operational frequency of the antenna determined by equation (2.7) above, t is the thickness of the film, q_e is the charge of an electron, N_e is the carrier concentration, m^* is the effective mass of an electron within the film, ε_∞ is the permittivity of the film at high frequencies, ω_{opt} is the optical frequency ($\omega = 2\pi f$), and τ_e is the electron relaxation time. The plot of FOM over various length to width ratios and film thicknesses are shown below in Figure 13,

$$FOM = \frac{R_a \sigma \delta (1 - e^{-t/2\delta})}{R_a \sigma \delta (1 - e^{-t/2\delta}) + L/W} e^{\frac{-377 q_e^2 N_e}{2m^* \sqrt{\varepsilon_\infty} \omega_{opt}^2 \tau_e} t} . \quad (2.11)$$

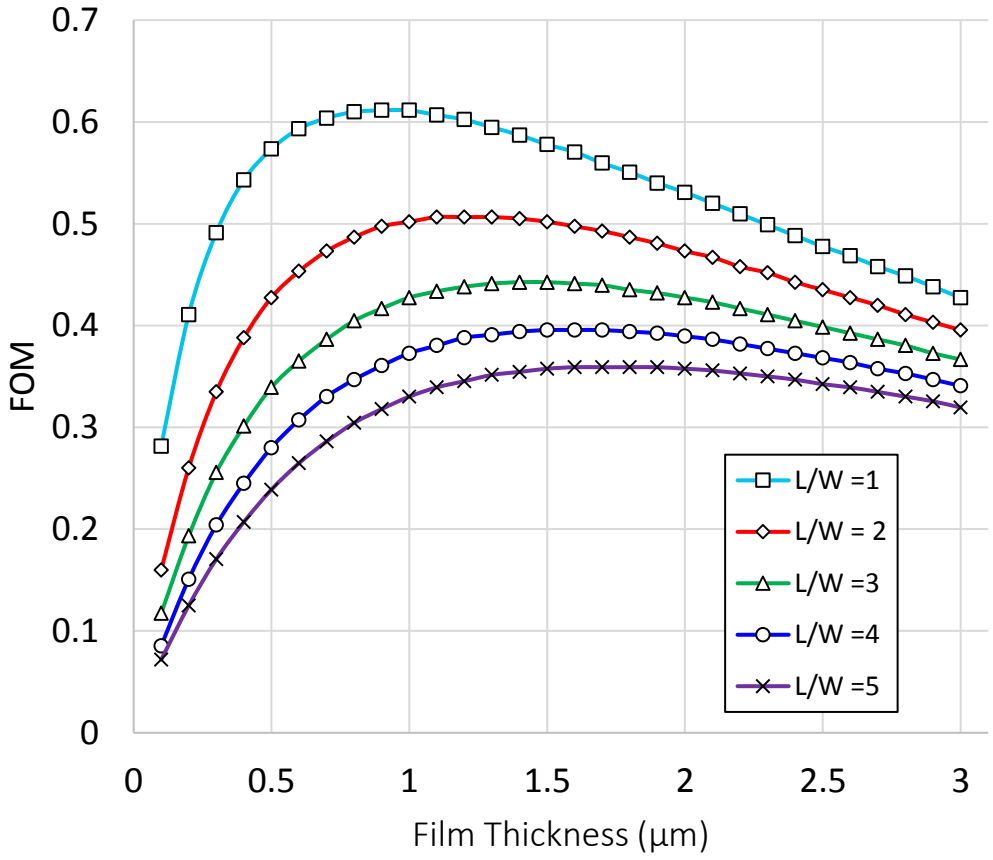

Figure 13 Figure of merit (FOM) for transparent antennas for film thickness over various length to width ratios.

The FOM shows that there is an optimum film thickness where the optical transparency is minimized and antenna efficiency is maximized. Additionally, the antenna shape affects the FOM as shown above in Figure 13. As the length to width ratio increases, the optimum film thickness gets thicker while the effectiveness reduces. One conclusion drawn from this is that the smaller the antenna (in comparison to the operation wavelength) the smaller the optimum film thickness. Extending from this conclusion, this means that different antenna topologies will possess different figures of merit. Furthermore, the antenna efficiency and transparency are affected by carrier concentration. How the figure of merit changes in relation to the thin film material properties needs

to be studied in more detail. In Chapter three, three different antenna topologies will be discussed and how the film properties effect this FOM for each antenna topology.

The figure of merit for frequency selective surfaces (FSSs) is different from the figure of merit for antennas. The common methodology for developing FSSs is to have a solid conductive layer with a pattern etched from the layer to either block or pass certain frequencies through the surface. As a result, the transmission of electromagnetic waves at an operational frequency needs to be minimized and the transmission of optical wavelengths needs to be minimized. This relationship, or figure of merit, is best seen in equation (2.12). In this equation, T is the transparency at an optical frequency (ω_{opt}) and τ is the transmission coefficient at an operational frequency (ω_{opp}),

$$FOM_{FSS} = \frac{T(\omega_{opt},t)}{\tau(\omega_{opp},t)}. \tag{2.12}$$

The transparency is determined using equation (2.5) above. The transmission coefficient is determined through the application of the Maxwell's equations at the boundaries of the transparent film with the surrounding medium (see Figure 14).

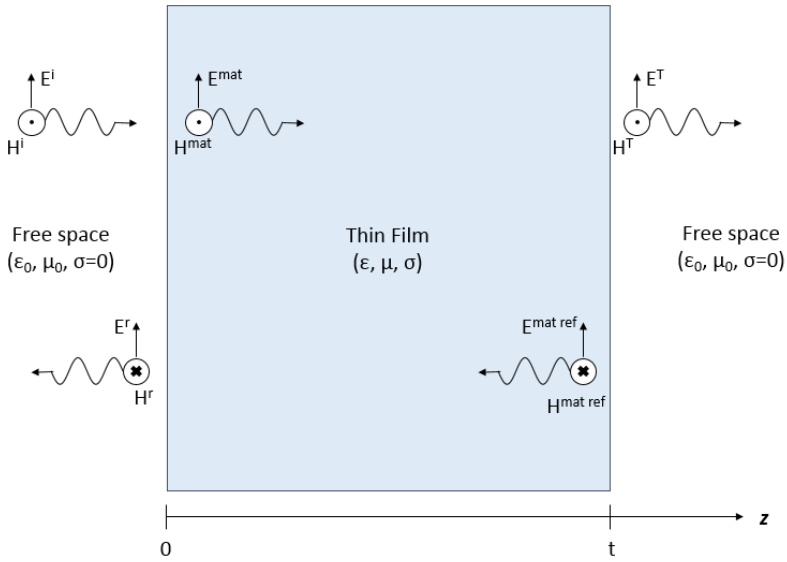

Figure 14 Boundary conditions of electromagnetic field propagating sandwiched between two infinite layers of free space.

In Figure 14, E_i and H_i are the incident electric field and magnetic field intensities, respectively, E_r and H_r are the reflected electric field and the magnetic field intensities, respectively, E_{mat} and H_{mat} are the transmitted field intensities in the film, $E_{mat\ ref}$ and $H_{mat\ ref}$ are the field intensities reflected at the boundary between the film and free space, and E_T and H_T are the transmitted field intensities through the film into free space. The relationship between the electric field intensity incident on the film and that transmits into the film at $z = 0$, is given in equation (2.13) where τ_1 is the transmission coefficient on the free space, film boundary.

$$E_m(z = 0) = \tau_1 E_i(z = 0) \tag{2.13}$$

As the electromagnetic wave propagates through the medium and undergoes an attenuation and a phase shift. The electric field intensity within the material of the $+z$ direction propagating wave is shown below in equation (2.14). In this equation, γ is the complex propagation constant, given in equation (2.15) [87] [88] and t is the thickness of the film. The equations for the propagation constant, the attenuation constant (α)[88], and the phase constant (β)[88] are given below. In these formulas, ω is the angular frequency of operation, μ is the permeability of the material, ε is the permittivity of the material, and σ is the conductivity of the material,

$$E_m(z = t) = E_m(z = 0)e^{-\gamma t} = \tau_1 E_i(z = 0)e^{-\gamma t}, \tag{2.14}$$

$$\gamma = \sqrt{j\omega\mu(\sigma + j\omega\varepsilon)} = \alpha + j\beta,$$

$$\alpha = \omega\sqrt{\frac{\mu\varepsilon}{2}\left[\sqrt{1 + \left(\frac{\sigma}{\omega\varepsilon}\right)^2} - 1\right]},$$

$$\beta = \omega\sqrt{\frac{\mu\varepsilon}{2}\left[\sqrt{1 + \left(\frac{\sigma}{\omega\varepsilon}\right)^2} + 1\right]}. \tag{2.15}$$

The relationship between the electric field intensity transmitted through the film to the field intensity in the material at $z = t$ is that of a second transmission coefficient τ_2. The relationship is shown below in equation (2.16) when equation (2.14) is plugged in

$$E_T(z = t) = \tau_2 E_m(z = t) = \tau_1 \tau_2 E_i(z = 0) e^{-\gamma t}. \quad (2.16)$$

The ratio of the electric field intensity at $z = t$ to $z = 0$ is shown below in equation (2.17). When the transmission coefficient is calculated, the relationship reduce to equation (2.18) where η is the characteristic impedance of the film and η_0 is the characteristic impedance of free space.

$$\frac{E_T(z=t)}{E_i(z=0)} = \tau_1 \tau_2 e^{-\gamma t} = \frac{2\eta_0}{\eta_0+\eta} \frac{2\eta}{\eta_0+\eta} e^{-\gamma t} \quad (2.17)$$

$$\frac{E_T(z=t)}{E_i(z=0)} = \frac{4\eta_0 \eta}{(\eta_0+\eta)^2} e^{-\gamma t} \quad (2.18)$$

Because the characteristic impedance and the propagation constant of the film are complex, the magnitude of the ratio is shows the total attenuation due to reflection and losses within the film. This total attenuation is the transmission coefficient shown above in equation (2.12). This formula is shown below in equation (2.19),

$$\tau(\omega_{opp}, t) = \left|\frac{E_T(z=t)}{E_i(z=0)}\right| = \left|\frac{4\eta_0 \eta}{(\eta_0+\eta)^2}\right| e^{-\alpha t}. \quad (2.19)$$

Where [88],

$$\eta = \sqrt{\frac{j\omega\mu}{\sigma+j\omega\varepsilon}} \quad , \qquad \eta_0 = 120\pi\ \Omega\ .$$

The plot of FOM over various carrier concentrations (N_e) and film thicknesses are shown in Figure 15. The frequency of operation used in the graph was 2.4 GHz. One thing to note, is that the transmission coefficient is so low (on the order of 10^{-3}) at 30 GHz for all thicknesses, that the FOM for a transparent FSS is much higher than that of the FOM for a transparent antenna. One conclusion drawn is that TCOs are more efficiently used in FSS and filter applications. This is

evident in the very low transmission coefficient with the same level of transparency for an antenna using similar carrier concentration and film thickness.

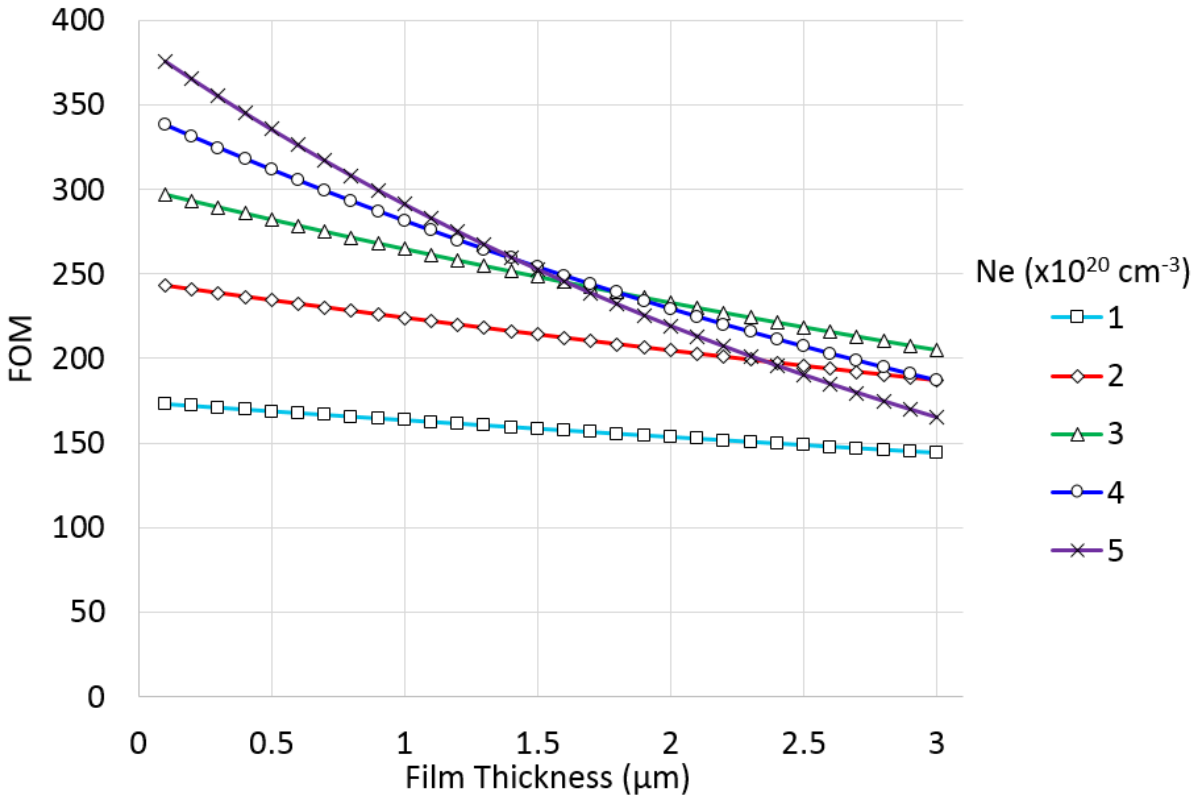

Figure 15 Figure of merit (FOM) for transparent antennas for film thickness over various length to width ratios.

2.5. Transparent Antenna Arrays

Because the efficiency of transparent antennas are significantly low to that of their non-transparent counterparts, one of the main challenges is to counteract this inefficiency while keeping a high transparency. Low efficiencies produce low antenna gains through the relationship below in equation (2.20). In this equation, $G(\theta,\varphi)$ is the gain of the antenna in the (θ,φ) direction, $D(\theta,\varphi)$ is the antenna directivity in the (θ,φ) direction, and ε_{eff} is the antenna efficiency,

$$G(\theta,\varphi) = D(\theta,\varphi) * \varepsilon_{eff} \,. \tag{2.20}$$

One method, as discussed above, to counteract this inefficiency, is to increase the carrier concentration, but this yields lower transparency. Another method to better the antenna performance is to keep antennas operating inefficiently, but to use multiple antennas in an array to increase the gain. The gain of an antenna array compared to the individual antenna (element) gain is shown below in equation (2.21) [89]. In this equation $G_A(\theta,\varphi)$ is the gain of the antenna array, $G_E(\theta,\varphi)$ is the gain of the antenna element, and n is the number of elements in the array,

$$G_A(\theta,\varphi) = n * G_E(\theta,\varphi). \tag{2.21}$$

This method of increasing the effective gain by means of an array has been explored before by Hautcoeur *et. al.* [90] through a meshed Titanium Gold mesh (shown in Figure 16). In this study, the transparent antenna achieved a maximum gain value 9.55 (dBi) at 56.3 GHz. Another thing to note is that the radiating elements are of higher transparency than the corporate feed. This is due to the added inefficiency of transparency, and will be a challenge for the future of transparent antennas, both meshed and thin film.

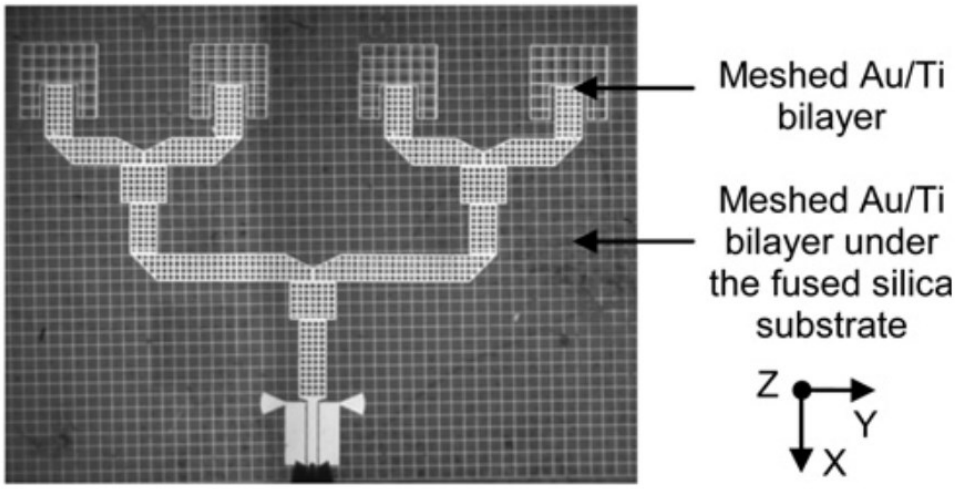

Figure 16 Meshed transparent antenna array explored by Hautcoeur et. al. [90]. Array operates at 60 GHz and has antenna transparency of approximately 75%, feed transparency of approximately 37%, and total transparency of approximately 68%.

2.6. Discussion

While previous studies explores an optically transparent antenna (both meshed and thin films), and antenna arrays via meshed conductors, these studies do not study transparent antenna arrays fabricated using transparent conductive oxides. Moreover, these previous studies do not explore the efficacy of transparent antenna arrays performing beam steering. The rest of this dissertation explores 1) the design, simulation, and fabrication of three antenna topologies using transparent GZO 2) the design, simulation, and fabrication of two frequency selective surfaces and 3) the design, simulation, and fabrication of an optically transparent antenna array for beam forming applications in the upcoming smart city environment.

Chapter 3: Transparent Antennas using Gallium-Doped Zinc Oxide Thin Films

3.1 Introduction

The main objective of this chapter is to study the efficacy of transparent antennas for smart city communication. While the proposed 5G frequencies are between 20 GHz and 300 GHz [1] [2], the limitations of present laboratory equipment limit this study to investigate optically transparent antennas at lower frequencies. While this limitation exists, the smart city will operate with existing communication protocols (Wi-Fi, Bluetooth, LTE) in a mixture or even cognitive environment. As a result, the investigation of antennas operating at current Industrial, Scientific, and Medical (ISM) bands of 2.4 GHz and 5.8 GHz is beneficial to the integration of optically transparent antennas for smart cities. This chapter presents three antenna designs made of GZO thin films. Each antenna topology is studied for variations of material properties and film thicknesses and their effects on the antenna return loss (S_{11}), gain, efficiency, and the figure of merit proposed in Chapter 2. The antennas presented below are a planar dipole antenna, a coplanar hourglass antenna, and a bowtie slot antenna. This chapter also presents an antenna performance overview to give context to the parameters simulated and measured.

3.2 Antenna Performance Overview

The performance of an antenna is measured by various important parameters including radiation pattern, gain, directivity, and impedance. The fields surrounding an antenna can be divided into three distinct areas: 1) Reactive near field, 2) Radiating near field (Fresnel region), and 3) and fair field [91]. The regions are determined by the following equations and shown visually in Figure 17 In these equations, R_1 is the region of the reactive near field, R_2 is the region of the radiating near field, R_3 is the far field region, D is the largest dimension of the radiating antenna, and λ is the wavelength the antenna is broadcasting.

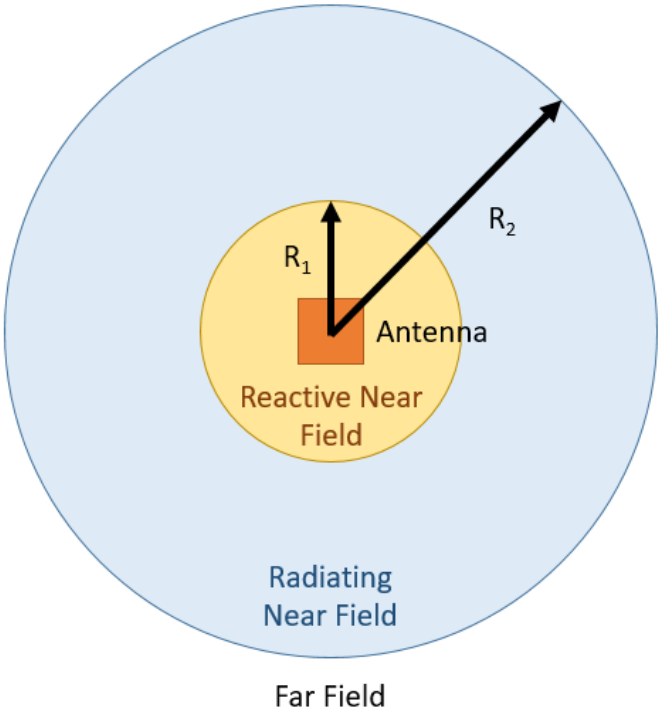

Figure 17 Reactive near fields, radiating near field, and far field of antenna.

$$R_1 < 0.62\sqrt{\frac{D^3}{\lambda}} \tag{3.1}$$

$$0.62\sqrt{\frac{D^3}{\lambda}} < R_2 < 2\frac{D^2}{\lambda} \tag{3.2}$$

$$R_3 > 2\frac{D^2}{\lambda}. \tag{3.3}$$

In the reactive near field region, no energy is dissipated due to the fields being reactive [92]. In the radiating near field region, the radiating fields are dominant compared to the reactive fields and in the fair field region, there are no reactive fields. The electric and magnetic fields attenuate at a $1/R^3$ rate in the reactive near field region, $1/R^2$ rate in the radiating near field region, and $1/R$ rate in the far field region.

The reflection coefficient is another important parameter for the determining antenna performance. In the context of a transmission line (e.g. coaxial cable), the reflection coefficient shows how much voltage, current, and power is being reflected due to load mismatch (See Figure 18). The reflection coefficient is determined by equation (3.4) [88]. In this equation Γ is the reflection coefficient, Z_0 is the characteristic impedance of the transmission line, and Z_L is the impedance of the antenna (or load). The better the load matches the impedance of the transmission line, the closer the reflection coefficient approaches zero. In practice, the reflection coefficient is measured by a network analyzer through the S_{11} scattering parameter. The S_{11} is related to the reflection coefficient through equation (3.5) [94].

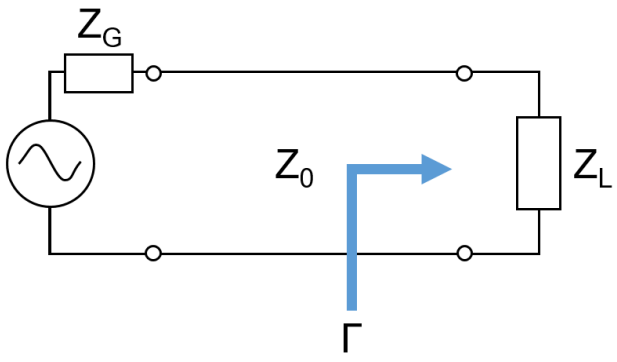

Figure 18 Transmission line diagram showing characteristic impedance of the line (Z_0), and the impedance of the load (Z_L).

$$\Gamma = \frac{Z_L - Z_0}{Z_L + Z_0} \tag{3.4}$$

$$S_{11} = 20 \log_{10} \Gamma. \tag{3.5}$$

Directivity, gain, and efficiency are important parameters to the antenna performance. Furthermore directivity is related to gain and efficiency. Directivity is the ratio between the antenna's radiated power density (at a distant point) to the total antenna radiated power radiated isotropically. For an isotropic radiator, the directivity is the same in every direction. Higher directivity values mean that the antenna intrinsically has higher radiation intensity in particular directions than other, making it more directive. Antenna efficiency is how well the antenna is radiating at the power delivered to the terminals of the antenna. This efficiency can take the form of the product of the conduction efficiency (due to conduction losses) and the dielectric efficiency (due to dielectric losses). These individual losses, however, are difficult to measure or compute, so an antenna measurement often yields the total antenna radiation efficiency. The gain of an antenna is the relationship of the antennas radiated power density to the total antenna input power radiated isotropically. While this definition sounds similar to that of directivity, the major difference is that directivity is the ratio to the radiated power while gain is the ratio to the input power. Looking at this in a transmission line context (Figure 19), it is evident that the radiated power is equal to the input power with the power losses due to inefficiency removed. Therefore $P_{rad} = P_{in} \cdot \varepsilon_{eff}$, where P_{rad} is the radiated power from the antenna, P_{in} is the power supplied to the terminals, and ε_{eff} is the total antenna efficiency.

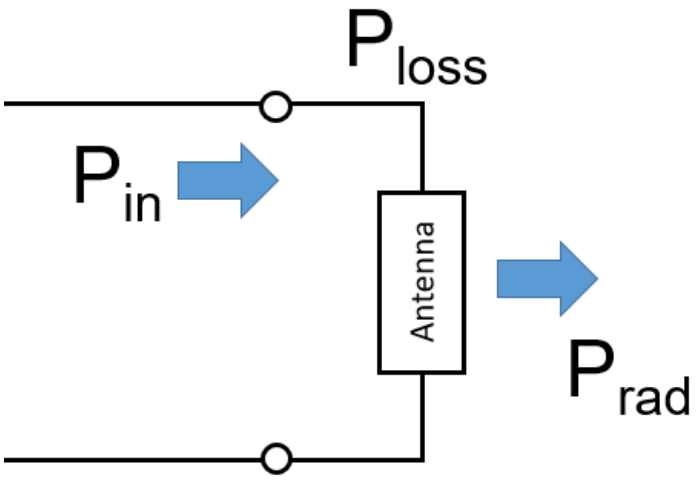

Figure 19 The radiated power from an antenna is less than the power input to the antenna due to losses due to inefficiency.

The equations for directivity and gain are shown in equations 3.6 and 3.7 respectively [91]. The relationship between the two can be also be expressed with the relationship between the radiated power to the input power above, yielding the relationship shown in equation 3.8 [91]. In these equations, P_{rad} is the radiated power from the antenna, P_{in} is the power supplied to the terminals, and ε_{eff} is the total antenna efficiency, $U(\theta,\varphi)$ is the radiation intensity in a particular direction, $D(\theta,\varphi)$ is the directivity in a particular direction, and $G(\theta,\varphi)$ is the gain in a particular direction.

$$D(\theta,\varphi) = 4\pi \frac{U(\theta,\varphi)}{P_{rad}} \tag{3.6}$$

$$G(\theta,\varphi) = 4\pi \frac{U(\theta,\varphi)}{P_{in}} \tag{3.7}$$

$$G(\theta,\varphi) = D(\theta,\varphi) * \varepsilon_{eff} \tag{3.8}$$

This relationship between gain and efficiency will be explored below with three antenna topologies over various carrier concentrations and film thicknesses via ANSYS HFSS, an electromagnetic simulation software. As shown in Chapter 2, the material properties (e.g. doping

concentration, electron mobility, etc.) and the thickness of the film effect the conductivity and added sheet resistance of the GZO film, adding conduction losses into antenna.

3.3 Antenna Designs

The rest of the chapter is organized to study the effects of carrier concentration and film thickness have on the antenna performance parameters of S_{11} (both frequency resonance and magnitude), gain, and efficiency. The figure of merit (discussed in Chapter 2) is studied for each film thickness and carrier concentration. Each of these performance parameters are explored for three antenna topologies: 1) Planar Dipole, 2) Coplanar Hourglass Antenna, and 3) Bowtie Slot Antenna. The fabrication and testing of each antenna is also presented in this chapter.

3.3.1 Planar Dipole Antenna

The first antenna topology studied in this dissertation is the planar dipole. A dipole antenna can be formed by making the conductors of a two-wire transmission at a 180 degree angle, such that the two bent conductors align. For a half wave dipole, the length of these two bent conductors is equal to that of half of the operational wavelength of the antenna. Because GZO needs a substrate to adhere to, a variation of the dipole antenna is looked at: a planar dipole. Unlike a wire dipole, which uses a thicker conductor without the presence of a dielectric substrate, a planar dipole consists of a conductor adhered to a dielectric substrate. The design of this planar antenna is shown below in Figure 20 with the design attributes below in Table 2. This antenna was designed to operate on a 2 inch wide sapphire substrate (relative permittivity $\varepsilon_r = 10$).

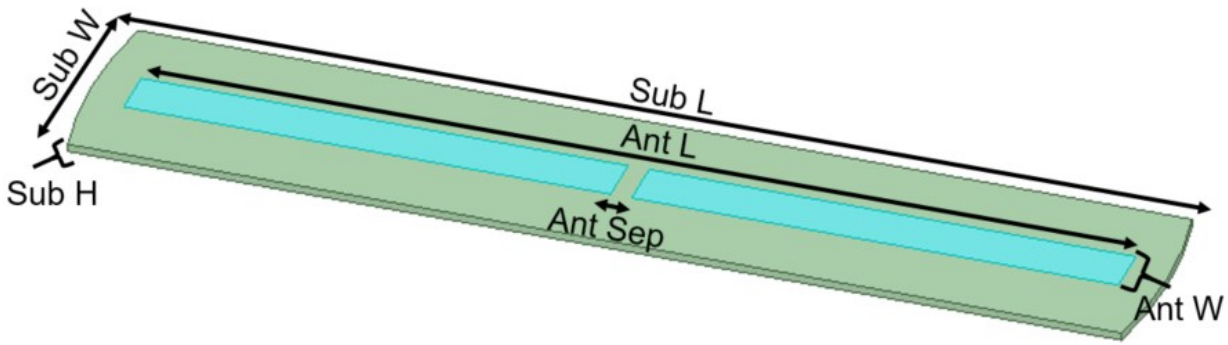

Figure 20 Planar dipole design template.

Table 2 Planar dipole antenna design attributes

Design Attribute	Value (mm)
Ant L	47
Ant W	2.5
Ant Sep	1
Sub H	0.375
Sub L	50.8
Sub W	10

The initial material properties assumed in the design of this antenna were a carrier concentration of $N_e = 4\text{x}10^{20}$ cm^{-3}, an electron mobility of $\mu_e = 31$ cm^2/V·s, and a film thickness of 1.5 μm. The simulated return loss of this design is shown below in Figure 21. This initial simulation shows a resonance of 2.43 GHz at -14.5 dB, with a -10 dB bandwidth from 2.28 GHz to 2.58 GHz (12.3% bandwidth).

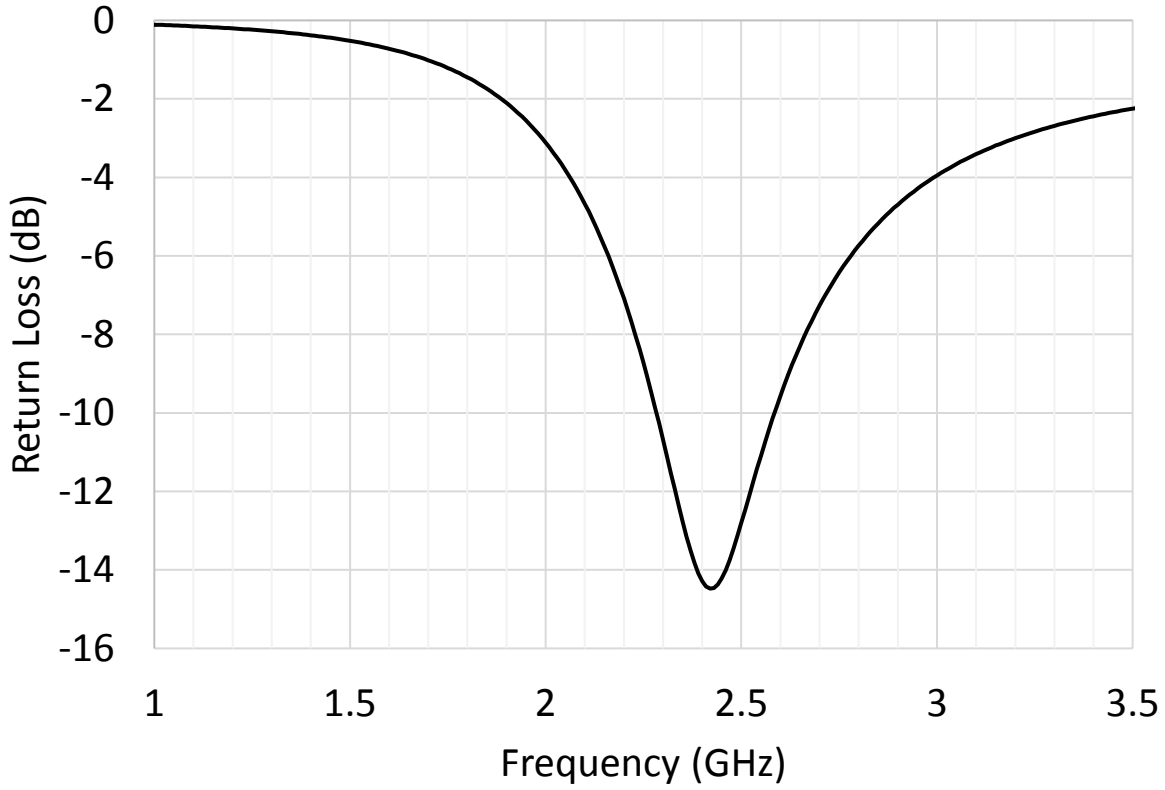

Figure 21 Simulated return loss for planar dipole with $N_e = 4x10^{20}$ cm^{-3}, $\mu_e = 31$ cm2/V·s, and a film thickness of 1.5 µm.

This simulated S_{11}, however, is only one possible return loss possible through the changing of the carrier concentration and film thickness. The antenna was simulated for carrier concentrations ranging from $1x10^{20}$ cm^{-3} to $5x10^{20}$ cm^{-3}, and a film thickness between 0.1 µm and 3.0 µm. The analyzed results of these simulations are shown in Figure 22 and Figure 23. The resonant frequency (the frequency with the minimum return loss) is shown in Figure 22 while the S_{11} value (in dB) for each variation of film thickness and carrier concentration is shown in Figure 23. There are a few conclusions drawn from these simulations. The first conclusion drawn is that low concentrations coupled with thin film thicknesses yield no significant resonance (less than -10 dB) between 1 GHz and 5 GHz. This is seen in Figure 22 where all concentrations have a 5 GHz resonant frequency while having S_{11} value greater than -3dB in Figure 23. Additionally to

this, no carrier concentrations between $1x10^{20}$ cm^{-3} to $5x10^{20}$ cm^{-3} has a resonance below -10 dB while the film thickness is less than that of 1 μm. Another conclusion drawn is that at approximately 0.6 μm of film thickness, all carrier concentrations show a minimum loss at 2.4 GHz, meaning that a minimum conductivity is needed to even possess a resonance at the designed frequency. The simulated S_{11} for all carrier concentrations and film thicknesses are shown in Appendix A.

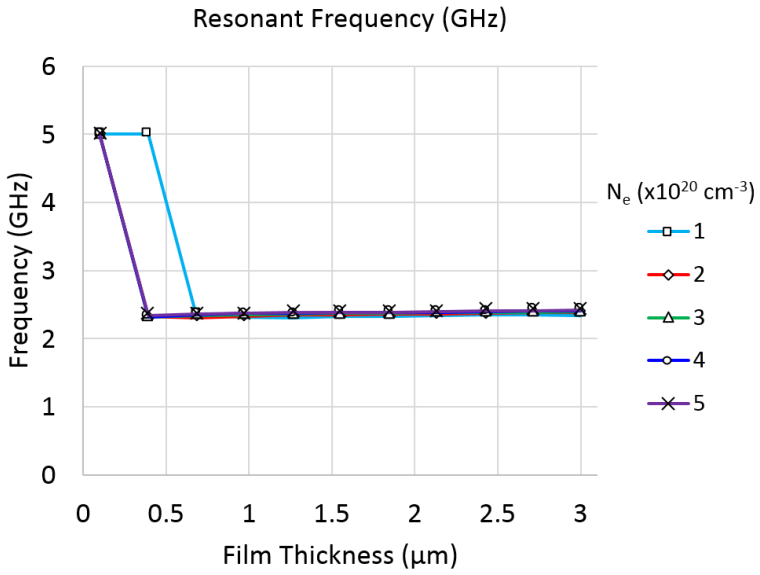

Figure 22 Simulated Resonant Frequency for planar dipole antenna versus carrier concentration, and film thickness.

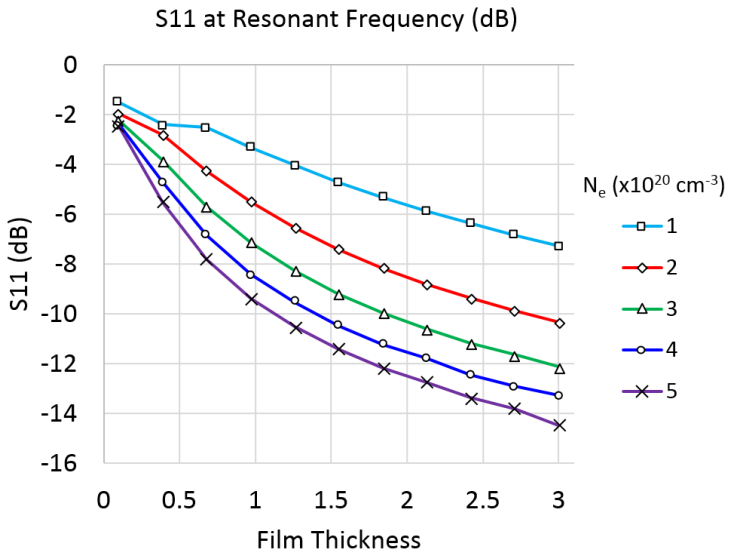

Figure 23 Simulated S_{11} value at resonant frequency (in Figure 22).

In addition to simulating the antennas for the changes in resonant frequency and load match, the antennas were simulated for gain and efficiency differences due to material properties and film thickness. The same simulation variations stated above were used in the study of gain and efficiency differences. The analyzed results of these simulations are shown below in Figure 24 and Figure 25. Figure 24 shows the simulated gain of the planar dipole antenna at 2.4 GHz for various carrier concentrations and film thicknesses. As seen, both gain and efficiency increase with carrier concentration, but increase at decreasing rates. Similarly to the S_{11} results from above, the efficiency and gain values are so low due the lack of resonance at 2.4 GHz, but even as film thicknesses are above 1 μm and concentrations are above 2.0 cm^{-3}, the gains are consistently below that of 1 dBi. The efficiency, correspondingly, are consistently below 70% to 80% (compared to 90%+ of copper radiators).

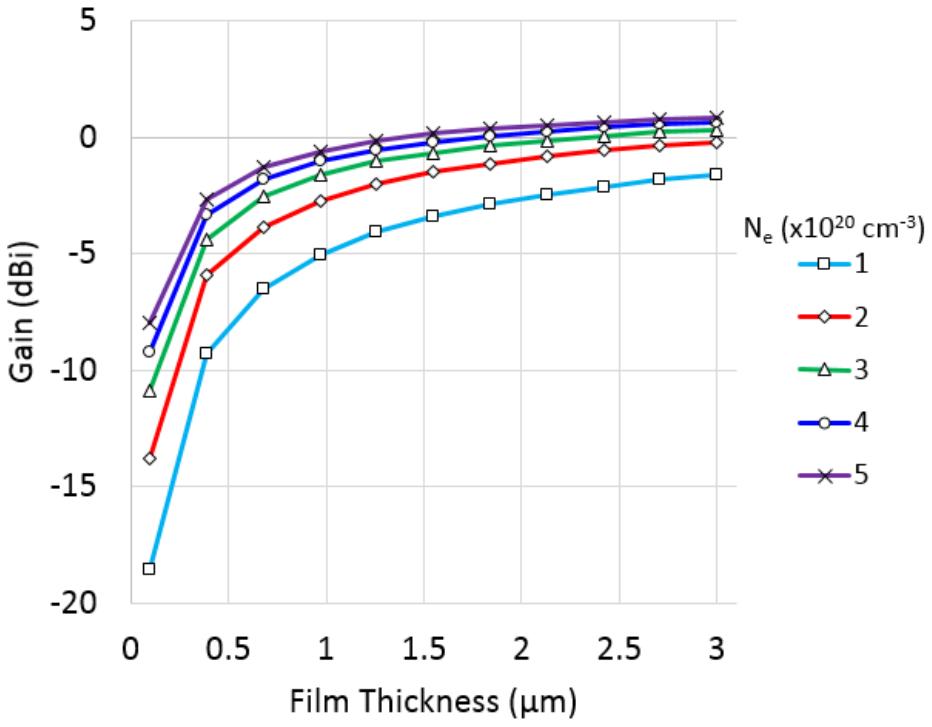

Figure 24 Simulated gain of planar dipole antenna for various carrier concentration and film thickness.

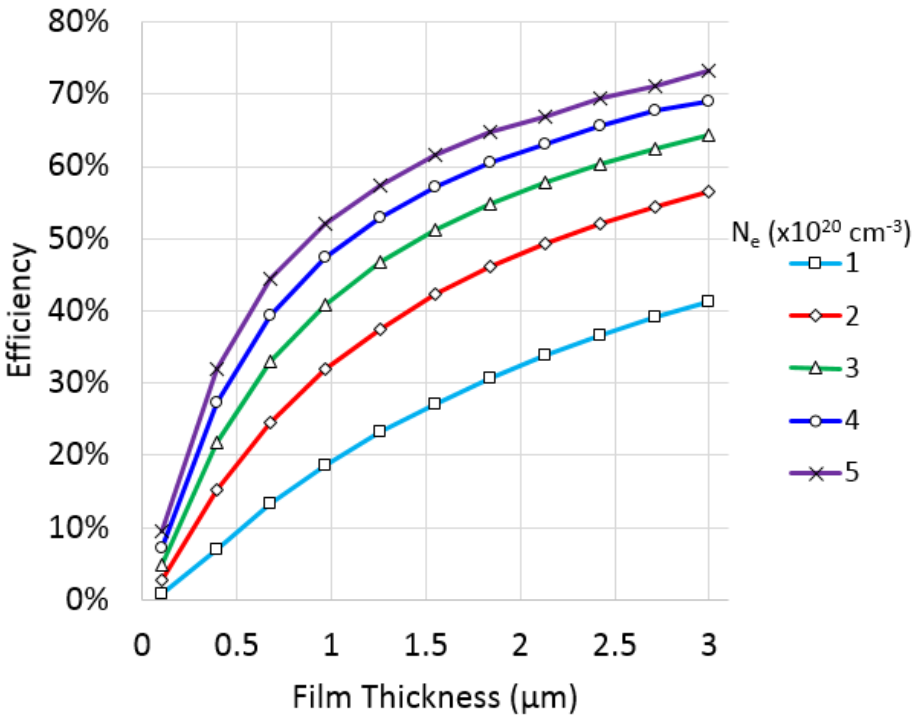

Figure 25 Simulated antenna efficiency of planar dipole antenna for various carrier concentration and film thickness.

From the S_{11}, gain, and efficiency simulation results, a logical conclusion is to increase the film thickness and carrier concentrations as much as possible to counteract the inefficiency and load mismatches present in transparent antennas. However, increasing the carrier concentration can lead to marginal decreases in film transparency and increasing the film thickness can lead to significant decreases in film transparency. Using the FOM equation proposed in chapter 2 (equation (2.10)), the transparency equation in chapter 2 (equation (2.5)), and the efficiencies shown in Figure 25, the figures of merit versus the film thickness shown in Figure 26. The figure shows that as the carrier concentration is increased, the optimum film thickness decreases. This coupled with the conclusions drawn above about the gain and S_{11}, the figures of merit suggest that a carrier concentration between $3x10^{20}$ cm^{-3} and $4x10^{20}$ cm^{-3}.

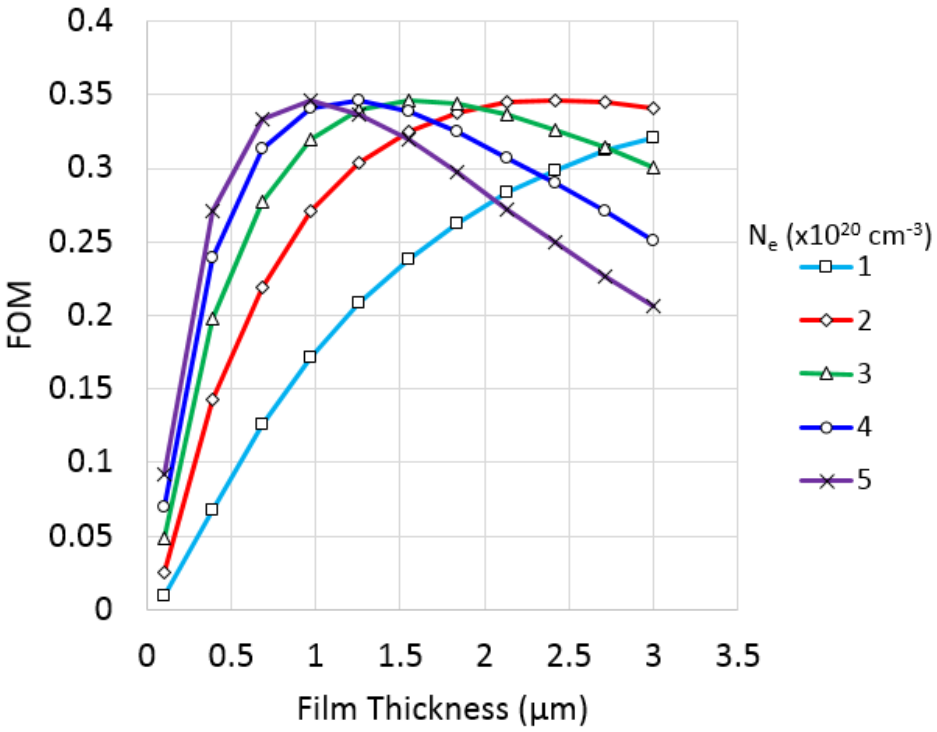

Figure 26 Simulated antenna figure of merit for a planar dipole antenna for various carrier concentration and film thickness.

The next step in the study of the planar dipole antenna is the fabrication and measurement of the topology. GZO thin films were grown on double side polished (0001) sapphire substrates using plasma assisted molecular beam epitaxy (MBE) with an RF plasma oxygen source and the Knudsen cells for Zn and Ga. (REF) Pyrolytic boron nitride (PBN) crucibles were used for both Zn and Ga sources. First, a 2 nm-thick MgO buffer layer was grown at 710 °C to ensure 2D nucleation. To achieve an atomically flat surface, a ~15 nm thick low temperature (LT) ZnO buffer layer was deposited at 300 °C followed by annealing at 730 °C and the growth of ~15 nm high temperature (620°C) ZnO layer serving as a high quality buffer layer for the subsequent growth of GZO films. The GZO films were deposited at ~9 x 10^{-6} Torr oxygen chamber pressure, 400 W RF plasma power, and a substrate temperature of 350 °C, the set of conditions found to be optimal to maximize the film conductivity. The growth rate was ~ 115 nm/hr, and the resulting thickness of GZO film was ~1.4 µm (determined from step profiler measurements). Rapid thermal annealing

at ~600 °C in nitrogen environment for 1 min was employed to improve GZO conductivity. The electrical characteristics of GZO samples were determined by using Hall measurement in the van der Pauw configuration. After annealing, the GZO electron concentration and mobility were found to be ~4 x 10^{20} cm^{-3} and ~40 cm2/V·s, respectively, resulting in a conductivity of $\sigma = 3.0 \times 10^5$ S/m. The antenna was fabricated by using the conventional photolithography process (Figure 27) and the resulting GZO antenna mounted to a SMA connector is pictured in Figure 28.

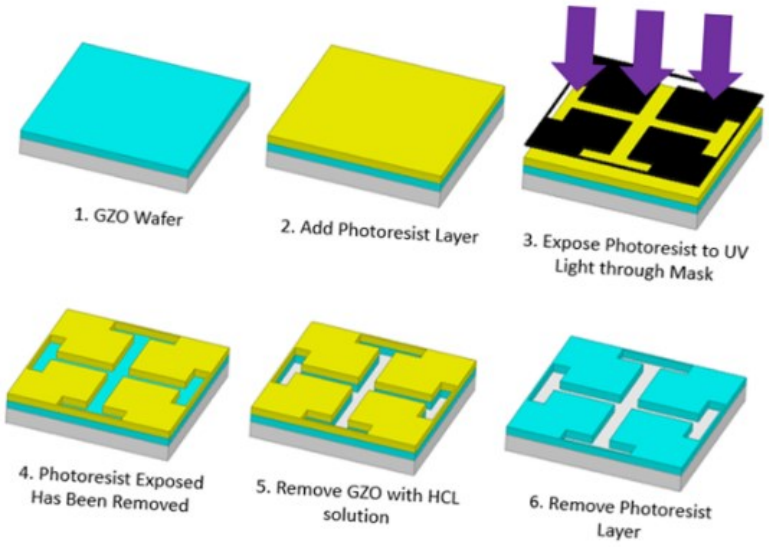

Figure 27 Photolithography process for GZO antennas and filters.

Figure 28 Fabricated 2.4 GHz transparent GZO Dipole Antenna.

The return loss of the fabricated GZO antenna measured with a Keysight PNA 5225A Network Analyzer is also shown in Figure 29. At 2.4 GHz, the return loss of the fabricated antenna is -12.4 dB, and the bandwidth extends from 2.33 GHz to 2.87 GHz (20.8% Bandwidth). The measured results show that there is a frequency shift between the simulated and measured results. This is due to the connection of the coaxial port to the GZO film as well as the absence of a balun (a transformer to convert an unbalanced load to a balanced load). While the frequency does show a shift and while tested without a balun, a strong resonance in the 2.4 GHz ISM band is still present.

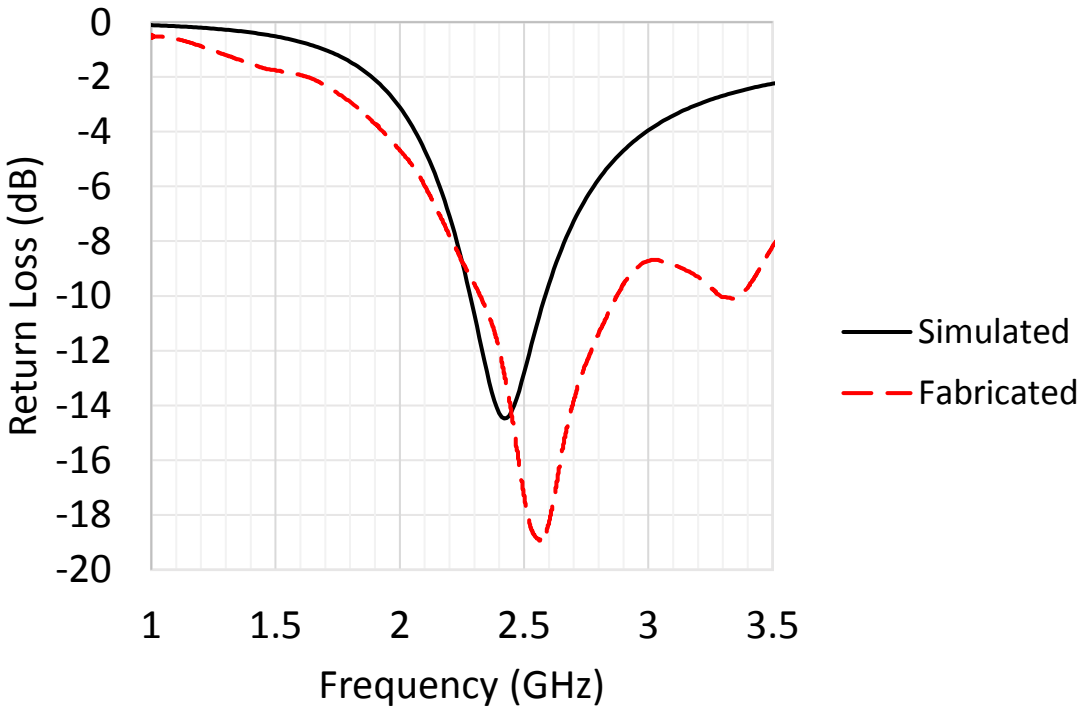

Figure 29 Return loss for the GZO dipole antenna.

3.3.2 Planar Hourglass Monopole Antenna

The second antenna studied in this dissertation is a planar hourglass monopole antenna. The design is based on the antenna developed by Sarkar *et. al.* [95] due to the topology's ultra-

wide band characteristics. Because of the ultra-wide band nature of this topology, resonant frequency shifts (as seen in the planar dipole antenna in the previous section) do not pose as detrimental effect on the radiating efficiency on the antenna. The antenna comprises of 2 semi elliptic conductors placed on a substrate (Figure 30). The top semi elliptic is fed via a coplanar waveguide strip bisecting the lower semi elliptic conductor. The design attributes of the antenna are shown below in Table 3 The antenna was designed to operate on a 2 inch wide sapphire substrate (relative permittivity $\varepsilon_r = 10$).

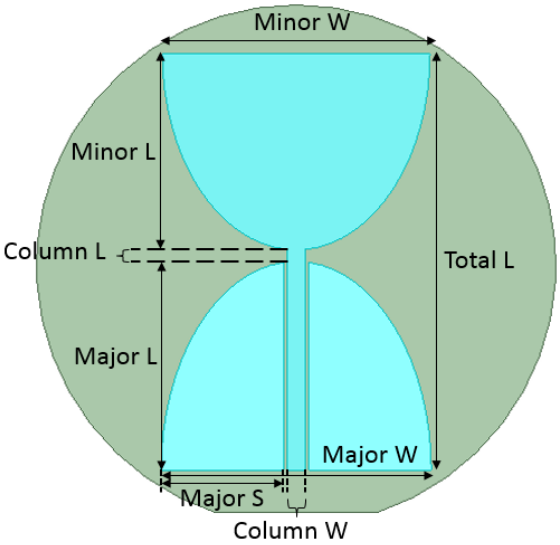

Figure 30 Planar hourglass antenna design template.

Table 3 Planar hourglass antenna design attributes.

Design Attribute	Value (mm)
Column L	1.22
Column W	1.75
Major L	20.34
Major S	12.88
Major W	26.4
Minor L	19.14
Minor W	26.16
Total L	40.7

The initial material properties assumed in the design of this antenna were a carrier concentration of $N_e = 4x10^{20}$ cm^{-3}, an electron mobility of $\mu_e = 31$ cm^2/V·s, and a film thickness of 1.5 μm. The simulated return loss of this design is shown below in Figure 31. This initial simulation shows a resonance at 1.9 GHz at -23 dB, with a S_{11} value at 2.4 GHz of -12.5 dB and an S_{11} value at 2.5 GHz of -12.6 dB.

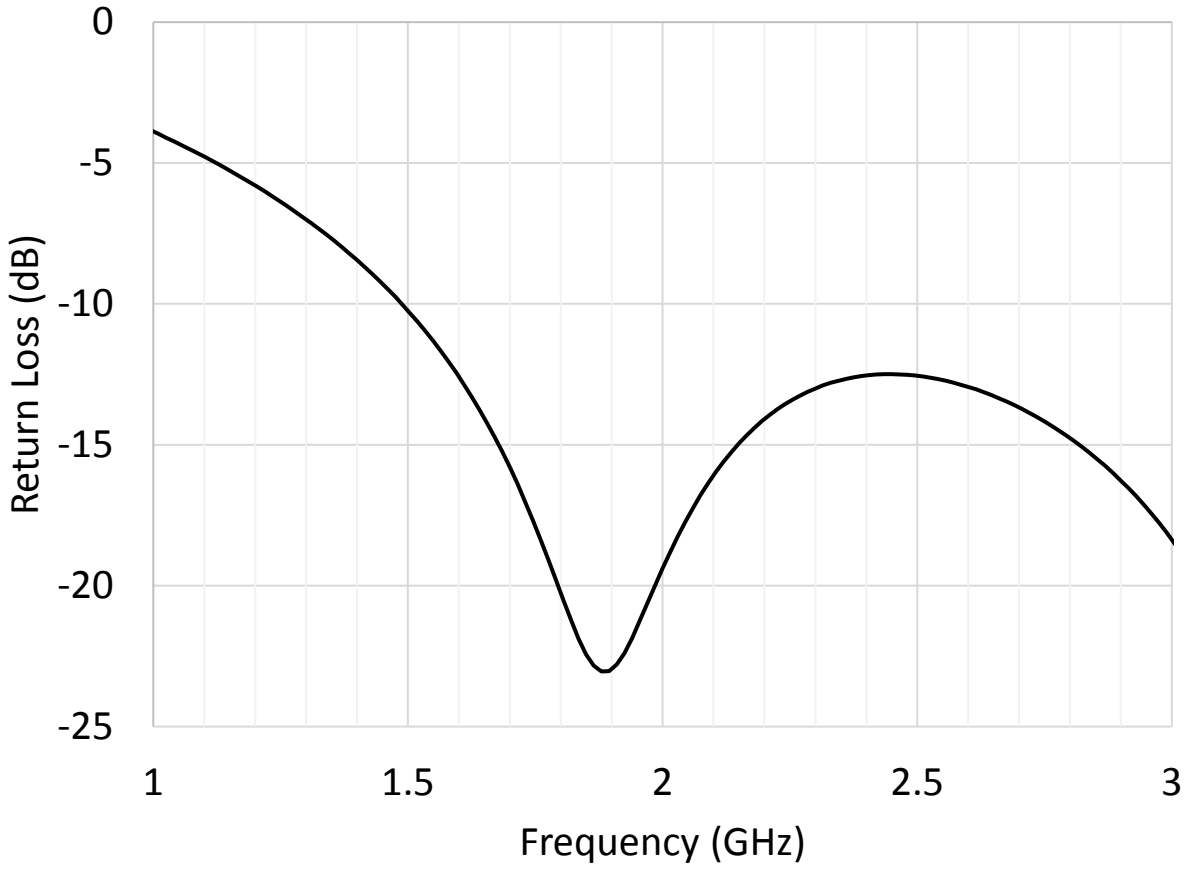

Figure 31 Simulated return loss for planar hourglass antenna with $N_e = 4x10^{20}$ cm^{-3}, $\mu_e = 31$ cm^2/V·s, and a film thickness of 1.5 μm.

Similar to the study done with the dipole antenna in the previous section, the return loss will change as the carrier concentration and film thickness are changed. The same simulation conditions used with dipole ($1x10^{20} \leq N_e \leq 5x10^{20}$ cm^{-3}, $0.1 \leq$ thickness ≤ 3 μm) were used to simulate the planar hourglass shape. The analyzed results of these simulations are shown in Figure

32 and Figure 33. The resonant frequency (the frequency with the minimum S_{11} value) is shown in Figure 32 while the S_{11} value is shown in Figure 33. Similar to the dipole antenna, the higher the carrier concentration, the lower the film thickness needs to be to reach a resonant frequency close to that of the ISM frequency band. Moreover, when the carrier concentration is higher than $2x10^{20}$ cm^{-3}, there exists an optimum film thickness between 0.1 μm and 3 μm for reducing the return loss. This optimum film thickness decreases as the carrier concentration is increased. The simulated S_{11} for all carrier concentrations and film thicknesses are shown in Appendix A.

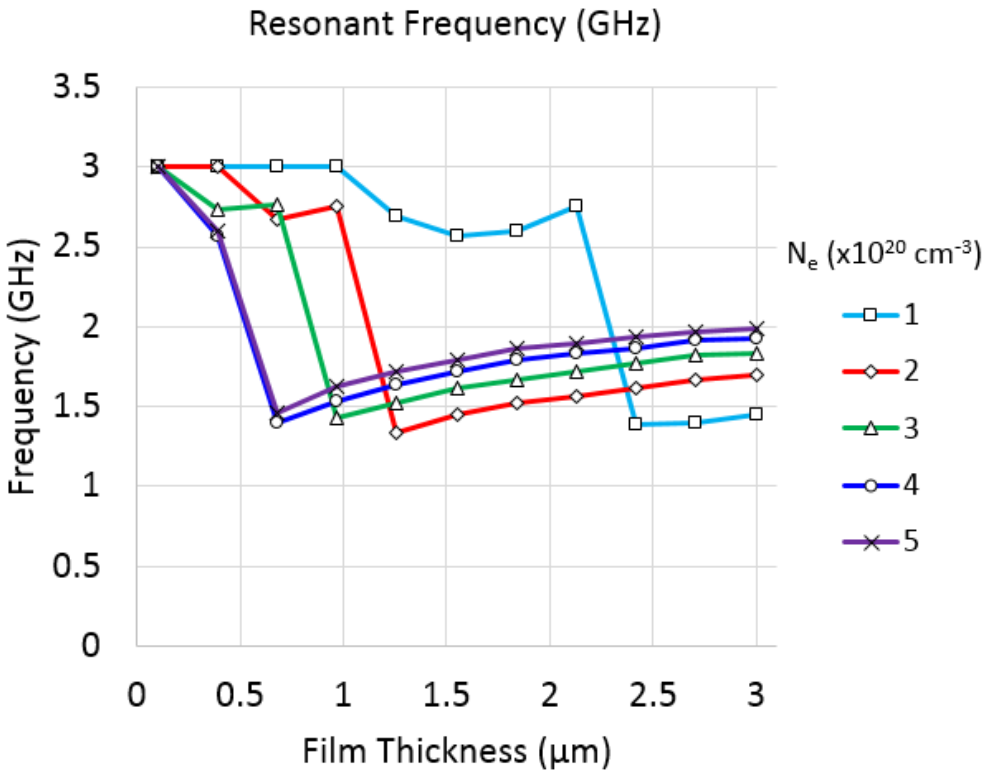

Figure 32 Simulated resonant frequency for planar hourglass antenna versus carrier concentration and film thickness.

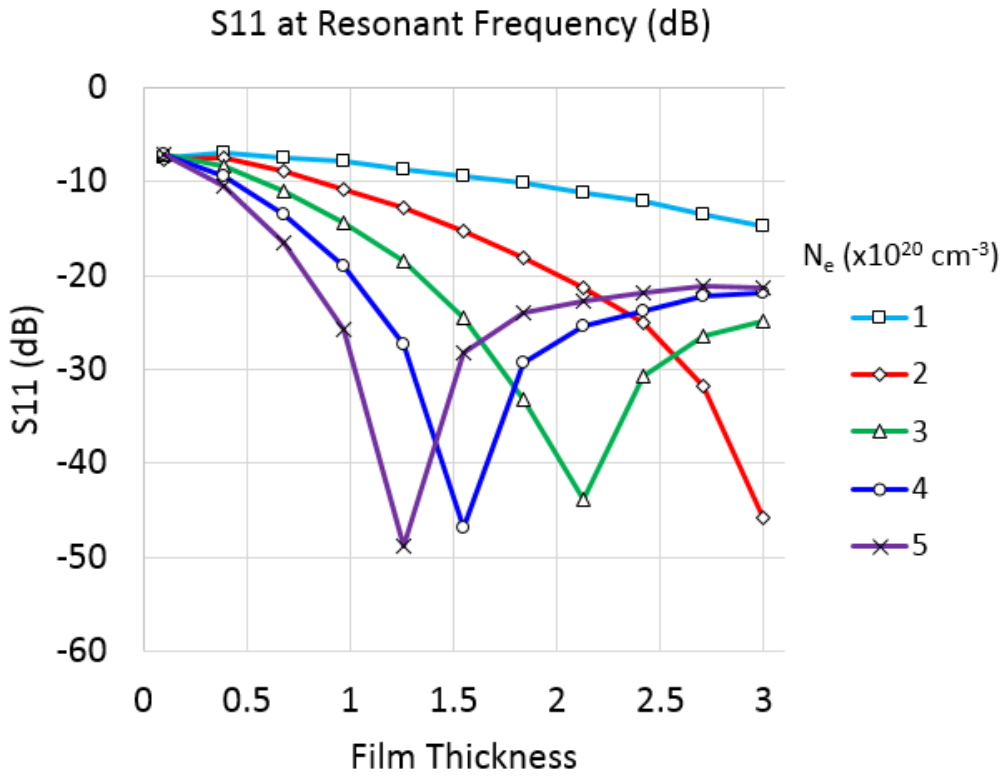

Figure 33. Simulated return loss value at resonant frequency (Figure 32) of planar hourglass antenna.

The gain and efficiency were simulated for the planar hourglass topology were simulated over the same range of carrier concentrations and film thicknesses as stated in the previous section. The results of these simulations are shown below in Figure 34 (Gain versus film thickness), and Figure 35 (Efficiency versus film thickness). Comparable to the results of the dipole antenna, the antenna gain and efficiency increase as the film thickness and the carrier concentration increases. In all circumstances, the gain is consistently below 0 dBi. The efficiency, consequently, is consistently below 60%.

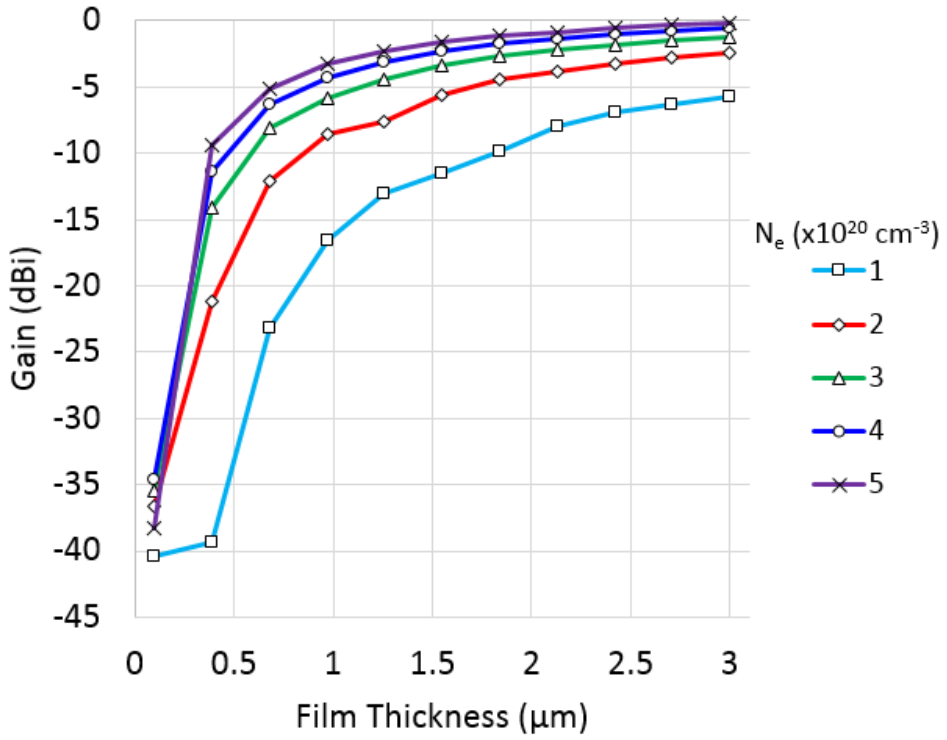

Figure 34 Simulated gain of planar hourglass antenna for various carrier concentrations and film thicknesses.

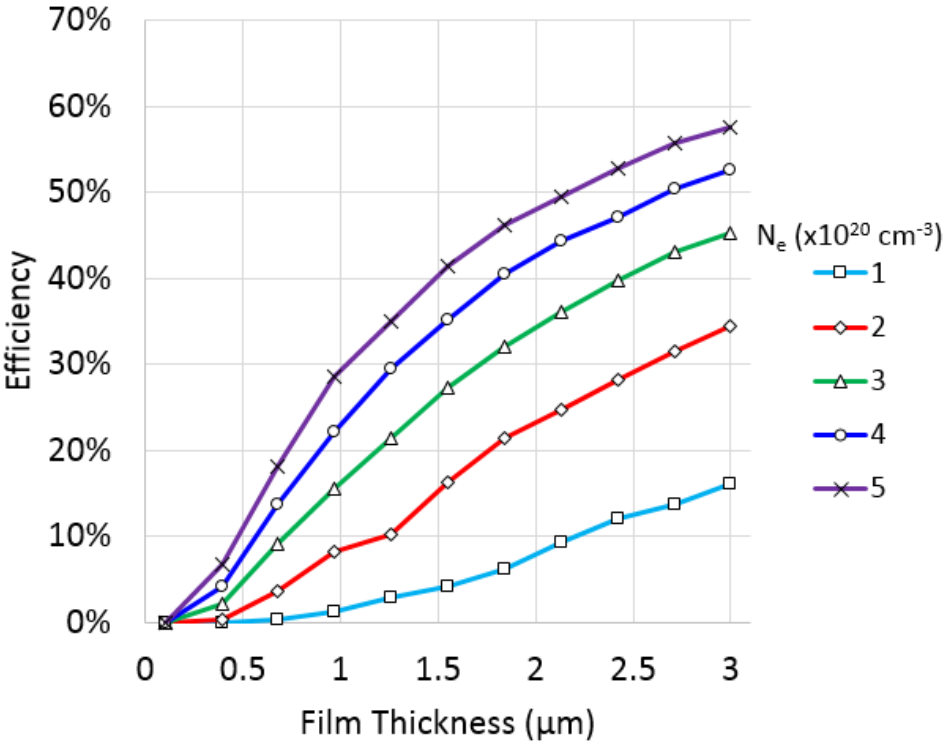

Figure 35 Simulated antenna efficiency of planar hourglass antenna for various carrier concentrations and film thicknesses.

Using the equations for the antenna figure of merit proposed in chapter 2 (equation 2.10), the transparency equation in chapter 2 (equation 2.5), and the efficiencies shown in Figure 35, the FOM for different carrier concentrations and film thicknesses are shown below in Figure 36. In the figure, it is seen that as the carrier concentrations increases above $2x10^{20}$ cm^{-3} there exists an optimum film thickness that maximizes both film transparency and antenna efficiency. The wideband nature of the antenna topology along with the Figure of merit suggests that the optimal carrier concentration of the antenna should be between $3x10^{20}$ cm^{-3} and $4x10^{20}$ cm^{-3}, with a film thickness between 2.0 μm and 2.5 μm.

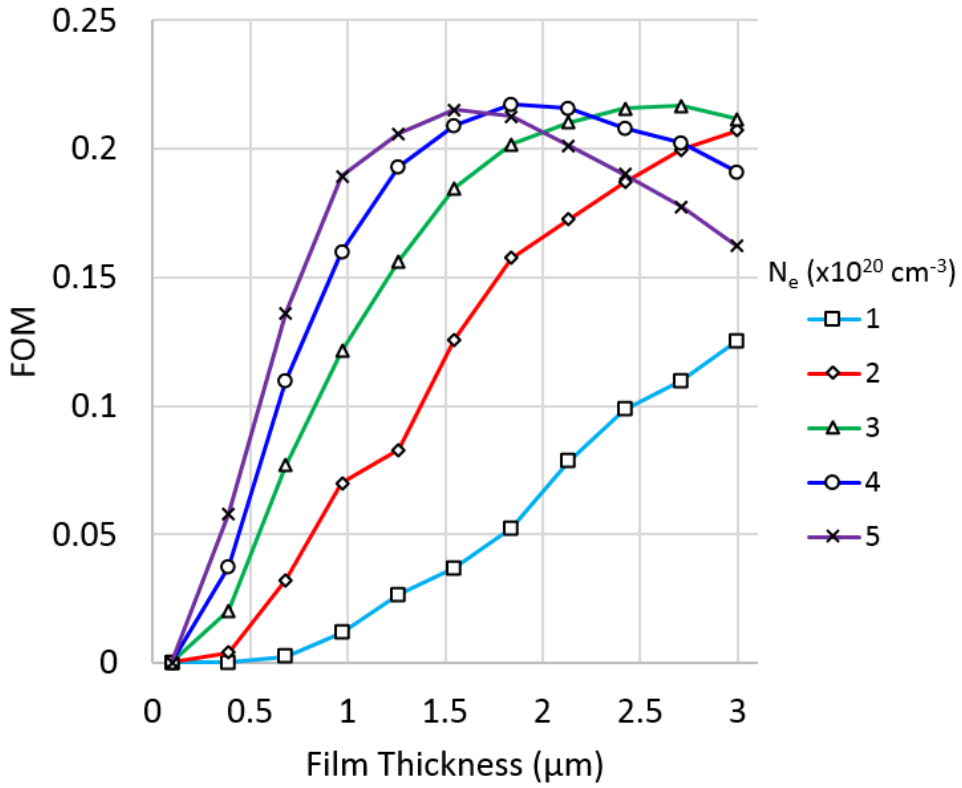

Figure 36 Simulated antenna figure of merit for a planar hourglass antenna for various carrier concentrations.

The next step in the study of the planar hourglass antenna is the fabrication and measurement of the topology. A GZO film was grown by plasma enhanced molecular beam

epitaxy (P-MBE) on a two-inch diameter, 375 μm thick c-sapphire substrate. Prior to loading into the MBE system, the substrate was degreased with acetone and methanol followed by rinsing with deionized water and blowing with nitrogen. After loading to the growth chamber, the sapphire substrate was pre-exposed to oxygen plasma at 750 °C for 30 min at a reactor pressure 1.5×10^{-6} Torr. First, a 2-nm-thick wurtzite MgO layer was grown at 700 °C, followed by a 15-nm-thick low-temperature (LT) ZnO buffer layer grown at 300 °C and a Zn flux of 0.01 nm/s. During both the MgO and the LT ZnO buffer layer growth, the oxygen gas flow was kept at 0.3 sccm, which corresponds to 5.5×10^{-6} Torr reactor pressure. After annealing the LT-ZnO layer at 700 °C for 5 min at 5.5×10^{-6} Torr reactor pressure with closed O-plasma shutter, ZnO growth proceeded at 620 °C with 0.025 nm/s Zn flux and 0.5 sccm oxygen gas flow for 10 min to obtain a high-quality ZnO buffer for subsequent GZO growth. The substrate was then cooled down to 350° C for the growth of GZO layer. The Ga cell temperature was maintained at 535 °C, which corresponds to a doping level of ~ 4×1020 cm^{-3} ($\sigma = 3\times10^{5}$ S/m). The growth of GZO layer was carried out at highly Zn-rich conditions for 12 hours, and total film thickness was ~1 μm, as measured by an alpha-step profilometer. The GZO films were patterned using a photolithography process, as shown schematically in Figure 27. The process includes pattern generation in photoresist, exposure, development, and etching. The antenna was fed with a right angle SMA jack (Cinch Connectivity Solutions Johnson 142-0701-321) with silver conductive epoxy (MG Chemicals 8330S-21G) adhering the jack to the GZO film. The resulting antenna is shown in Figure 37. Note the water-clear transparency of the devices not obscuring visibility of images located behind them. The simulated and measured results of the antenna are shown below in Figure 38. One can see that the simulation predicts a resonant frequency at 1.90 GHz with a return loss value of -23.0 dB. The measured results show a resonant frequency at 1.98 GHz with a return value of -17.1 dB. The

differences between the measured and simulated show a 20 MHz shift with a 6 dB shift upwards. This is most likely due to the imperfections in the feeding of the antenna with the right angle SMA jack. While there is both a frequency shift and added return loss, the return loss shoes appropriate impedances within the 2.4 GHz ISM band (2.4 GHz to 2.5 GHz).

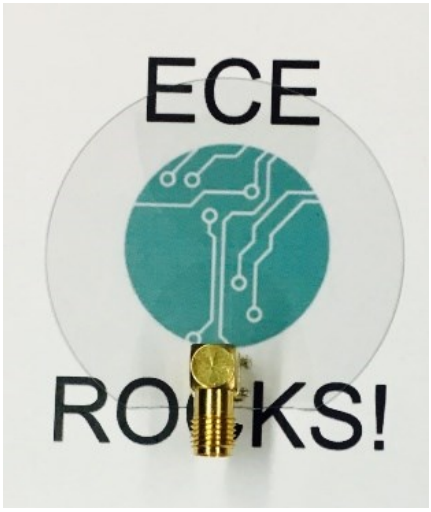

Figure 37 Fabricated 2.4 GHz GZO planar hourglass antenna.

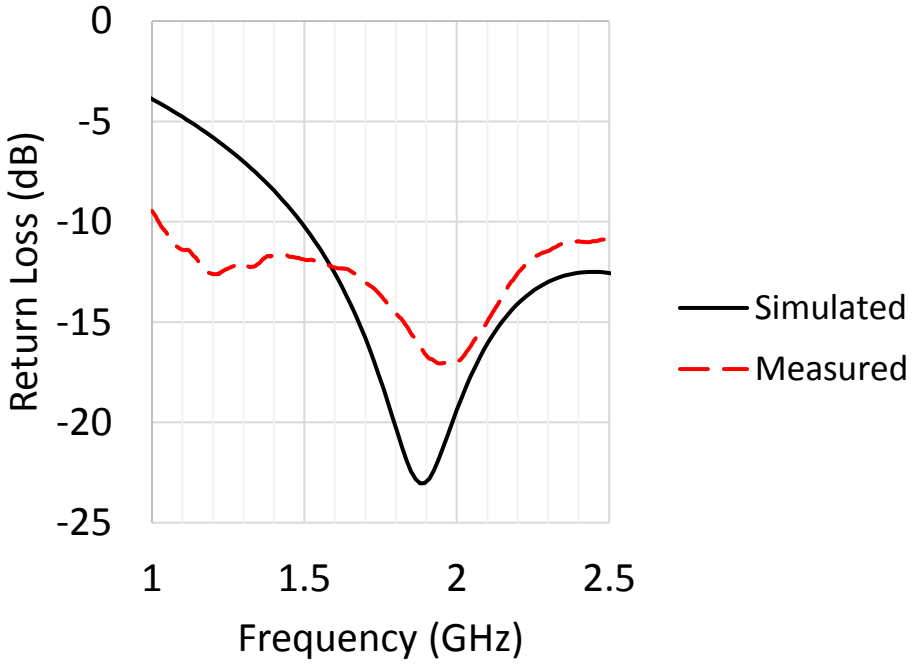

Figure 38 Return loss for the GZO planar hourglass antenna.

3.3.3 Bowtie Slot Antenna

The last antenna topology studied in this dissertation is a bowtie slot antenna. A slot antenna is a complementary version of a wire or planar antenna. Babinet's principle allows for the wire form of the antenna to predict the pattern and impedance of a slot form of that antenna [96] [97]. A slot antenna consists of a conductive surface with a slotted pattern removed from this surface. In this case, the conductive surface used in this design is GZO and a serpentine bowtie dipole antenna is cut out of the design. The resulting design is fed via a center feed line extending from the center of the bowtie pattern to the edge of the substrate. The antenna design template is given in Figure 39 and the design attributes are given in Table 4.

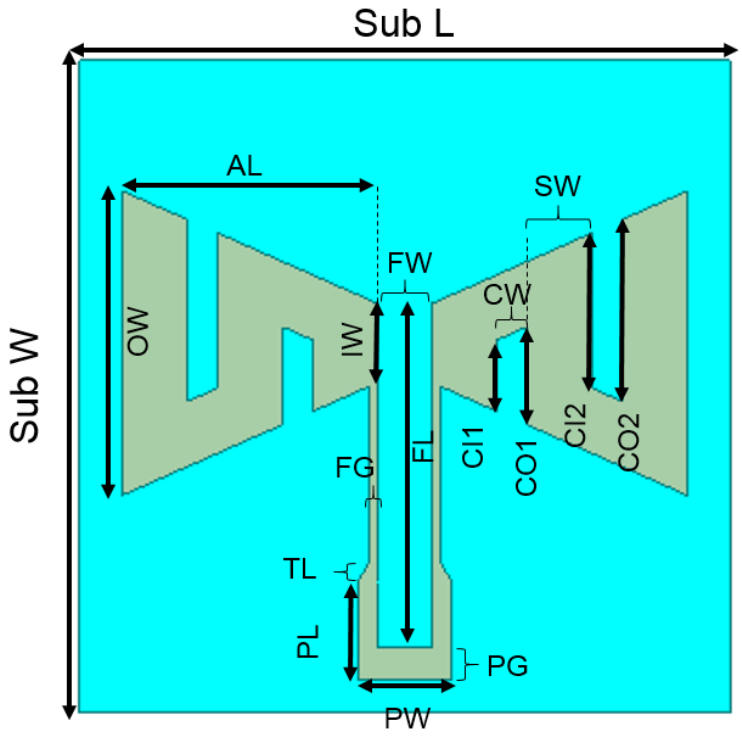

Figure 39 Bowtie slot antenna design template.

Table 4 Bowtie slot antenna design attributes

Design Attribute	Value (mm)	Design Attribute	Value (mm)
AL	5.9	*IW*	1.8
CW	0.7	*OW*	7
CI1	1.622	*PG*	0.75
CO1	2.239	*PL*	2.25
CI2	3.561	*PW*	2.18
CO2	4.178	*SW*	1.5
FG	0.2	*Sub L*	15
FL	7.9	*Sub W*	15
FW	1.28	*TL*	0.5

The initial material properties assumed in the design of this antenna were a carrier concentration of $N_e = 4\text{x}10^{20}$ cm^{-3}, an electron mobility of $\mu_e = 31$ cm^2/V·s, and a film thickness of 1.5 µm. The simulated return loss is shown below in Figure 40. The initial simulation shows a return loss resonance of -25.6 dB at 5.14 dB with a 5.75 GHz S_{11} value of -22.2 dB and a 5.8 GHz S_{11} value of -21.5 dB.

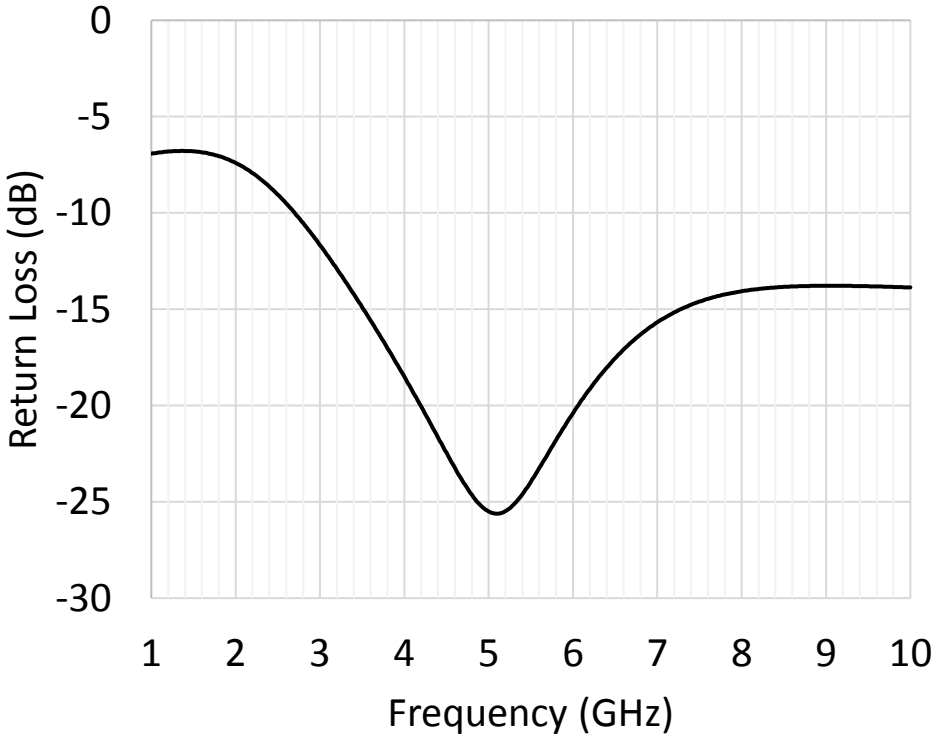

Figure 40 Simulated return loss for a Bowtie Slot antenna with $N_e = 4\text{x}10^{20}$ cm^{-3}, $\mu_e = 31$ cm^2/V·s, and a film thickness of 1.5 µm.

As performed with the planar dipole and the planar hourglass antenna, the antenna is simulated for various carrier concentrations and film thicknesses. The same simulation profile ($1x10^{20} \leq N_e \leq 5x10^{20}$ cm^{-3}, $0.1 \leq$ thickness ≤ 3 μm) was used on the bowtie slot antenna topology. The analyzed results are shown below in Figure 41 (S_{11} resonant frequency) and

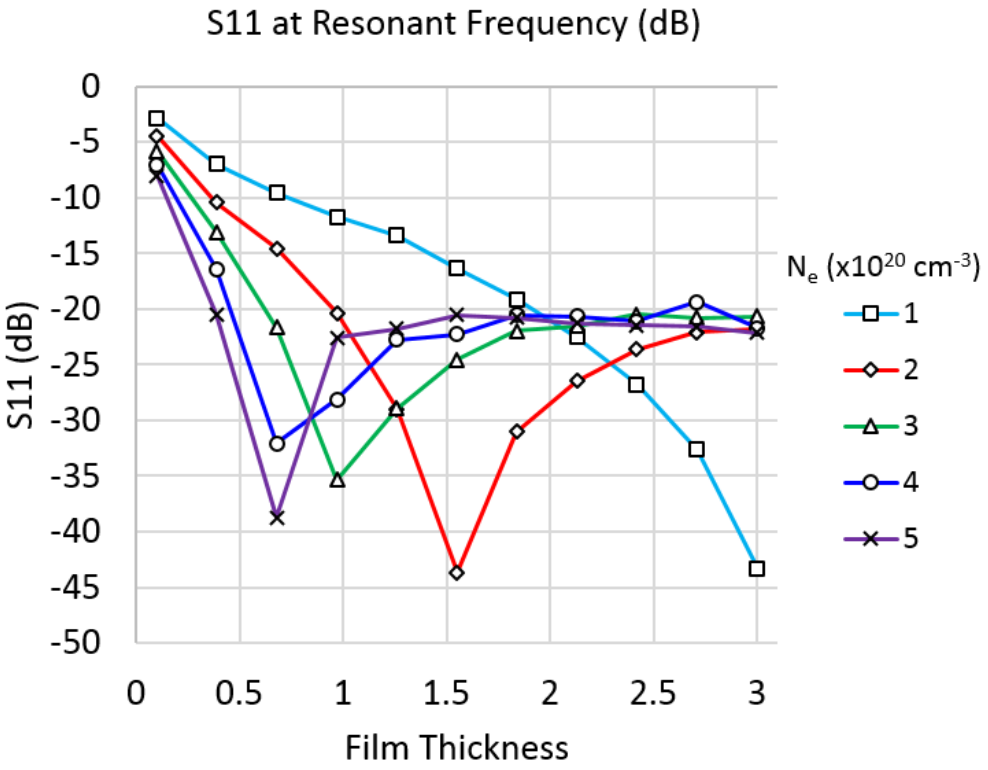

Figure 42 (S_{11} value at resonant frequency). Similar to both the dipole and the hourglass antenna, the antenna shows that as the film thickness is increased, the resonant frequency of the antenna becomes more stable and settles between 5 GHz and 6 GHz. Furthermore, all carrier concentrations show a stable resonant frequency at film thicknesses of 1.25 μm. Additionally, the S_{11} value shows a similar pattern to that of the simulations performed for the planar hourglass antenna. The figure shoes that when the carrier concentration is greater than $2x10^{20}$ cm^{-3}, there exists an optimum film thickness to minimize return loss of the antenna. In all cases though, the

antenna shows at film thicknesses greater than 1.25 μm, the antenna topology shows a strong resonance in the 5 GHz to 6 GHz range. The simulated S_{11} for all carrier concentrations and film thicknesses are shown in Appendix A.

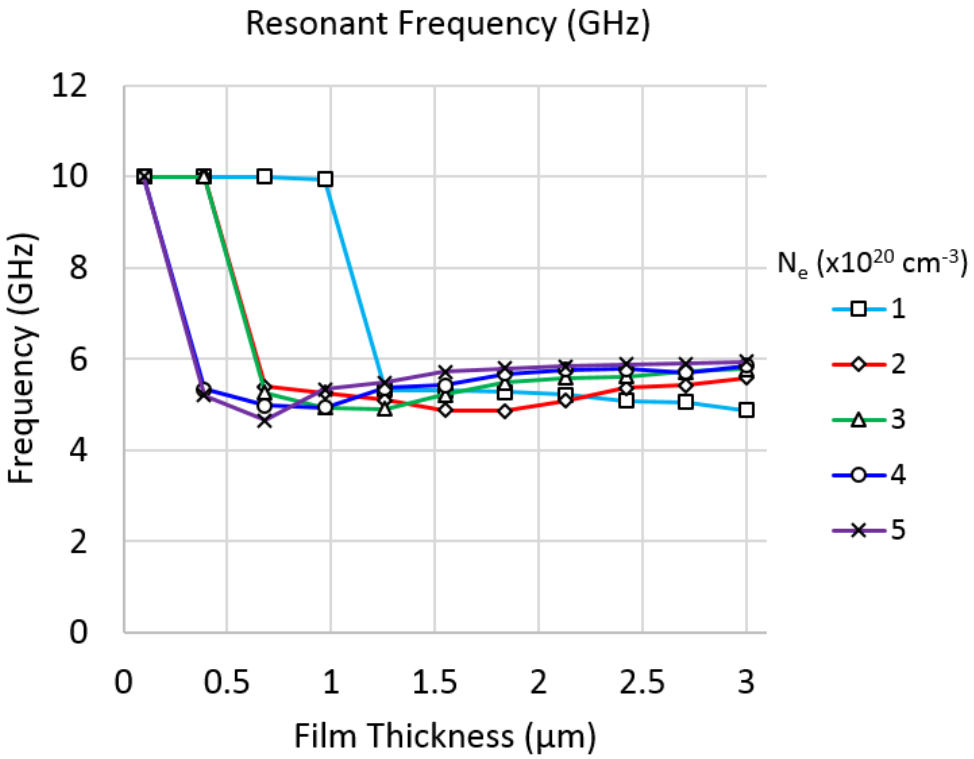

Figure 41 Simulated resonant frequency for bowtie slot antenna versus carrier concentrations and film thicknesses.

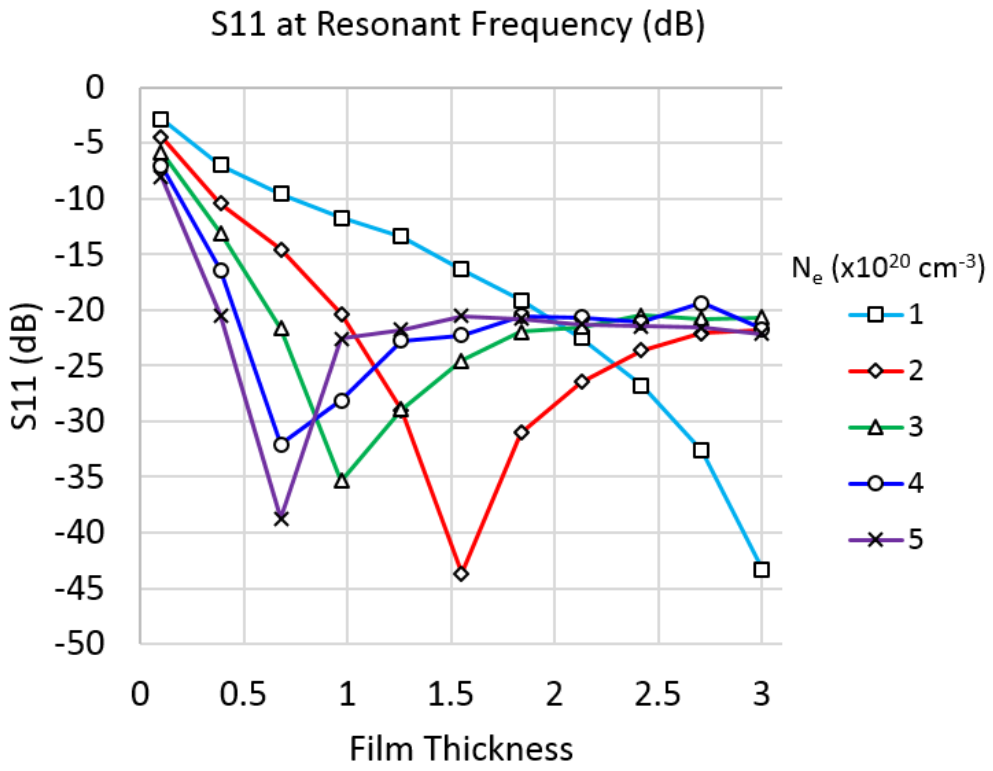

Figure 42 Simulated return loss value at resonant frequency (per Figure 41) for bowtie slot antenna.

Using the same simulation profile mentioned above, the antennas were studied for their simulated antenna gain and efficiency changes. The gain versus film thickness is shown in Figure 43 and the antenna efficiency is shown in Figure 44. Comparable to the hourglass antenna gains, all gains simulated for the bowtie slot antennas at 5.8 GHz were below 0 dBi. The antenna efficiencies are also very low with all efficiencies below 35%.

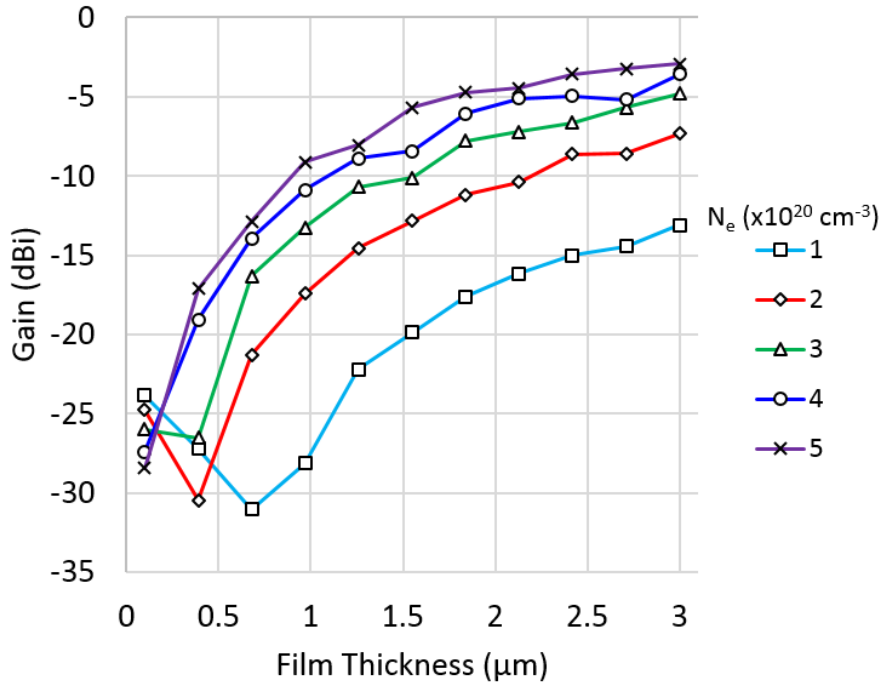

Figure 43 Simulated gain of bowtie slot antenna for various carrier concentrations and film thicknesses.

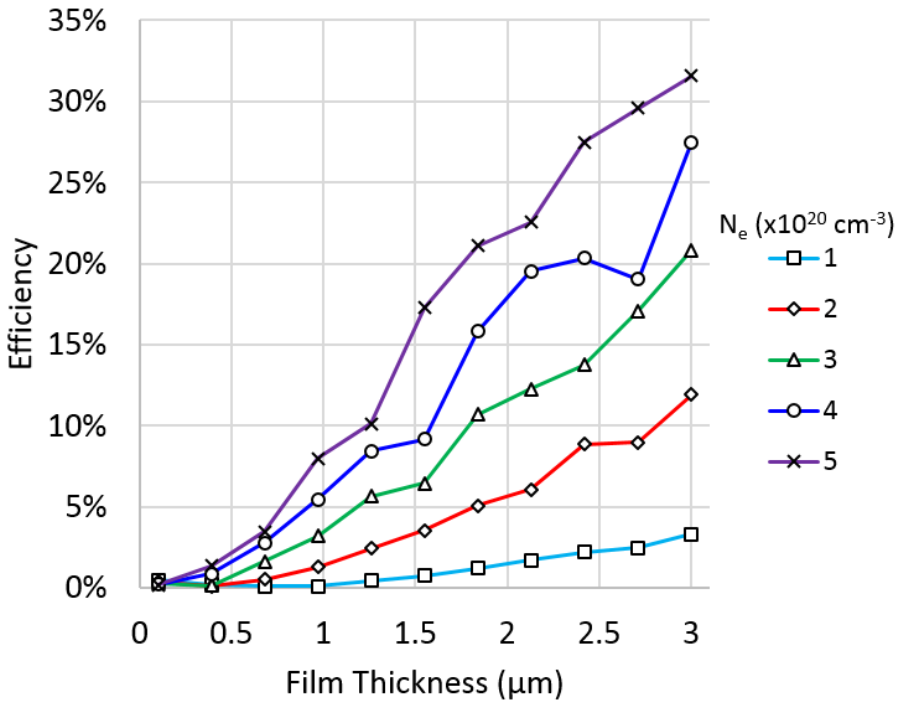

Figure 44 Simulated antenna efficiency of bowtie slot antenna design for various carrier concentrations and film thicknesses.

Using the efficiency in Figure 44 and the transparency determined from chapter 2, the bowtie slot antenna's figure of merit is shown below in Figure 45. The figure of merit here shows

a similar pattern to that of the hourglass antenna in that after a certain carrier concentration, there exists a local maximum figure of merit. The antenna designed shows that the antenna efficiency is so low, that the Figure of merit is much lower than that compared to the dipole and hourglass antenna. This figure suggests that for every carrier concentration below $5x10^{20}$ cm^{-3}, the film should be grown all the way to 3 µm or thicker to counter the in efficiency at the cost of the transparency.

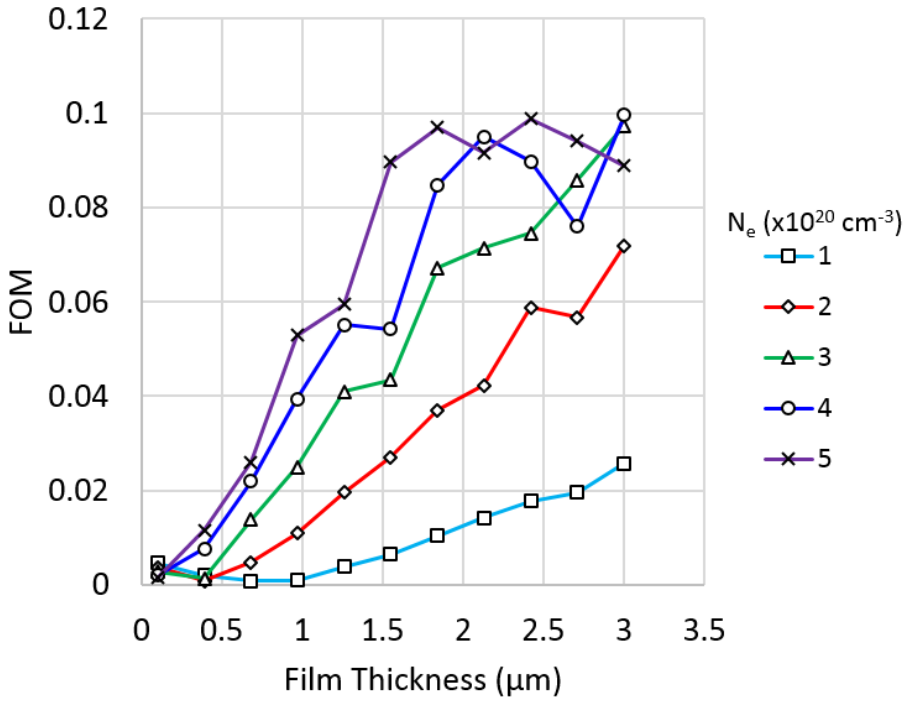

Figure 45 Simulated antenna figure of merit for bowtie slot antenna design for various carrier concentrations and film thicknesses.

The next step in the study of the planar hourglass antenna is the fabrication and measurement of the topology. A GZO film was grown by plasma enhanced molecular beam epitaxy (P-MBE) on a two-inch diameter, 375 µm thick c-sapphire substrate. Prior to loading into the MBE system, the substrate was degreased with acetone and methanol followed by rinsing with deionized water and blowing with nitrogen. After loading to the growth chamber, the sapphire substrate was pre-exposed to oxygen plasma at 750 °C for 30 min at a reactor pressure 1.5×10^{-6}

Torr. First, a 2-nm-thick wurtzite MgO layer was grown at 700 °C, followed by a 15-nm-thick low-temperature (LT) ZnO buffer layer grown at 300 °C and a Zn flux of 0.01 nm/s. During both the MgO and the LT ZnO buffer layer growth, the oxygen gas flow was kept at 0.3 sccm, which corresponds to 5.5×10^{-6} Torr reactor pressure. After annealing the LT-ZnO layer at 700 °C for 5 min at 5.5×10^{-6} Torr reactor pressure with closed O-plasma shutter, ZnO growth proceeded at 620 °C with 0.025 nm/s Zn flux and 0.5 sccm oxygen gas flow for 10 min to obtain a high-quality ZnO buffer for subsequent GZO growth. The substrate was then cooled down to 350° C for the growth of GZO layer. The Ga cell temperature was maintained at 535 °C, which corresponds to a doping level of ~ 4×10^{20} cm^{-3} ($\sigma = 3\times10^{5}$ S/m). The growth of GZO layer was carried out at highly Zn-rich conditions for 12 hours, and total film thickness was ~1 μm, as measured by an alpha-step profilometer. The GZO films were patterned using a photolithography process, as shown schematically in Figure 27. Next, a 200 nm layer of Titanium Gold (Au/Ti) was grown on the GZO film and etched to leave a soldering pad and outline around the substrate. The purpose of this Au/Ti is to provide a visual soldering base for the coaxial connector to feed the antenna. The other purpose of the Au/Ti is to provide an outline to make scoring the sapphire substrate easier. The process includes pattern generation in photoresist, exposure, development, and etching. The antenna was fed with a right angle SMA jack (Digi-Key A118077CT-ND) with silver conductive epoxy (MG Chemicals 8330S-21G) adhering the jack to the Au/Ti film. The resulting antenna is shown below in Figure 46. The transparency of the GZO film for this antenna is comparable to the transparency of that of the previous antennas discussed in this chapter. The simulated results and measured results of four fabricated antennas are shown below in Figure 47. The resonant frequency simulated shows a resonance at 5 GHz while the measured results show a resonance between 7.5 GHz and 8 GHz. This shift can be due to several reasons including feeding mismatches and the

non-transparent Au/Ti outline around the antenna. Despite the frequency shift, the antennas possess an S_{11} at 5.75 GHz between -12 dB and -14 dB and an S_{11} at 5.85 GHz between -12 dB and -15 dB. These antennas fabricated were used to validate an optically transparent antenna array in Chapter 4.

Figure 46 Fabricated 5.8 GHz Bowtie Slot Antenna.

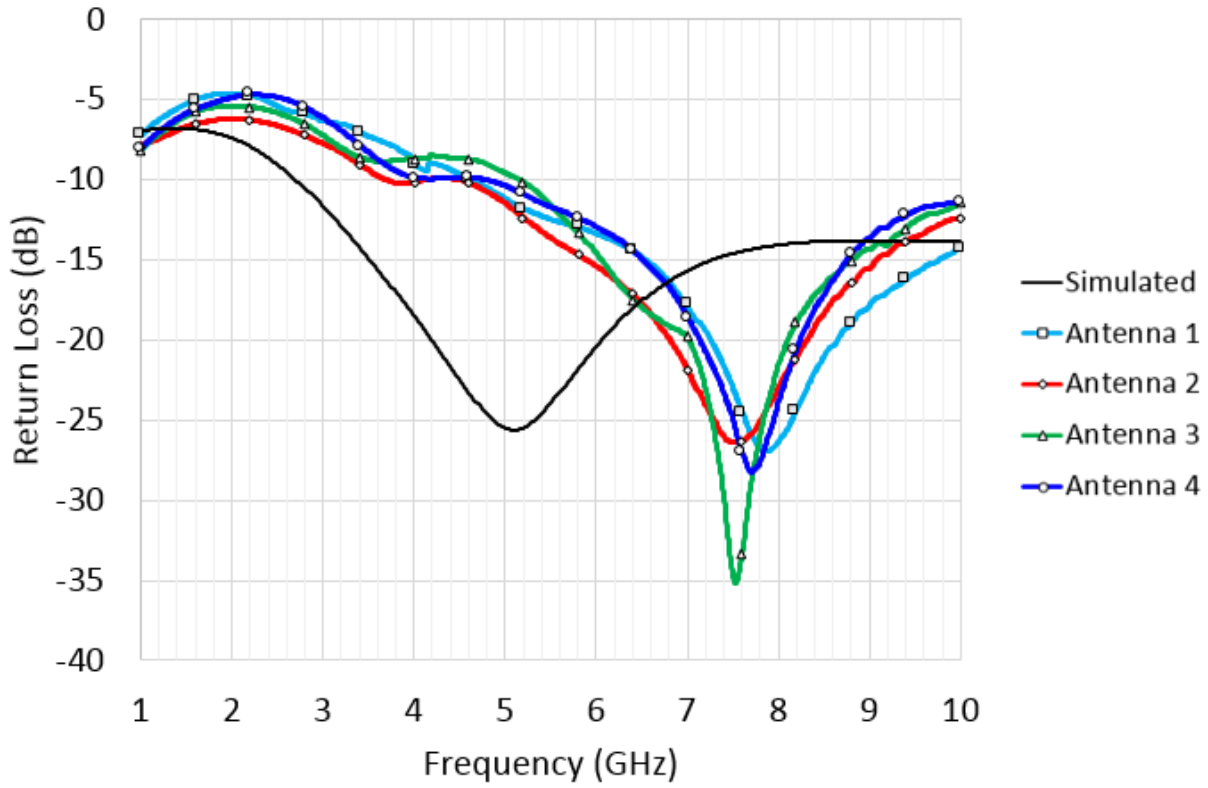

Figure 47 Return loss for the GZO bowtie slot antenna.

3.4 Discussion

In this chapter, a brief background is given on antenna testing, antenna gain, and how thin films affect performance. Moreover, this chapter presents three designs of optically transparent antennas and are compared. In each case, the antenna efficiency is maximized when the carrier concentration and the film thickness is maximized. However this process decreases antenna transparency. This give and take yields a figure of merit (presented for each antenna design). Each figure of merit shows there to be an optimum film thickness for each carrier concentration. In general, this figure of merit shows an optimal film thickness at 1.5 μm for concentrations between $3x10^{20}$ cm^{-3} and $4x^{20}$ cm^{-3}. The while the efficiency and transparency can be optimized, this does not yield antenna gains comparable to that of antenna made from thicker copper sheets. As a result these optimized film thicknesses determined by the figure of merit produce antenna gain consistently below 0 dBi. These low gains can be countered with more antenna elements placed in a periodic structure to increase the overall gain. This method is explored in Chapter 4.

Chapter 4: Transparent Periodic Structures using Gallium-Doped Zinc Oxide Thin Films

4.1 Introduction

The main objective of this chapter is to study the efficacy and performance of transparent periodic structures. Periodic structures is a term in electromagnetics to refer to devices that are constructed of a patterned sub structure. Periodic structures take the form of various commonly used electromagnetic devices such as phased arrays [101], frequency selective surfaces [98], and reflect arrays [102]. In the case of phased arrays, their uses extend from wireless communication applications with their utilization in smart antennas [97] to military applications for radar. Frequency selective surfaces see applications including the screen on microwave oven windows to radome applications for military [103]. Periodic structures, in traditional designs, are used with thick conductors (thickness much greater than the skin depth) and with materials such as copper. The use of TCOs are expected to affect the performance of periodic structures of antenna arrays and FSSs, much like that for the design of antenna elements discussed in Chapters 2 and 3. In this chapter, two frequency selective surfaces are designed, fabricated, and tested. Furthermore, the bowtie slot antenna designed in Chapter 3 was used to characterize the performance of a beam steering antenna array.

4.2 Frequency Selective Surfaces

Frequency Selective Surfaces (FSS) are any surface designed to filter planar electromagnetic waves [97]. A common construction of an FSS is a planar design and typically embedded in some dielectric material. Traditionally, FSSs have had military (radomes) or antenna subassembly (dichroic sub reflectors and reflect array lenses) applications [97]. The FSS consists of a conductive periodic array of solid conductor/antennas arranged in a predictable and repeatable pattern in a one or two dimensional fashion. Depending on the shape of the conductor, the FSS can reflect certain frequencies and allow others to be transmitted through. Several different geometries have ben researched in the 60 year history of FSSs. These different shapes can usually be classified into four different groups.

The first group according to Munk, is the Centered Connected (or N-Pole) topologies. These shapes tend to consist of a dipole design that has been altered in either inter element spacing or bent to follow different shapes. This group can be subdivided into several different types including “Gang Buster” which consist of dipoles arrayed with some offset for a cascading effect. The Gang Buster style is often used as a polarizer [99] because straight dipoles oriented in the same direction polarize incoming electric fields linearly. While the “Gang Buster” style has a linear polarization effect, the unloaded tripole (tripole without end stubs) can operate well under multiple polarization schemes. The tripole also has the advantage of being able to be compact tightly, yielding a higher bandwidth [98]. Similar in geometry, the loaded tripole (tripole with stubs) is similar to the unloaded tripole, however the shape is relatively small compared to the wavelength and is more broadband than that of its unloaded counterpart. Another topology for this first group is the Jerusalem cross. The shape can be described as a loaded quadpole (4-pole) design. While

the size of the element is large compared to other topologies operating at the same wavelength, the shape is used mainly for narrowband applications. The last element geometry discussed in Munk's book for group one is the square spiral element. Its bandwidth is comparable to that of gangbuster, but has the feature of being able to be made into a reflecting and transparent array [98].

Another group discussed by Munk is the "Loop Type" topologies. This style has a conductive loop that can be shaped into different styles to take advantage of bandwidth and element spacing. Typically the size of these elements are small compared to the resonant wavelength. The circumference/perimeter of loop is equal to the wavelength. "Loop Type" elements are common bandpass elements where the bandwidth is controlled by the thickness of the conductor [99].

The third group Munk discusses is the "Plate Type" FSS topologies. These types of shapes are comprised of solid conductive plates in typically simple shapes such as squares, circles, and hexagons. This group is the earliest and simplest elements studied [99]. Because these are the earliest studied, these topologies not only tend to be large compared to the wavelength, but also have issues with grating lobes (diffracted wave into discrete directions at higher frequencies [99]) as well as a variability in performance on the incident angle [98].

The fourth group discussed by Munk is the catch all group of "Combinations." Naturally in a research setting, simple FSS topologies become more complicated to adjust bandwidth, reduce the relevant size of the element, and to reduce the grating lobes caused by the diffraction grate. In most cases, despite the topology, an FSS can also change have its behavior by making a complementary array.

A complementary array can be described as the shape corresponding to the original array such that when the original array and the complementary array are put together, a solid conductive

surface is the result. An example is the difference between a dipole array and a slot array. In a Gang Buster surface, a conductive strip of certain dimension exist on a dielectric slab (or equivalent support structure). The complementary array of this dipole array is a conductive surface on a dielectric slab (or equivalent support structure) with the same shape in the dipole array etched away from the conductive surface. The reflection properties of an FSS equals the transmission properties of the complementary array [98]. This means that if a particular design shows the behavior associated with a bandpass filter, in ideal circumstances (conductor with infinite conductivity and infinitely thin [98]) the complementary array will show behavior of that of a band stop filter.

The topology used for this study is a Jerusalem Cross (Figure 48 (a)). This topology was chosen due to its cross polarization behavior and its understandable geometry and equivalent circuit. Below in Figure 48 (b) is the Jerusalem cross equivalent circuit. As an electromagnetic wave encounters the FSS, the electric wave encounters both conductive and dielectric boundaries. These boundaries can be represented as inductors and capacitors. If the electric field is traveling along a conductor with particular length and width, the equivalent circuit element is the inductor. It the electric field travels across the dielectric gap with particular conductor width, conductor length, and gap width, the equivalent circuit element is the capacitor. The arrangement of the inductors and capacitors for the periodic array motif can be used to calculate the equivalent circuit where L_g is the inductance along the length of the cross, C_{ga} is the capacitance between the gap, and L_d is the inductance of the substrate.

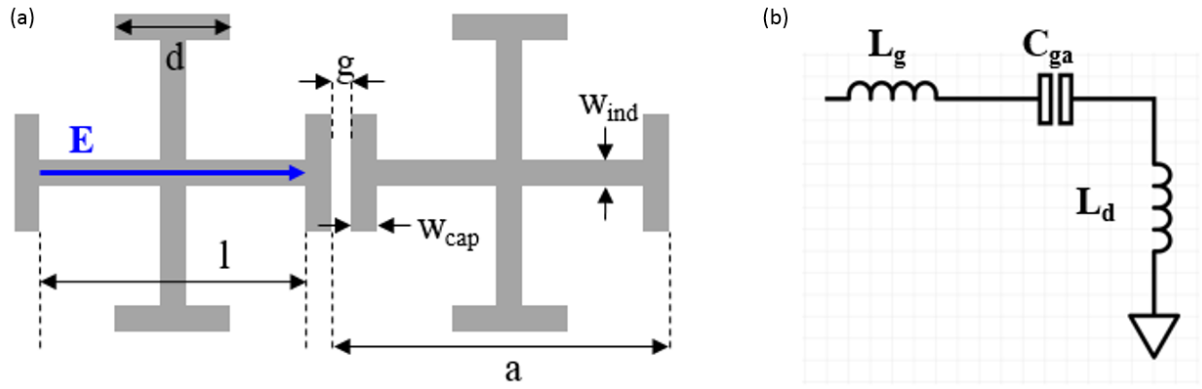

Figure 48 Jerusalem cross frequency selective topology (a) design template with electric field direction specified (b) Equivalent circuit of Jerusalem cross.

For the Jerusalem cross topology, the capacitance C_{ga} is calculated equation (4.1) [100]. In this formula, ε_0 is the free space permittivity, ε_{re} is the effective permittivity, $K(k)$ and $K'(k)$ are the complete elliptic integral and its complement respectively, and d is the length of the stub,

$$C_{ga} = 2\varepsilon_0\varepsilon_{re}\frac{K(k)}{K'(k)}d. \tag{4.1}$$

The ratio of the elliptical integral to its complementary is calculated in equation (4.2) [100],

$$\frac{K(k)}{K'(k)} = \begin{cases} \frac{1}{\pi}\ln\left(2\frac{1+\sqrt{k}}{1-\sqrt{k}}\right), & 0.707 \le k \le 1 \\ \frac{\pi}{\ln(2\frac{1+\sqrt{k'}}{1-\sqrt{k'}})}, & 0 \le k \le 0.707 \end{cases}, \tag{4.2}$$

Where k and k' are calculated via equations (4.3) and (4.4) respectively [100].

$$k = tan^2\left(\frac{w_{cap}\pi}{4(w_{cap}+g)}\right) \tag{4.3}$$

$$k' = \sqrt{1-k^2} \tag{4.4}$$

The effective relative permittivity is calculated in equation (4.5) [100]. The variable w refers to the width of the copper line. For the calculation of C_{ga}, this w value corresponds to w_{cap}.

$$\varepsilon_{re} = \frac{\varepsilon_r+1}{2} + \frac{\varepsilon_r-1}{2}F\left(\frac{w}{h}\right) \tag{4.5}$$

Where $F(w/h)$ is calculated below in equation (4.6).

$$F\left(\frac{w}{h}\right) = \begin{cases} \left(1+\frac{12h}{w}\right)^{-\frac{1}{2}} + 0.041\left(1-\frac{w}{h}\right)^{2}, & \frac{w}{h} \leq 1 \\ \left(1+\frac{12h}{w}\right)^{-\frac{1}{2}}, & \frac{w}{h} \geq 1 \end{cases}. \tag{4.6}$$

The inductance of the cross length L_g is calculated in the equation (4.7) [100]. In this formula, η is the characteristic impedance, ε_{re} is the effective relative permittivity, c is the speed of light, and l is the length of the cross (stub to stub).

$$L_g = \frac{\eta\sqrt{\varepsilon_{re}}}{c} l \tag{4.7}$$

The characteristic impedance is calculated in equation (4.8) [100]. In this formula, η_0 is the free space characteristic impedance ($\eta_0 \approx 120\pi$), ε_{re} is the effective relative permittivity, h is the thickness of the dielectric substrate, and w_{ind} is the thickness of the cross grid. In this particular scenario, the ε_{re} value is calculated using the w_{ind} value for w instead of w_{cap} as before,

$$\eta = \begin{cases} \frac{\eta_0}{2\pi\sqrt{\varepsilon_{re}}} \ln\left(\frac{8h}{w_{ind}} + \frac{w_{ind}}{4h}\right), & \frac{w_{ind}}{h} \leq 1 \\ \frac{\eta_0}{\sqrt{\varepsilon_{re}}}\left(\frac{w_{ind}}{h} + 1.393 + 0.667\ln\left(\frac{w_{ind}}{h} + 1.444\right)\right)^{-1}, & \frac{w_{ind}}{h} \geq 1 \end{cases}. \tag{4.8}$$

The inductance of the dielectric is calculated below in equation (4.9) [100]. In this formula μ_0 is the free space permittivity and h is the thickness of the dielectric substrate.

$$L_d = \mu_0 h \tag{4.9}$$

With the values of L_d, L_g, and C_{ga}, the impedance can be calculated. Since the equivalent circuit shows two inductors and one capacitor in series, the equivalent impedance can be found using equation 4.10 below. In this formula ω is the angular frequency ($\omega = 2\pi f$).

$$Z_S(\omega) = Z_L(\omega) + Z_D(\omega) + Z_C(\omega) = j\left(\omega L_g + \omega L_d - \frac{1}{\omega C_{ga}}\right) \tag{4.10}$$

Equations (4.11) and (4.12) below shows how to calculate the reflection and the transmission coefficients [87] of the FSS using Z_S.

$$\Gamma = \frac{Z_S - \eta_0}{Z_S + \eta_0} \tag{4.11}$$

In this equation, η_0 is the free space impedance. The transmission coefficient is calculated simply with the following equation.

$$\tau = 1 - \Gamma \tag{4.12}$$

Two FSSs, band-pass and band-stop filters, were designed to operate between 23 GHz to 29 GHz. Due to its wideband behavior, the Jerusalem Cross topology was employed for both filters. The band-pass filter was designed to have a solid GZO layer with the Jerusalem Cross openings etched in the film. The design of the band-stop filter is an inverted pattern of the band-pass filter: the Jerusalem Crosses were composed of GZO, while the rest of the film was etched away, as shown in Figure 27.

4.2.1 Band Pass Filter

The first filter design discussed is the band pass filter. The band pass filter design is shown below in Figure 49 and the design attributes are shown below in Table 5.

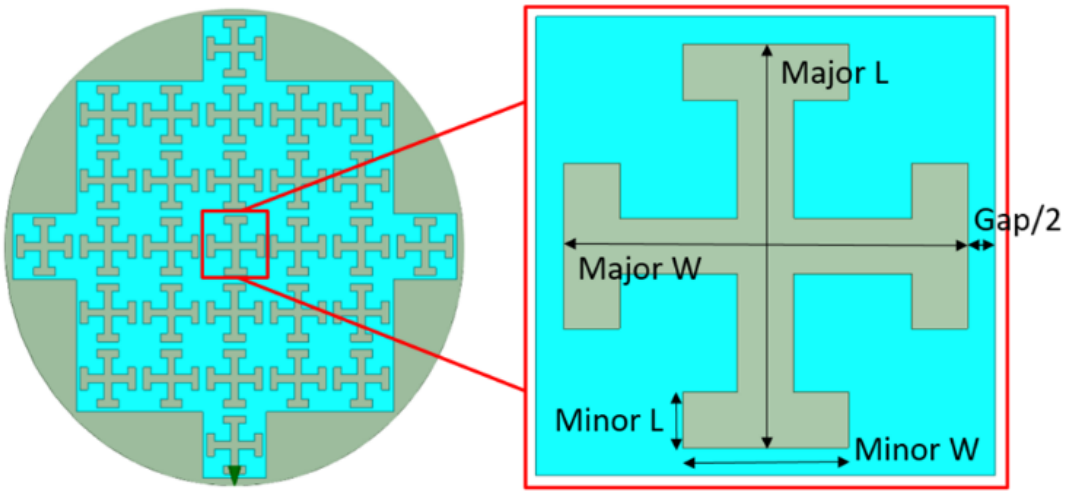

Figure 49 Fabricated Band Pass Filter.

Table 5 Band pass filter design attributes.

Design Attribute	Value (mm)
Major L	6.15
Major W	6.15
Minor L	0.85
Minor W	2.40
Gap	0.85

The simulated return loss of the band pass filter is shown below in Figure 50. The initial design was assumed to have a carrier concentration of $N_e = 4\text{x}10^{20}$ cm^{-3}, an electron mobility of $\mu_e = 31$ cm^2/V·s, and a film thickness of 1.5 μm. The simulations show an insertion loss of -4.89 dB at 28.6 GHz.

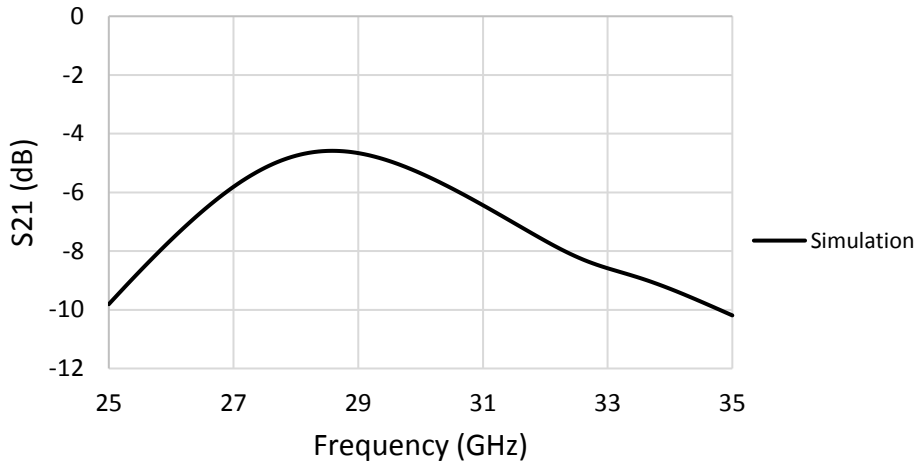

Figure 50 Simulated transmission of band pass filter.

Much like the antenna simulations, the resonance of the filter is expected to change as the material properties change. The band pass filter design was simulated using the same simulation profile used with the antenna simulations ($1\text{x}10^{20} \leq N_e \leq 5\text{x}10^{20}$ cm^{-3}, $0.1 \leq$ thickness ≤ 3 μm). The insertion loss (S_{21}) results are shown below in

Figure *51*. The results show an interesting result, in that at low film thicknesses, the S_{21} lowers as the carrier concentration is increased, but at higher film thicknesses, a resonance is seen,

and that value rises as the carrier concentration is increased the resonance possesses a lower S_{21}. This is due to the sheet resistance of the film, and in conjunction the resistivity, lowering as the carrier concentration and the film thickness increased. Without a pattern, the S_{21} of the films would continue to lower. With a pattern, this allows for the Jerusalem cross to act more and more as a frequency selective surface, producing a resonance at 28.5 GHz.

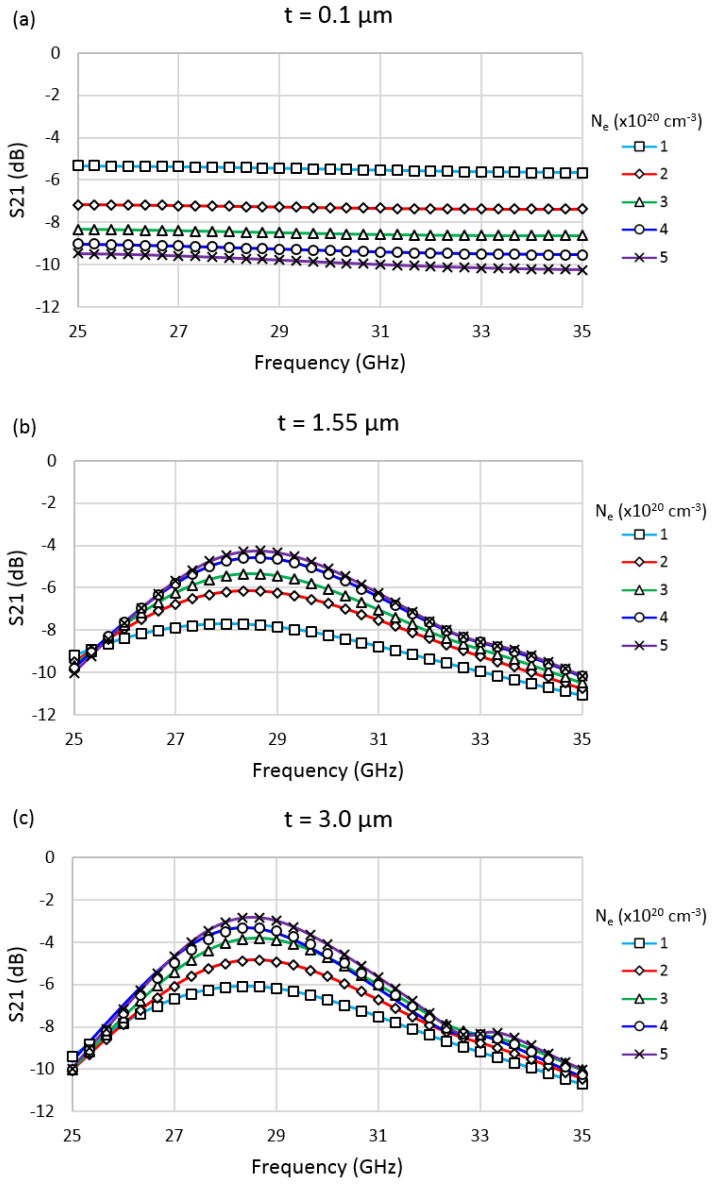

Figure 51 Simulated transmission for band pass filter (a) S_{21} at thickness of 0.1 µm for various carrier concentrations (b) S_{21} at thickness of 1.55 µm for various carrier concentrations (c) S_{21} at thickness of 3.0 µm for various carrier concentrations.

The next step taken was to fabricate and test the band pass filter topology. A GZO film was grown by plasma enhanced molecular beam epitaxy (P-MBE) on a two-inch diameter, 375 μm thick c-sapphire substrate. Prior to loading into the MBE system, the substrate was degreased with acetone and methanol followed by rinsing with deionized water and blowing with nitrogen. After loading to the growth chamber, the sapphire substrate was pre-exposed to oxygen plasma at 750 °C for 30 min at a reactor pressure 1.5×10^{-6} Torr. First, a 2-nm-thick wurtzite MgO layer was grown at 700 °C, followed by a 15-nm-thick low-temperature (LT) ZnO buffer layer grown at 300 °C and a Zn flux of 0.01 nm/s. During both the MgO and the LT ZnO buffer layer growth, the oxygen gas flow was kept at 0.3 sccm, which corresponds to 5.5×10^{-6} Torr reactor pressure. After annealing the LT-ZnO layer at 700 °C for 5 min at 5.5×10^{-6} Torr reactor pressure with closed O-plasma shutter, ZnO growth proceeded at 620 °C with 0.025 nm/s Zn flux and 0.5 sccm oxygen gas flow for 10 min to obtain a high-quality ZnO buffer for subsequent GZO growth. The substrate was then cooled down to 350° C for the growth of GZO layer. The Ga cell temperature was maintained at 535 °C, which corresponds to a doping level of $\sim 4\times10^{20}$ cm^{-3} ($\sigma = 3\times10^{5}$ S/m). The growth of GZO layer was carried out at highly Zn-rich conditions for 12 hours, and total film thickness was ~1 μm, as measured by an alpha-step profilometer. The GZO films were patterned using a photolithography process, as shown schematically in Figure 27. The process includes pattern generation in photoresist, exposure, development, and etching. The resulting filter is shown below in Figure 52.

Figure 52 Fabricated GZO band pass filter with Virginia Commonwealth University College of Engineering Logo for background.

The test setup for the bandpass filter is shown below in Figure 53. The band pass filter was characterized using a network analyzer with two horns, operating between 23 GHz and 35 GHz, placed 10 cm apart. Between the two antennas, an isolator panel, made of a section of 3ft by 3ft piece of galvanized steel with RF absorber placed on the steel plate, is placed. A 1.5 inch diameter hole was drilled through the center of the steel plate and the RF absorber. On the RF absorber side, the horn antenna is placed into a box lined with RF absorber. This antenna is connected to port 2 of a network analyzer. The antenna placed on the steel plate side of the isolator panel is connected to port 1 of the network analyzer.

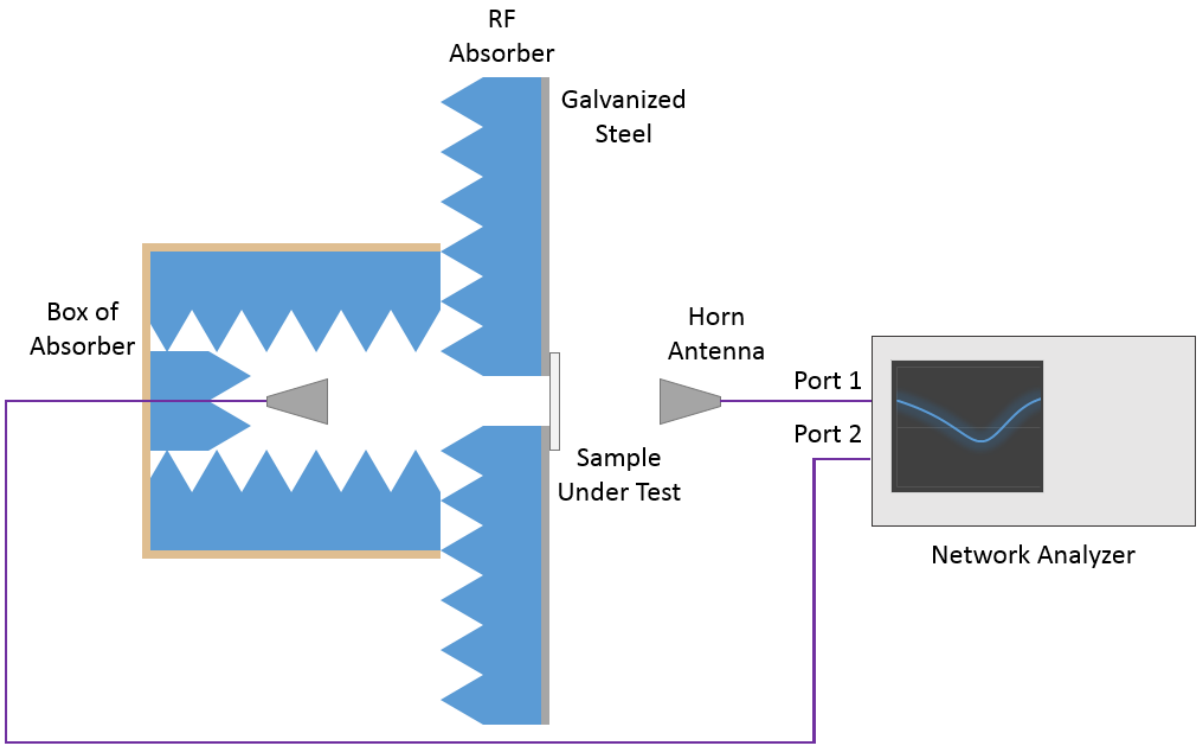

Figure 53 FSS filter test setup.

Before the filter is placed on the isolator panel, a calibration is performed between the two antennas. The network analyzer is set to operate between 23 GHz and 35 GHz, at an output power level of 15 dBm. The network analyzer takes 1601 frequency points between 23 GHz and 35 GHz at an intermediate frequency (IF) bandwidth of 1 Hz. This bandwidth is set low to minimize the noise on the measurement. A response calibration was then performed on the network analyzer for the S_{21} scattering parameter. This takes the current amount of magnitude of the insertion loss at every frequency and sets it to 0 dB. After the calibration, the resulting insertion loss is the loss due to the filter itself.

The results for the band pass filter are shown below in Figure 54. There is a strong correlation between the simulated and the measured results with slight discrepancies. The differences are explained by the finite size of the filter versus the infinite size assumed by the

simulation process. A finite sized filter has frequency shifts and transmission changes compared to the infinite size. Despite these differences, there is a strong correlation between the simulated and measured results.

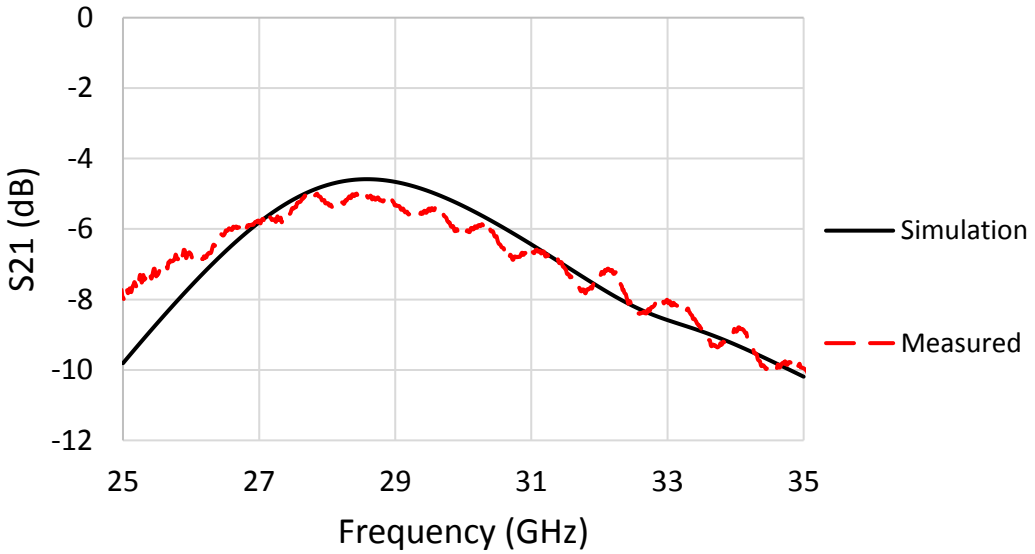

Figure 54 Insertion loss of band pass filter.

4.2.2 Band Stop Filter

The second filter explored in this study is the band stop filter. The filter design template is shown below in Figure 55 and the design attributes are shown in Table 6.

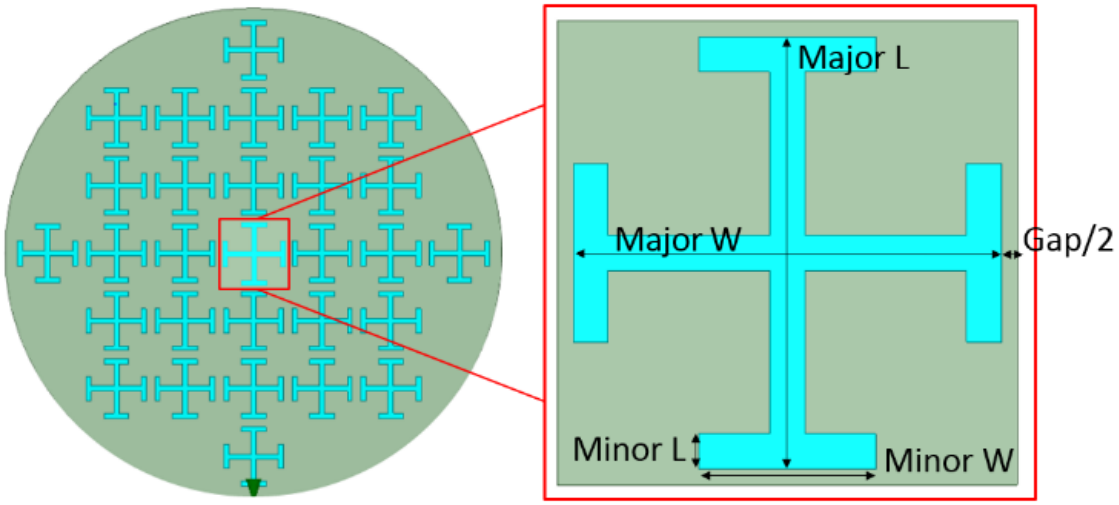

Figure 55 Fabricated Band Pass Filter.

Table 6 Band stop filter design attributes

Design Attribute	Value (mm)
Major L	6.1
Major W	6.1
Minor L	0.5
Minor W	2.515
Gap	0.9

The simulated return loss of the band stop filter is shown below in Figure 56. The initial design was assumed to have a carrier concentration of $N_e = 4x10^{20}$ cm^{-3}, an electron mobility of $\mu_e = 31$ $cm^2/V{\cdot}s$, and a film thickness of 1.5 μm. The simulations show an insertion loss of -12.38 dB at 27.7 GHz.

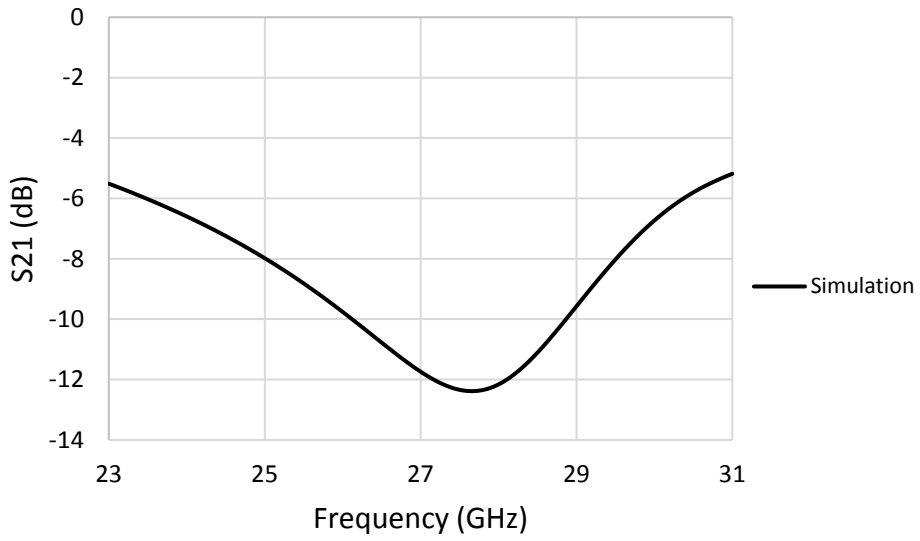

Figure 56 Simulated transmission of band stop filter.

Similar to the changes seen in the band pass filter, the resonance of the filter is expected to change as the material properties change. The band pass filter design was simulated using the same simulation profile used with the antenna simulations ($1x10^{20} \leq N_e \leq 5x10^{20}$ cm^{-3}, $0.1 \leq$ thickness $\leq$ 3 μm). The insertion loss (S_{21}) results are shown below in Figure 57. The results show that at low film thicknesses, the S_{21} lowers as the carrier concentration is increased, but at higher film thicknesses, a resonance is seen, and that transmission value lowers as the carrier concentration is

increased the resonance possesses a lower S_{21}. This is due to the sheet resistance of the film, and in conjunction the resistivity, lowering as the carrier concentration and the film thickness increased. Without a pattern, the S_{21} of the films would continue to lower. With a pattern, this allows for the Jerusalem cross to act more and more as a frequency selective surface, producing a resonance at 27.5 GHz.

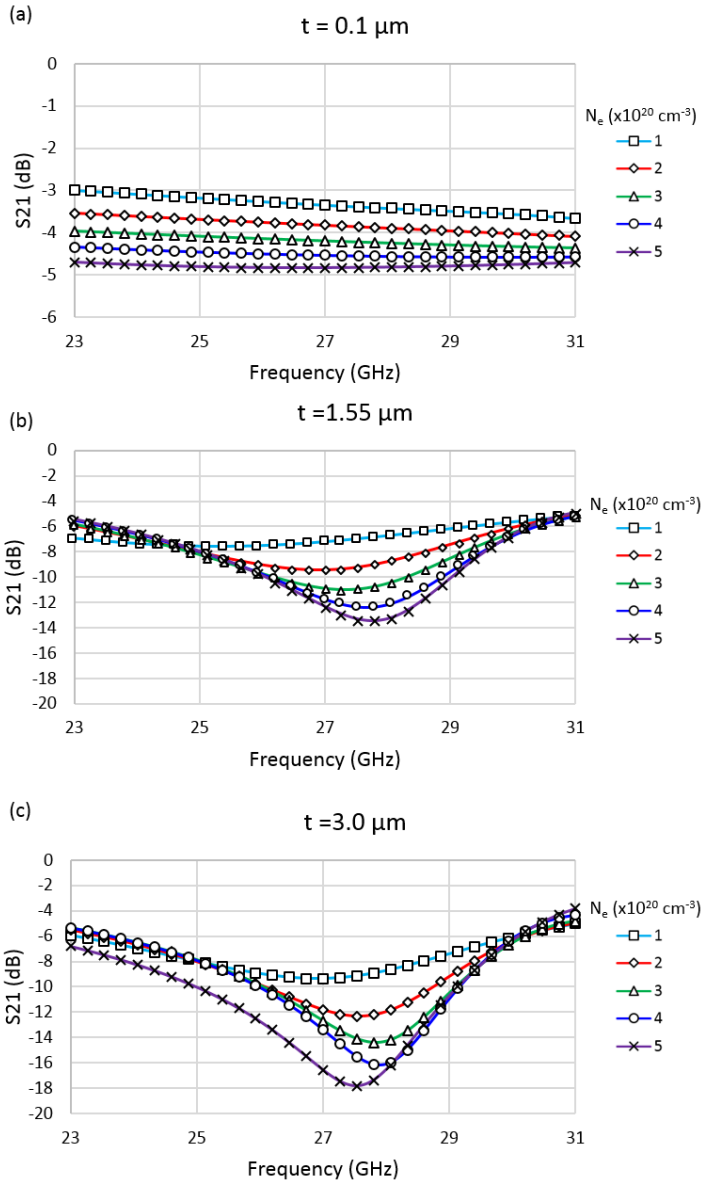

Figure 57 Simulated transmission for band stop filter (a) S_{21} at thickness of 0.1 µm for various carrier concentrations (b) S_{21} at thickness of 1.55 µm for various carrier concentrations (c) S_{21} at thickness of 3.0 µm for various carrier concentrations.

The next step taken was to fabricate and test the band stop filter topology. A GZO film was grown by plasma enhanced molecular beam epitaxy (P-MBE) on a two-inch diameter, 375 μm thick c-sapphire substrate. Prior to loading into the MBE system, the substrate was degreased with acetone and methanol followed by rinsing with deionized water and blowing with nitrogen. After loading to the growth chamber, the sapphire substrate was pre-exposed to oxygen plasma at 750 °C for 30 min at a reactor pressure 1.5×10^{-6} Torr. First, a 2-nm-thick wurtzite MgO layer was grown at 700 °C, followed by a 15-nm-thick low-temperature (LT) ZnO buffer layer grown at 300 °C and a Zn flux of 0.01 nm/s. During both the MgO and the LT ZnO buffer layer growth, the oxygen gas flow was kept at 0.3 sccm, which corresponds to 5.5×10^{-6} Torr reactor pressure. After annealing the LT-ZnO layer at 700 °C for 5 min at 5.5×10^{-6} Torr reactor pressure with closed O-plasma shutter, ZnO growth proceeded at 620 °C with 0.025 nm/s Zn flux and 0.5 sccm oxygen gas flow for 10 min to obtain a high-quality ZnO buffer for subsequent GZO growth. The substrate was then cooled down to 350° C for the growth of GZO layer. The Ga cell temperature was maintained at 535 °C, which corresponds to a doping level of $\sim 4\times10^{20}$ cm^{-3} ($\sigma = 3\times10^{5}$ S/m). The growth of GZO layer was carried out at highly Zn-rich conditions for 12 hours, and total film thickness was ~1 μm, as measured by an alpha-step profilometer. The GZO films were patterned using a photolithography process, as shown schematically in Figure 27. The process includes pattern generation in photoresist, exposure, development, and etching. The resulting filter is shown below in Figure 58. Note, this particular filter was fabricated on a non-polished sapphire wafer, causing the cloudy nature of the filter. The film itself is transparent and if the substrate were polished, the transparency of the film would be comparable to that of the band pass filter.

Figure 58 Fabricated band stop filter with Virginia Commonwealth University College of Engineering Logo for background.

The test setup for the band stop filter is shown above in Figure 53. The band stop filter was characterized using a network analyzer with two horns, operating between 23 GHz and 35 GHz, placed 10 cm apart. Between the two antennas, an isolator panel, made of a section of 3ft by 3ft piece of galvanized steel with RF absorber placed on the steel plate, is placed. A 1.5 inch diameter hole was drilled through the center of the steel plate and the RF absorber. On the RF absorber side, the horn antenna is placed into a box lined with RF absorber. This antenna is connected to port 2 of a network analyzer. The antenna placed on the steel plate side of the isolator panel is connected to port 1 of the network analyzer.

Before the filter is placed on the isolator panel, a calibration is performed between the two antennas. The network analyzer is set to operate between 23 GHz and 35 GHz, at an output power level of 15 dBm. The network analyzer takes 1601 frequency points between 23 GHz and 35 GHz at an intermediate frequency (IF) bandwidth of 1 Hz. This bandwidth is set low to minimize the noise on the measurement. A response calibration was then performed on the network analyzer for the S_{21} scattering parameter. This takes the current amount of magnitude of the insertion loss at

every frequency and sets it to 0 dB. After the calibration, the resulting insertion loss is the loss due to the filter itself.

The results for the band stop filter are shown below in Figure 59. The measured results show a resonance at 26.13 GHz with a transmission value of -13.6 dB. There is a correlation between the simulated and the measured results with a frequency shift. The differences are explained by the finite size of the filter versus the infinite size assumed by the simulation process. A finite sized filter has frequency shifts and transmission changes compared to the infinite size. Despite these differences, there is a decent correlation between the simulated and measured results.

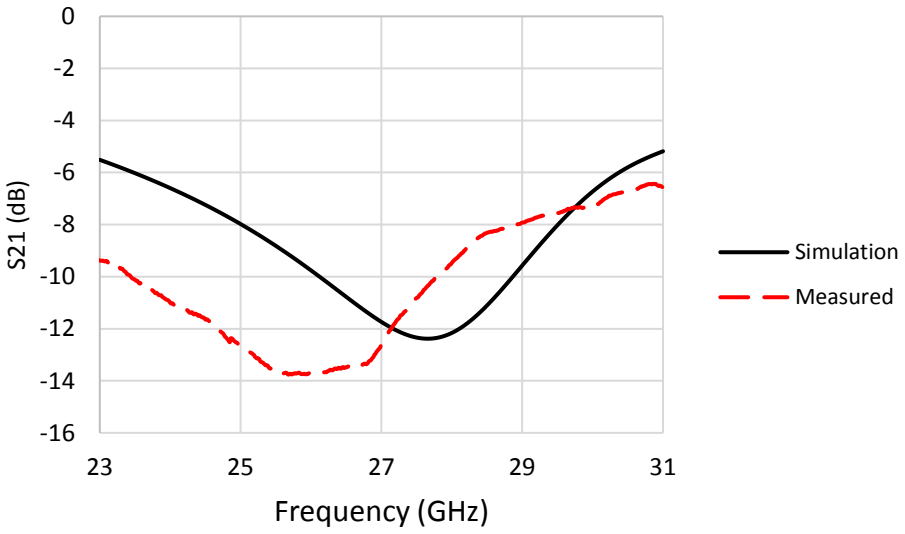

Figure 59 Insertion loss of band stop filter.

4.3 Antenna Array

Antenna arrays are designed as a series of antennas positioned in either a 1 dimensional or 2 dimensional placement to increase the performance of the antenna broadcast to a certain standard that a single element often cannot meet. Such requirements include higher gain, narrow beams, and steerable beams. The elements, if possible, are assumed to be parallel and identical [94]. For

an array, the total far electric field is expressed as the summation of the far electric fields from each antenna within the array at an observation point.

Each antenna array is tested by a link budget analysis test shown in Figure 60. First, a signal generator to a 4 way splitter. Three of the output terminals of the splitter are connected to a phase shifter via a coaxial connector. The output of each phase shifter is connected to a corresponding antenna for channels 1, 2, and 3. The fourth output is connected to the fourth antenna via two coaxial cables connected via a female-to-female SMA adapter to match the attenuation value seen in the phase shifters and cables on the other three antennas. A horn antenna connected to a spectrum analyzer is placed at a distance *D* (2 meters) away and the signal is received and measured. The physical setup of this test is shown in Figure 61. The signal generator is set to broadcast 0 dBm out of the output. The insertion loss between each channel is measured to be -12.25 dB, -12.78 dB, -12.98 dB, and -12.63 dB for channels 1 through 4 respectively. This means that there is an average of -12.66 dB of loss for each channel. The phase shift of the fourth channel is measured via a network analyzer between the input of the splitter and the output to Antenna 4.

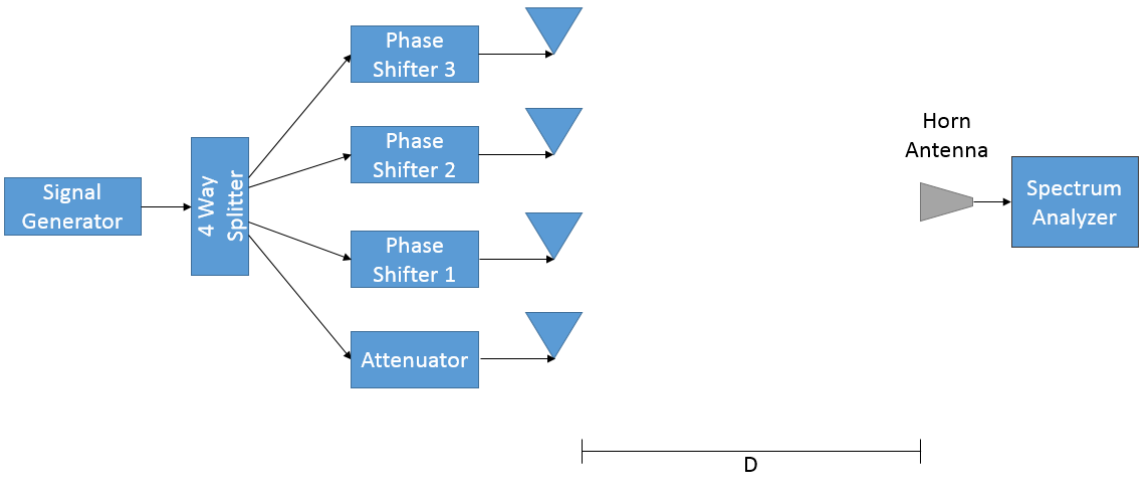

Figure 60 Link Budget Analysis diagram.

Figure 61 Link Budget Analysis physical layout.

Using the Friis formula, in equation R4.13 [94], is used to calculate the Gain of the antennas under test. In this equation P_R is the power received on the receiver antenna (in Watts), P_T is the power transmitted by the antennas under test (in Watts), G_R is the gain of the receiver antenna (scalar), G_T is the gain of the transmitter antenna (scalar), λ is the wavelength broadcast (in meters), and D is the distance between the two antennas (in meters).

$$\frac{P_R}{P_T} = G_R G_T \left(\frac{\lambda}{4\pi D}\right)^2 \tag{4.13}$$

Using this formula, if the power transmitted, power received, the gain of the receiver, the distance, and the operation frequency are known, the gain of the transmitter can be calculated. In this test, the power transmitted is set to 0 dBm (1mW) to be output at the antennas under test and the distance is set to be 2 meters. The gain of the horn antenna was measured to be 7.93 dBi (6.21 scalar). Additionally, each antenna and antenna array under test in this chapter are placed on a rotating table with a paper reference underneath for angle placement. Each antenna or array under test were tested between -60° and +60° from boresight at increments of 5°.

To study the efficacy of an optically transparent antenna array for this study a one dimensional array of 4 antennas was investigated. This antenna array was fabricated using the bowtie slot antenna design presented in chapter 3. The array operates on the 5.8 GHz ISM band (5.75 GHz to 5.85 GHz), and its beam steering capabilities are also investigated. In order to do a comparison, a similar antenna was fabricated using copper on Rogers 6006 (ε_r = 10.2) to better replicate the performance of the GZO antenna on a substrate with similar permittivity.

4.3.1 Copper Antenna Array

First, a copper antenna array was designed and developed to be a bench mark for how the GZO array would perform. A similar antenna was designed using copper on Rogers 6006 substrate. Moreover, the antennas were simulated to be applied to a transparent, 0.25 inch acrylic slab (ε_r = 3.4) The shape of the antenna topology is the same as the antenna proposed in Chapter 3 and can be seen in Figure 39. The antenna design attributes are seen below in Table 7. The antenna was simulated on Ansys HFSS and fabricated using an LPKF S103 Milling machine. Four antennas were milled for this study and the simulated and measured return losses are shown below in Figure 62 (b). The Fabricated antennas are shown in Figure 62 (a) in an array pattern and are labeled for channels 1 through 4. The antennas are placed at a distance of a half wavelength (d = 26 mm) apart from center to center.

Table 7 Copper Bowtie slot antenna design attributes

Design Attribute	Value (mm)	Design Attribute	Value (mm)
Arm L	5.86	*Inner W*	2
Cut W	0.6	*Outer W*	6.5
Cut 1 Inner	1.64	*Port Gap*	0.75
Cut 1 Outer	2.1	*Port L*	2.25
Cut 2 Inner	3.29	*Port W*	2.18
Cut 2 Outer	3.75	*Serp W*	1.5
Feed Gap	0.2	*Sub L*	15
Feed L	9.0	*Sub W*	15
Feed W	1.28	*Taper L*	0.5

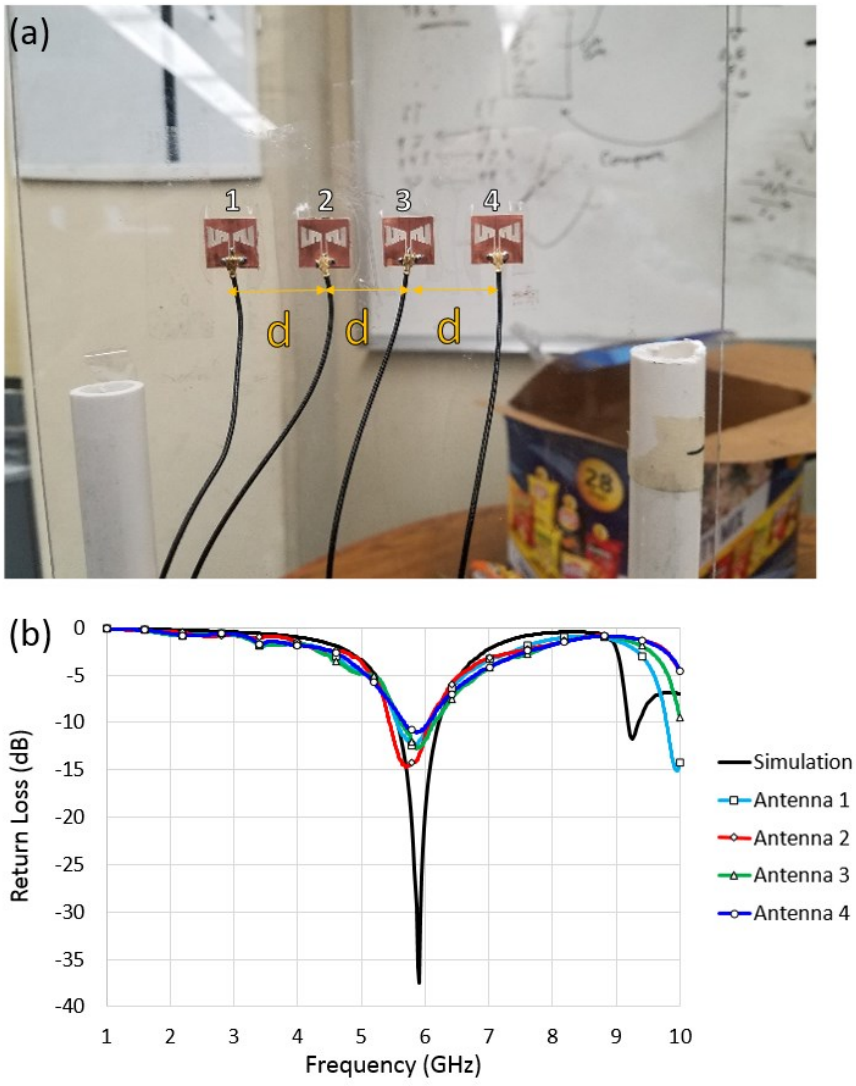

Figure 62 Copper Antenna Array (a) Fabricated Copper Bowtie Slot Antennas in 4x1 array pattern (b) Simulated and measured return loss of copper bowtie slot antennas.

Next, the copper antenna was simulated for the beam steering and measured. In order to test this different phases needed to be applied to each antenna in both the simulation and the physical test bench. The phases applied to the antenna can be calculated via equation 4.14. In this formula $\Delta\phi$ is the change in phase between each antenna element, λ is the wavelength of the frequency being broadcast, d is the distance between the antennas, and Θ is the angle of beam. This concept is also shown below in Figure 63.

$$\Delta\varphi = \frac{2\pi}{\lambda} d \sin\Theta \tag{4.14}$$

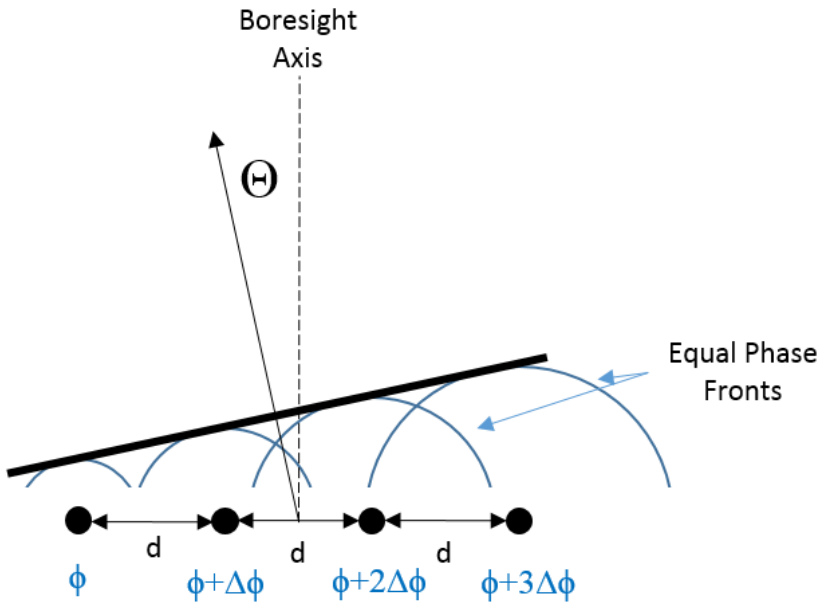

Figure 63 Simulated Antenna gain for copper element and 4x1 array.

In order to have a boresight beam ($\Theta = 0°$), the change in phase is equal to 0, meaning each antenna has the same phase. The simulated results are shown below in Figure 64. In this simulation, the single element antenna has a maximum gain of 2.18 dBi and the maximum gain of the array is 7.77 dBi.

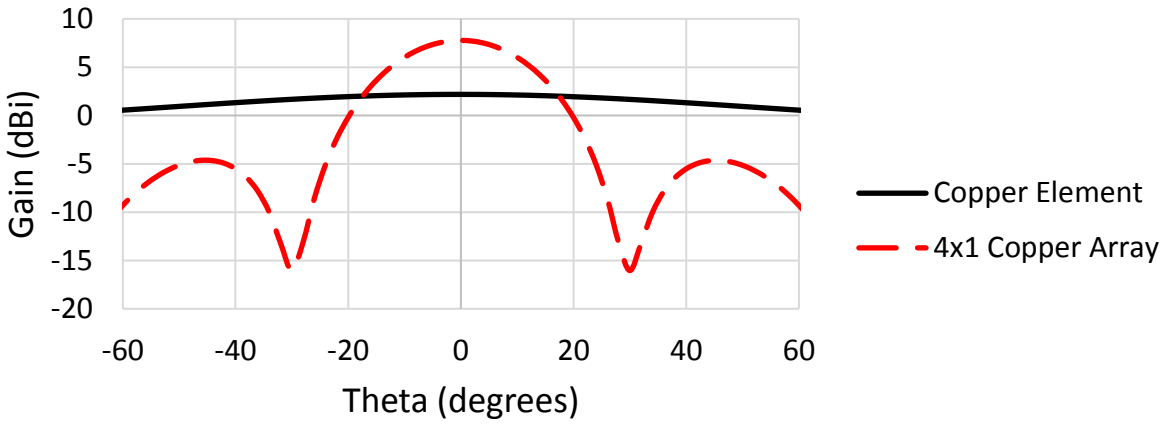

Figure 64 Simulated Antenna gain for copper element and 4x1 array.

Next, a single antenna element was tested in comparison to the fabricated 4x1 copper antenna array. These results are shown below in Figure 65. The copper antenna array was setup to be tested with no phase difference between the 4 antennas. The S_{21} between the input to the splitter and the output to the antenna were measured and the S_{21} phase for Antenna number 4 is -71.36°. The S_{21} for each channel was taken and the phase for each channel was set by tuning the phase shifters to match -71.36°.

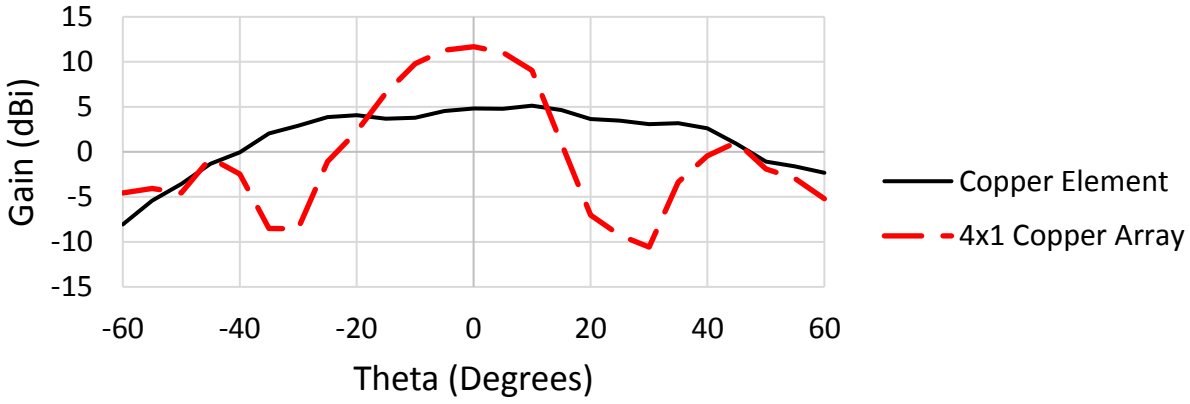

Figure 65 Measured Antenna gain for copper element and 4x1 array.

Next, different $\Delta\phi$ were applied to have a beam angle. Beam angles of -45°, -30°, -20°,-10°, +10°, +20°, +30°, and +45° were applied by adding a phase shift to each antenna in simulation. The phase shifts in Table 8 are shown. Similar to the testing of the copper antenna array with a

boresight beam, the phase shifts shown in Table 8 were applied to each antenna to create various beam angles and were tested for its gain. The antenna array was rotated on an azimuth table at 5° increments between -60° from boresight to +60° from boresight. The recorded received power was used to calculate the gain. The results of these simulated and measured beam angles (gain) are shown in Figure 66.

Table 8 Phase shifts (Δφ) applied to achieve beam angle (Θ).

Θ (degrees)	Δϕ (mm)
-45	-127.28
-30	-90.00
-20	-61.56
-10	-31.26
0	0.00
+10	31.26
+20	61.56
+30	90.00
+45	127.28

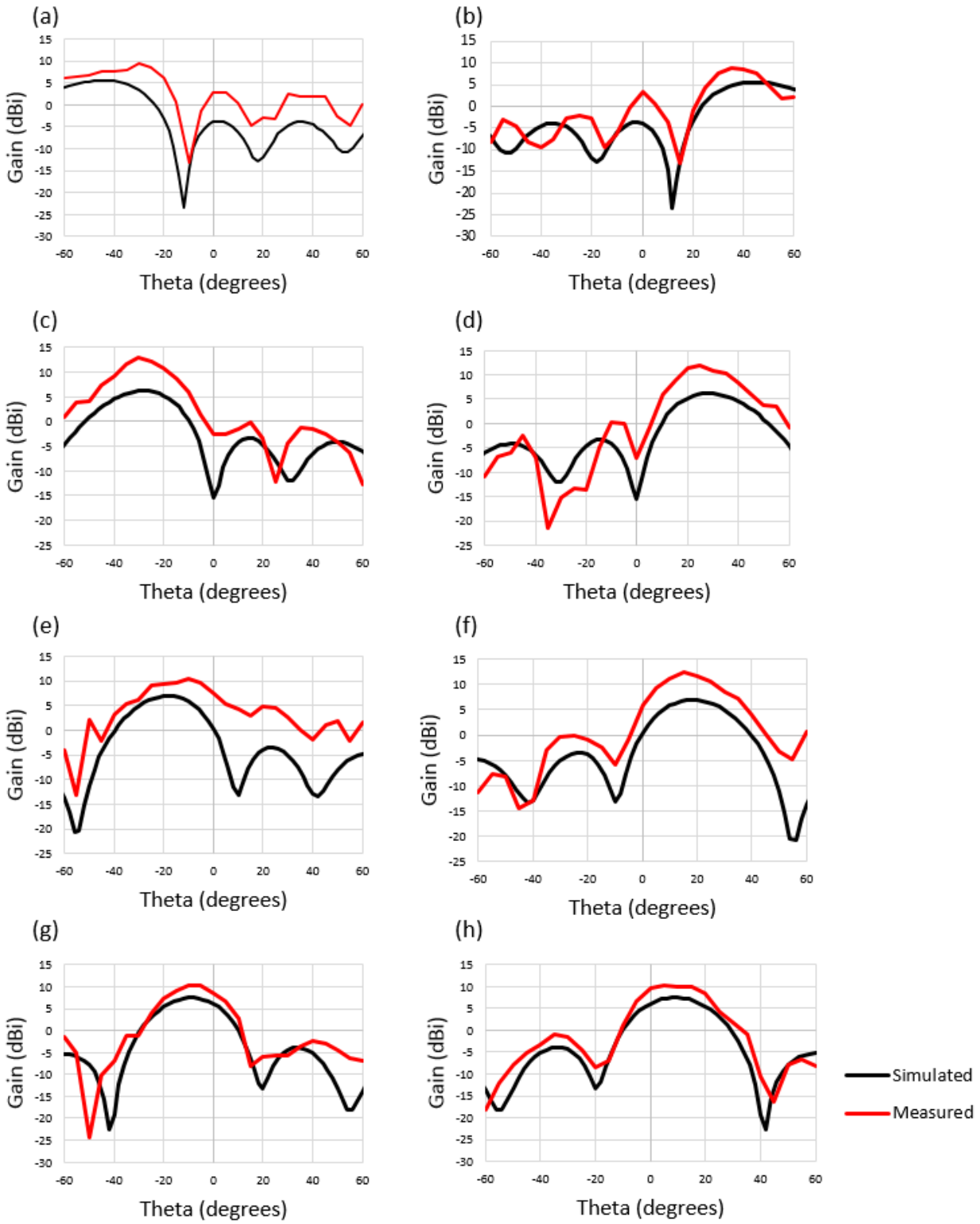

Figure 66 Simulated and measured copper array beam steering for various beam angles. (a) -45° beam angle, (b) +45° beam angle, (c) -30° beam angle, (d) +30° beam angle, (e) -20° beam angle, (f) +20° beam angle (g) -10° beam angle (h) +10° beam angle

While there is a slight increase in gain between the simulated and measured results, each beam steering angle shows a good correlation between the expected and measured results. This discrepancy between simulated and measured results may be due to reflections present in the class room setting the array was tested. The antenna array of four antennas adequately beam forms on angles between -45° and +45°. This array will be used for comparison to the GZO Array for gain and beam forming capability.

4.3.2 GZO Antenna Array

Next, an antenna array was designed using the GZO antennas fabricated in Chapter 3. The antenna design is a bowtie slot antenna on a 375 μm thick sapphire substrate ($\varepsilon_r = 10$). The antenna elements are placed on a transparent, 0.25 inch acrylic slab ($\varepsilon_r = 3.4$). Since the array is made of thin films, it is expected that the film material properties would affect the array characteristics. The array and antenna elements were simulated for their gain for various values of the carrier concentration ($N_e = 1\text{x}10^{20}$ cm^{-3}, $3\text{x}10^{20}$ cm^{-3}, and $5\text{x}10^{20}$ cm^{-3}) and film thicknesses ($t = 0.1$ μm, 1.55 μm, and 3.0 μm). The results of this simulation are shown below in Figure 67 and Figure 68. In Figure 67, the carrier concentration is kept at $3\text{x}10^{20}$ cm^{-3}, and the thickness of the film is swept. As expected the gain for both the array and the element increases as the film thickness increases, decreasing the resistance of the film. Each pairing shows an increase of over 6 dBi between the antenna elements to the 4x1 arrays. For the thickness of 0.1μm, the array shows a 6.2 dBi increase over the antenna element gain. For the thickness of 1.55 μm, the array shows a 7.57 dBi increase over the antenna element gain. For the thickness of 3.0 μm, the array shows a 6.36 dBi increase over the antenna element gain. In Figure 68, the carrier concentration is swept while the thickness

of the film is held at 1.55 μm. As expected, the gain for both the array and the element increases as the carrier concentration increases, increasing the conductivity of the film. Each paring shows an increase over 3 dBi between the antenna elements to the 4x1 arrays. For the carrier concentration of $1x10^{20}$ cm^{-3}, the array shows a 3.1 dBi increase over the antenna element gain. For the carrier concentration of $3x10^{20}$ cm^{-3}, the array shows a 7.57 dBi increase over the antenna element gain. For the carrier concentration of $1x10^{20}$ cm^{-3}, the array shows a 6.25 dBi increase over the antenna element gain.

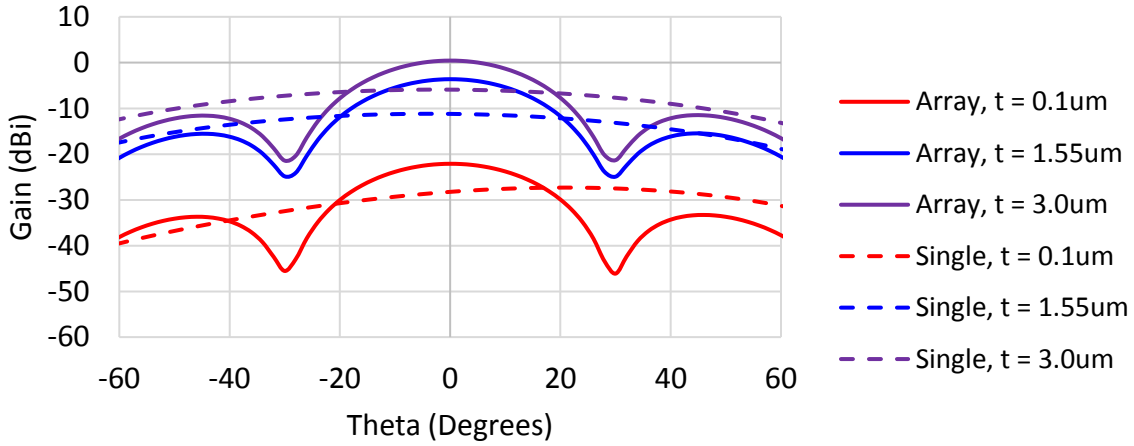

Figure 67 Simulated Gain versus Theta for array and element for N_e = $3x10^{20}$ cm^{-3} for various thicknesses of GZO.

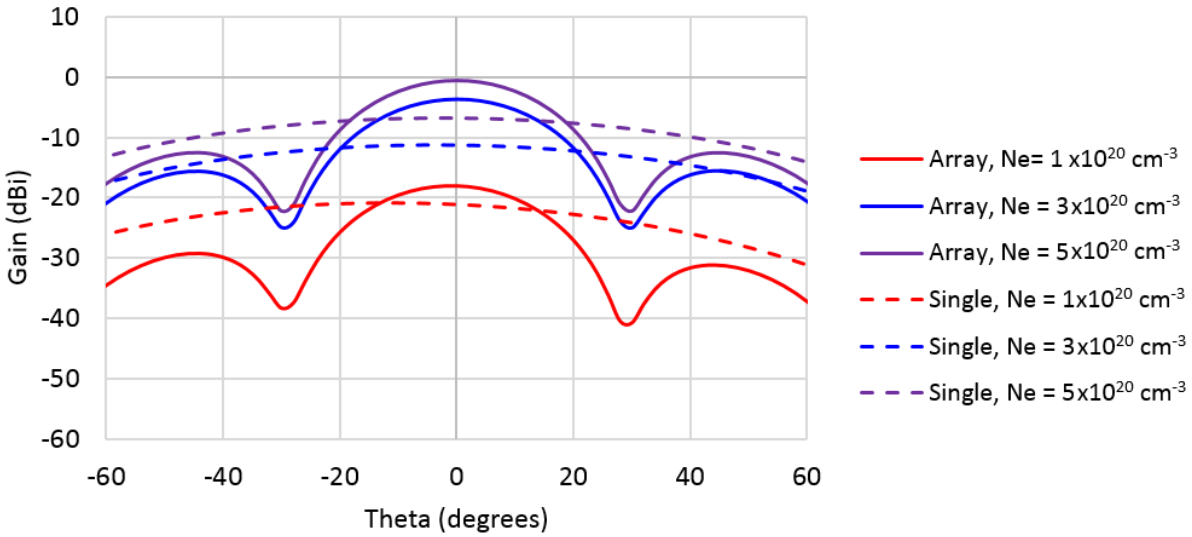

Figure 68 Simulated Gain versus Theta for array and element for film thickness of t = 1.5 μm for various carrier concentrations (N_e).

Next, a GZO antenna element was tested for gain to compare it with a 4x1 array. The GZO antenna was adhered to an acrylic slab and tested using the link budget analysis test setup seen in Figure 61 After this test, the antenna element was placed into the 4x1 array and the array was tested similarly to the tests performed for the copper array. The S_{21} between the input of the splitter and the output of the antenna were measured and the S_{21} phase of antenna number 4 is -138.6°. The S_{21} for each channel was measured and the phase for each channel was set by tuning the phase shifters to -138.6°. The simulated gain for both the antenna element and the array are shown in Figure 69. Both the simulation and the measured results show a strong correlation with the array results. The discrepancies in the gain with the single element are explained by 1) feeding mismatches with the silver epoxy paste used to adhere the coaxial connector the Au/Ti feed and 2) presence of Au/Ti feeds in the reactive nearfield of the GZO antenna. Despite these discrepancies, the antenna performance between the antenna elements and the antenna arrays correlate.

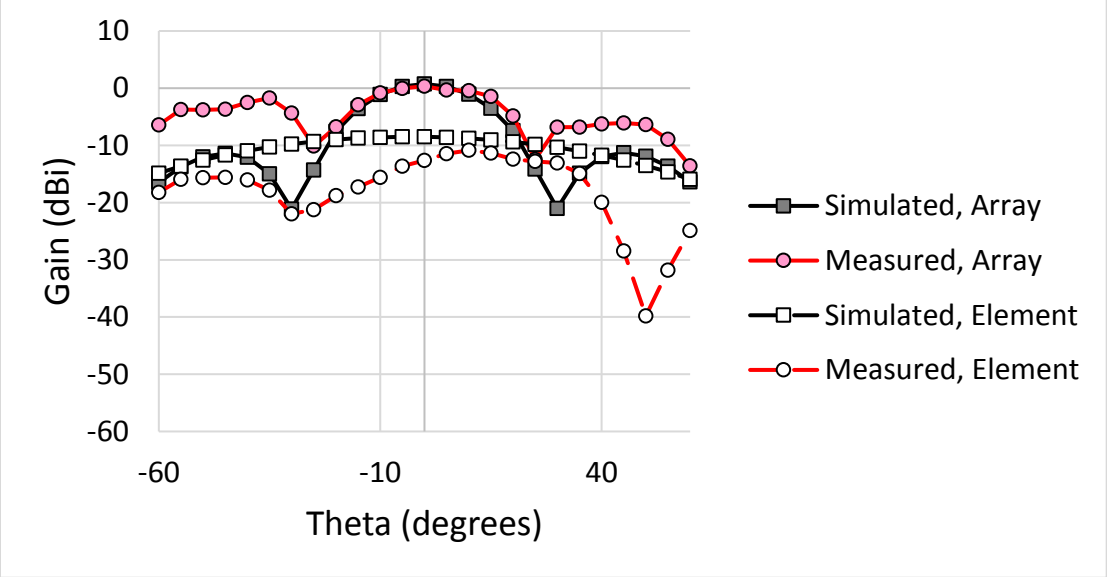

Figure 69 Simulated and measured results of boresight beam GZO antenna array and GZO antenna element.

Next, different $\Delta\phi$ were applied to have various beam angles. The array was simulated for its beam steering ability by applying the phase shifts shown in Table 8. The arrays were simulated for beam angles of -45°, -30°, -20°, -10°, +10°, +20°, +30°, and +45°. The assembled antenna

array is shown in Figure 70. The antenna elements were placed at a distance of a half wavelength (d = 26 mm) apart. The results of these simulated and measured beam angles are shown in Figure 71.

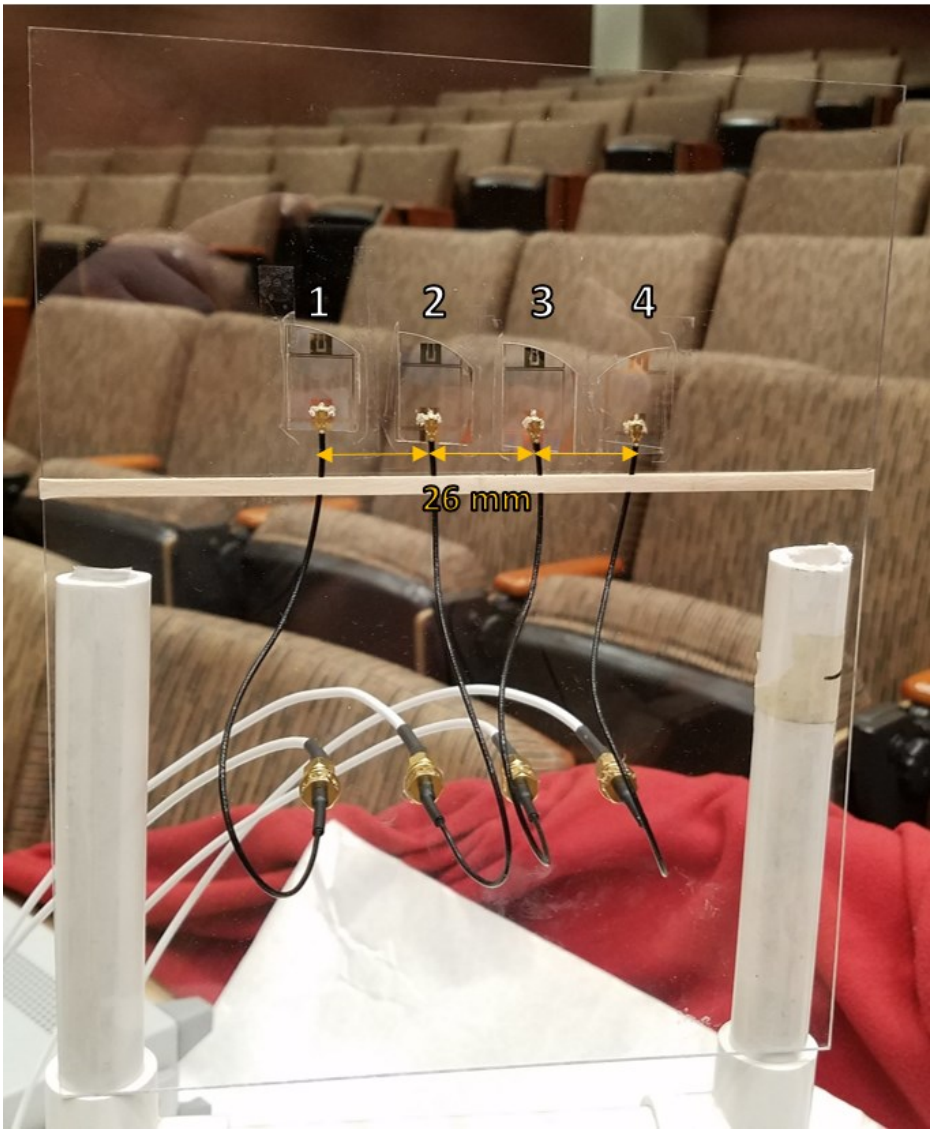

Figure 70 Assembled 4x1 GZO array on acrylic slab.

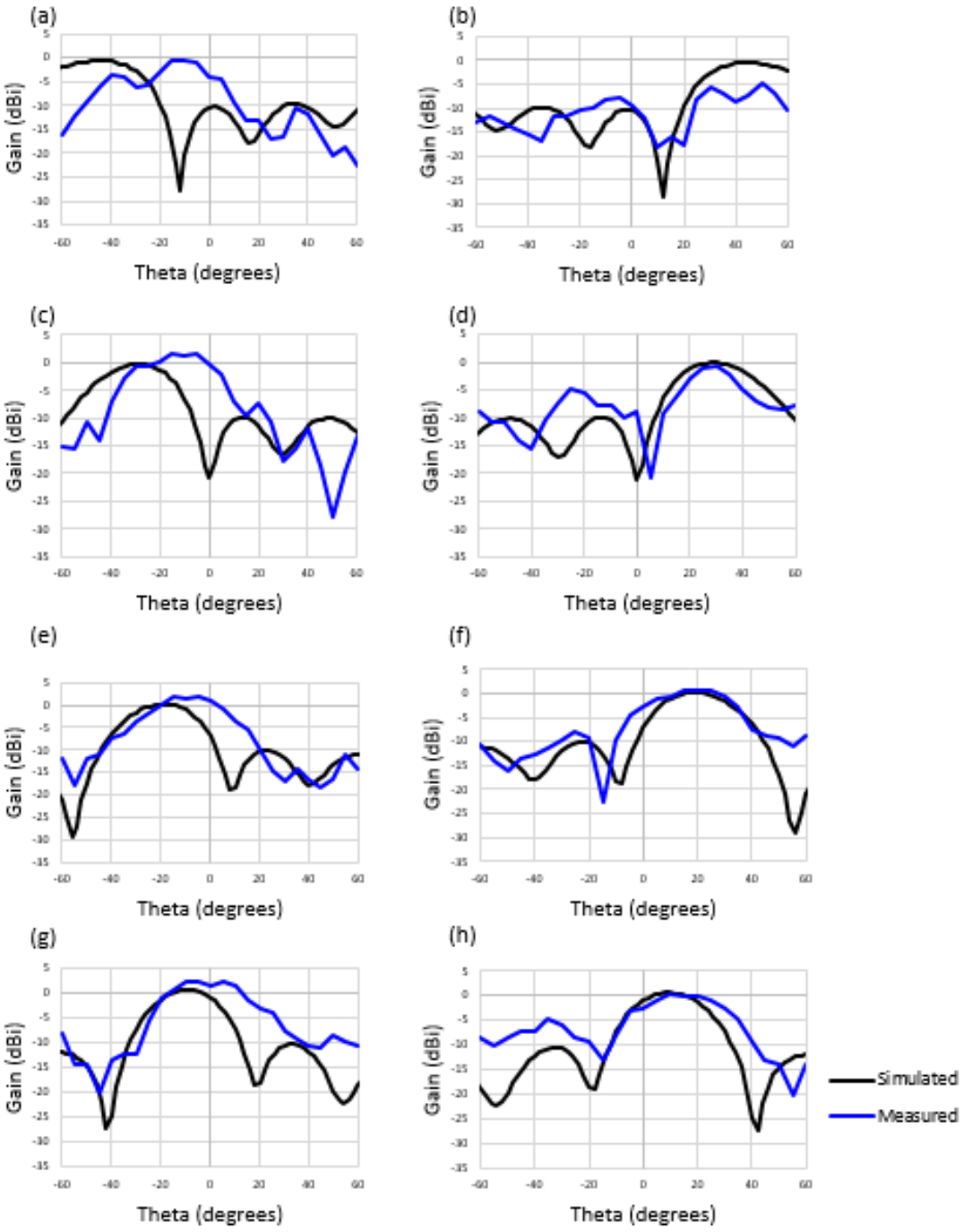

Figure 71 Simulated and measured GZO array beam steering for various beam angles. (a) -45° beam angle, (b) +45° beam angle, (c) -30° beam angle, (d) +30° beam angle, (e) -20° beam angle, (f) +20° beam angle (g) -10° beam angle (h) +10° beam angle.

The measured results correlate well with the simulated results for beam steering in the positive beam angle direction with the exception of +45°. The discrepancies are substantial for negative beam angles lower than -10°. These discrepancies are more than likely due to the

dissimilarity between each antenna due to their placement on the sapphire wafer and the cleaving plane. Because sapphire does not cleave as well as other substrates, the antennas fabricated on the substrates are at risk has a risk of damaging the antennas in the cleaving process, there are some inconsistencies in the fabricated elements. Despite the maximum beam angle not tracking well with the phase applied, the gain values at each beam angle (with the exception of -45°) shows very good correlation.

4.4 Discussion

In this chapter a brief background is given on periodic structures and testing periodic structures is presented. Furthermore, period structure performance is explored as TCO electrical properties are changed in simulation. In the case for FSSs, as the films become more conductive (as a function of the carrier concentration) and less resistive (as a function of film thickness), the resonance for the topology becomes more pronounced. If the thickness of the film or the carrier concentration is too low, in part to facilitate higher transparencies, the frequency selective surface loses the performance (either blockage or transmission) of the frequency of operation. For a Jerusalem cross design, the change in either film thickness or carrier concentration results in a frequency shift. In the case of antenna arrays, the changes inherent to antenna elements are applicable to antenna arrays. As the conductivity and thickness is changes, efficiency, gain, and resonance also change. The lower gain for transparent antennas can be countered via an antenna array. In this study, the gain increased approximately 12 dBi for boresight angle and approximately 11 dBi for angles up to ±30° from boresight for the manufactured antennas. One shortfall of the antenna array is the beam steering at negative angles from boresight. This may be due to

inconsistencies in film properties in Antenna 1 versus the remaining three. Antenna 1 has a higher sheet resistance compared to the other three antennas, meaning on beamforming at negative angles compared to boresight, this antenna is in the direction of the beam steering, resulting in a lower power output. In circumstances where there are elements operating at a lower efficiency than the other elements, an element replacement or an amplification is employed to balance the performance. In some circumstances, the elements are positioned to the outer part of the array. Material limitations did not leave this an option for replacement or amplification, leaving the inefficient antenna on the edge of the array. Despite this antenna array from not being able to beam steer to -30° from boresight and beyond, transparent antenna arrays do not show an inability to beam form with the presence of extra conduction losses.

Chapter 5: Conclusion and Future Work

5.1 Conclusions

In this dissertation, a brief overview and motivation driving development of optically transparent antennas is presented. In particular, optically transparent antennas can be applied to 5G and smart city applications through the embedding of these transparent antennas into windows and windshields offer aesthetically neutral access points. In particular, window embedded antennas in conjunction with the proper amplifier and routing mechanism can be employed as a signal repeater to mitigate communication dead zones within an urban environment. Methods to make a transparent antenna include meshing metal conductors and transparent conductive oxides (TCOs). In our paper, we focus on TCOs as promising materials for transparent antennas. Some of the most common TCOs used are indium tin oxide (ITO) and doped zinc oxides. TCO antennas present special challenges in design to achieve a reasonable trade-off between antenna efficiency and transparency. As the film thickness is increased, the transparency is decreased, and therefore the thickness must be minimized. However, the thinner the film, the more resistive the film and the less efficient the antenna. Additionally, the thin film antennas are more efficient at higher frequencies due to skin depth effects. As a result, thin film antennas are a natural selection for millimeter wave frequency bands. To demonstrate the potential of doped zinc oxide thin films as an electromagnetic device material, 2.4-GHz WiFi antennas, 5.8-GHz ISM band antennas, and

frequency selective surfaces (band-pass and stop-band filters) operating in the 23 GHz to 29 GHz frequency band were designed, fabricated, and tested. While promising, the reduced efficiency of the antennas poses a challenge researchers must overcome.

5.2 Limitations

While the array and the frequency selective surfaces fabricated in the study have shown acceptable performance for electromagnetic filtering and gain boosting, there are some limitations to the current designs that need to be improved. Exploring different designs, operational frequencies, and many other factors can result in not only arrays of higher gain and better efficiency, but of direct use to smart city and other applications.

The major drawback to the use of transparent antennas is the inefficiency. Even in use in an array, the inefficiency of the antennas cause such a low gain, that in order to match the gain of a copper counterpart, many antennas need to be used. Using equation (2.21), the number of elements needed to meet a specified array gain is given below in equation (5.1). In this equation, n is the number of elements in the array, G_A is the gain of the array in dBi, and G_E is the gain of the antenna element in dBi. According to equation (5.1), in order to have a 10 dBi increase in gain over the element gain, 10 elements are needed. For 20 dBi gain increase, 100 elements are needed. In order for the GZO array to match the gain of a single copper element, no fewer than 7 elements are necessary in the array,

$$n = 10^{(G_A - G_E)/10}. \tag{5.1}$$

Another challenge in the optimization of this antenna array is the scoring of sapphire to separate antennas. Due to the scoring plane of the sapphire wafer, not all antennas are fabricated

equally. In future iterations of this research, a complete antenna array on a full sapphire wafer (with no scoring) should be explored. This limitation of using a full sapphire wafer without scoring also assists in facilitating in higher frequency. For example, an array operating at 28 GHz yields a separation of 10.7 mm between each antenna element. On a 2 inch diameter sapphire wafer, approximately 60 elements can fit, yielding 17.8 dBi increase in gain between the antenna elements individually to the array configuration. Figure 72 shows a potential 28 GHz patch antenna array fed via coupling aperture. Additional elements also provide a narrower beam and a wider range of beam steering angles. Another way to mitigate the scoring issue of sapphire is to consider other substrates to deposit and etch GZO including silica glass and flexible substrates that can be cut with scissors or a rotary tool.

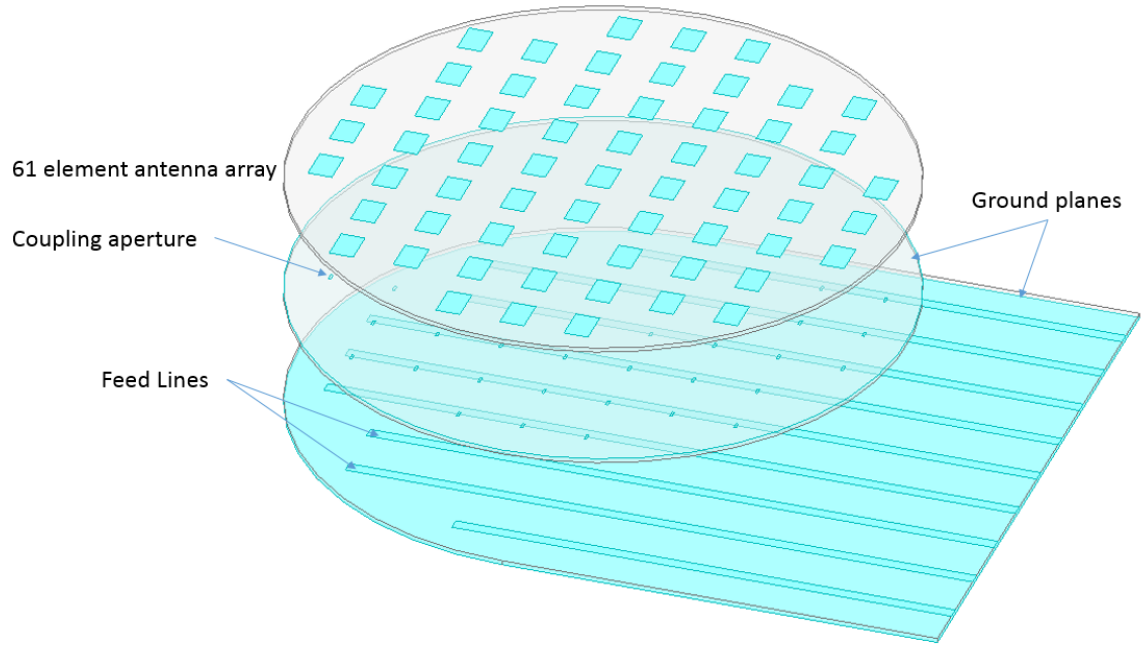

Figure 72 GZO Aperture fed antenna array (61 elements) on sapphire substrates.

Another large limitation, similar to the low gain, is the inefficiency of feeding techniques for optically transparent antennas. In this study, opaque coaxial cables are used to feed the antennas in order to minimize power loss to the antennas. In order to make an array where both antennas

and feeds are transparent, feeding methods (including striplines and microstrip lines) must also be highly transparent. This issue is also seen in meshed antennas as seen in Figure 16 [90]. In this study, Hautcoeur et al. produced a meshed transparent antenna array, but the corporate feeding had a transparency of approximately 30%. In order to minimize the losses in the mesh, the meshing size is reduced. Similarly, with TCOs, the film thickness and carrier concentrations will need to be increased.

5.3 Future Outlooks

Despite the limitations of using transparent antennas, the applications of transparent antennas and filters extend beyond the realm of smart city communication. These end applications for transparent antennas include industrial sectors such as space [104], military [104], and medical. Below, each of these sectors are discussed in the context of transparent antennas and filters. As a result, future research in optically transparent antennas needs to focus in alleviating the above stated limitations as well as these promising and influential fields.

5.3.1 Transparent and Flexible Antennas for Satellite and Space Communication

One of the original applications for transparent antennas, satellite communication, can further benefit from transparent antennas and arrays. Moreover, the use of transparent antennas on transparent, flexible, adhesive substrates to apply to solar cells [104]. The benefit of adhering transparent antenna arrays to solar panels of satellites is that the payload of satellites can be reduced while not removing either system from the satellite. Furthermore, the flexible version of antenna

arrays can be sent compact payloads via manned missions to provide repair materials for the antennas already implemented. The advantage here is that while current antennas used on space stations, satellites, and other space related capsules, these antennas typically are rigid and not compact while a flexible antenna can be stored in a smaller footprint than it needs for operation.

5.3.2 Military Automotive Communication

One of the major contributions of transparent antennas to the scope of the military is more secure methods of communication. A common issue for the military and department of defense contractors is the ability to reverse engineer critical systems from sight. In the context of radar and communications, the operational frequency can be determined if the space between the elements or the size of the elements are estimated. Figure 73 shows an example of sight sensitivity. In Figure 73 (a), a military automotive possesses several communications systems with redundancy antennas. These antennas seen on the Humvee is a quarter wavelength monopole topology. If the size of the antennas are seen, the frequency of operation can be estimated and a spoofing or jamming system can be put into place for sabotage of military operations. To help counter these issues, transparent antennas can be integrated into the windshields, windows, or in the body of the automobile to provide communication that the monopole antennas would offer. The transparency of the antennas would make the goal of enemy forces to thwart military operations harder to accomplish without complex technology to sniff for military communication frequencies.

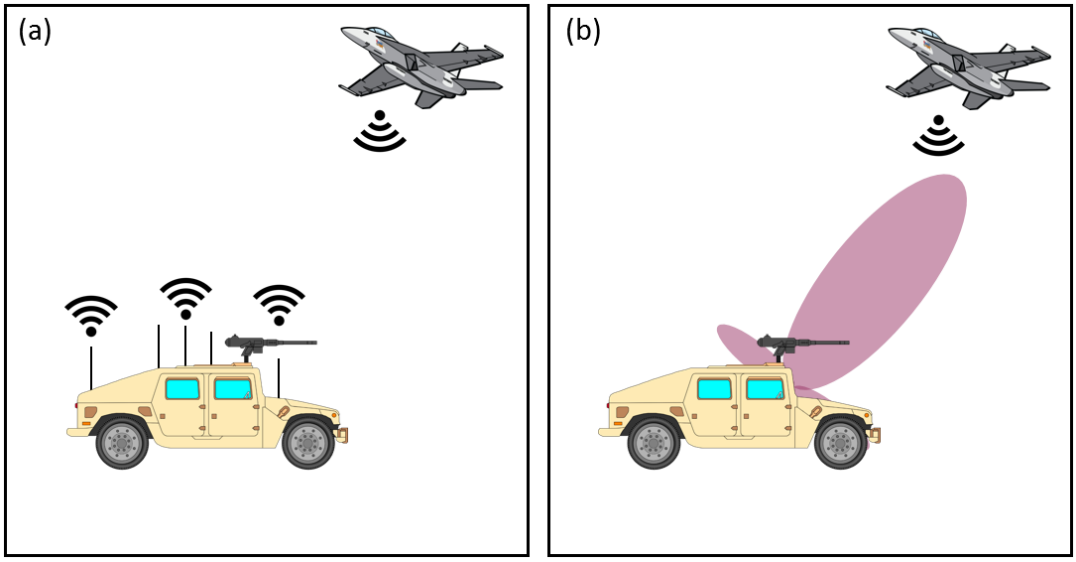

Figure 73 Military automotive communication system. (a) Automotive monopoles exposed for enemy forces to estimate communication bands for sabotage. (b) Automotive using windshield embedded antenna array for air to ground communication.

5.3.3 Medical Devices Using Optically Transparent Antennas

A natural place for transparent antennas is in conjunction with contact lens embedded medical sensors. Contact lenses have been proposed, and in some cases successfully, to monitor diabetes [105] [106], glaucoma [107], and intraocular pressure [108]. In particular, intraocular pressure has been measured via De Smedt et al. with a biosensor integrated with an antenna on the conctact lens to both collect power for the sensor and to broadcast data back to a portable recorder. The portable recorder also provides power wirelessly to the lens embedded sensor. The system developed can be seen in Figure 74. One limitation of this system is the visibility of the system. While an excellent tool for clinical usage, the device does not adapt well to an inconspicuous way to continuously monitor intraocular pressure due to the mask covering approximately a quarter of the face. Those who manage diseases that can be monitored using this system would most likely not utilize the system outside of the home or doctor's office as it calls attention to the device.

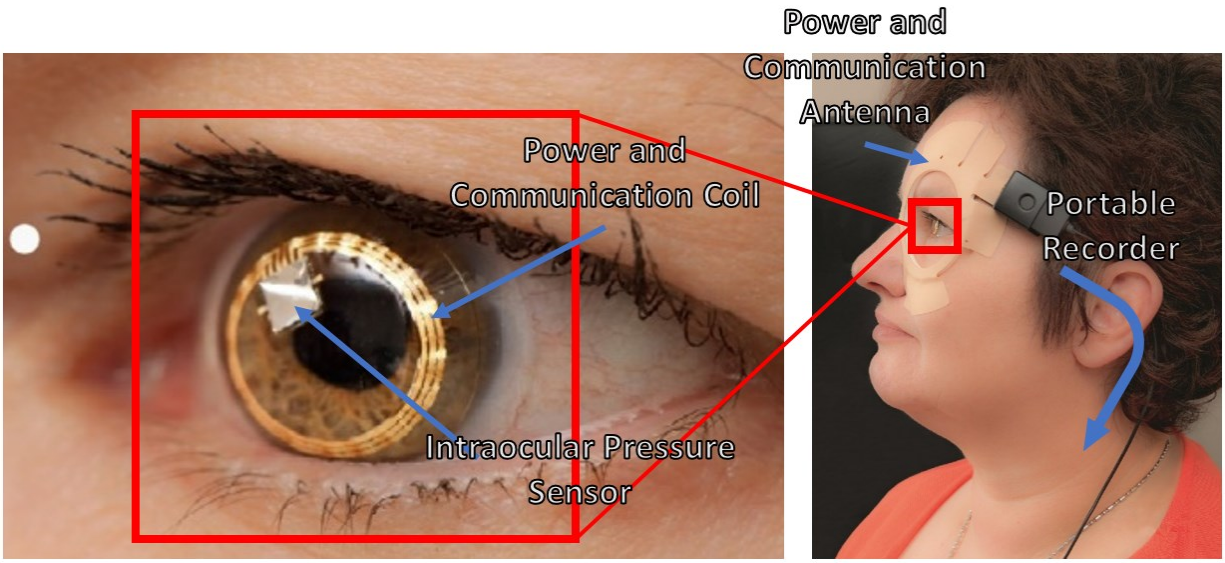

Figure 74 Wireless intraocular pressure sensor developed by Sensimed AG including contact lens with sensor and RF coil for power transfer and communication (left) and including a wearable recorder (right). [108]

An alternative would be to implement transparent loops and antennas into both the contact lens and a pair of eyeglasses to provide power and collect data (Figure 75). The benefit of using the eyeglasses is that different styles can appeal to different patients ranging various ages and lifestyle. The use of transparent antennas would allow for the functionality of these sensor systems for continuous monitoring while not sacrificing market value due to the conspicuous nature of optically opaque conductive materials.

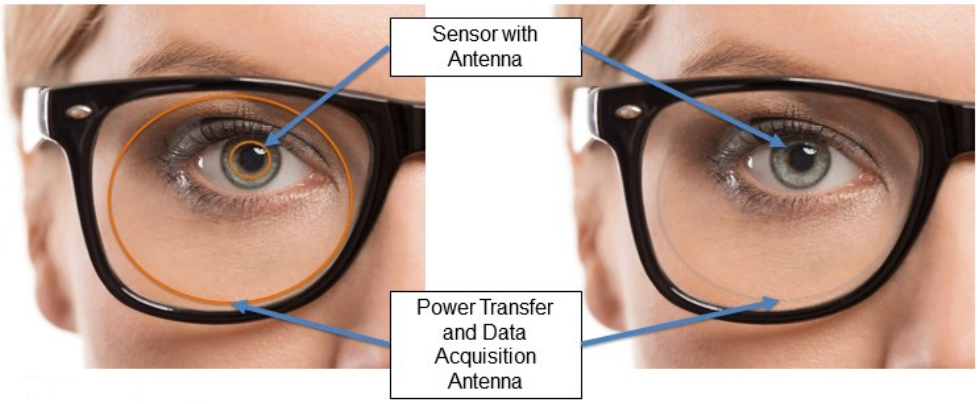

Figure 75 Optically transparent antennas for intraocular pressure sensor system. Opaque conductor system (left) and transparent conductor system (right).

5.4 Concluding Remarks

While research challenges exist, optically transparent antennas could allow the realization of smart cities, one of the goals of the 5G network [7] [8]. Applications range from windshield communication for self-driving cars, the internet of things (IOT), and higher data rates. Beyond the scope of smart cities, transparent antennas may potentially extend into military, commercial, and medical applications with antennas embedded into eyeglasses [109] and contact lenses for wearable intraocular pressure sensors [110] [111]. TCO antennas provides a viable option for upcoming wireless technologies such as proposed 5G, which will not only be ten times faster than current 4G LTE but will have 1000 times more communication capacity [7].

References

[1] R. Hall, "The vision of a smart city," Proceedings of the 2nd International Life Extension Technology Workshop, Paris, France, 2000.

[2] C. Harrison, B. Eckman, R. Hamilton, P. Hartswick, J. Kalagnanam, J. Paraszczak, P. Williams, "Foundations for Smarter Cities," IBM Journal of Research and Development, Vol 54, Is 4. 2010.

[3] F. Howarth, "Developing Smart City Initiatives with the IoT," Insights, Samsung, Dec. 2016 [Online] Available: https://insights.samsung.com/2016/12/28/developing-smart-city-initiatives-with-the-iot/ [Accessed: 13-Feb-19]

[4] T. Nam, T. Pardo, "Conceptualizing smart city with dimensions of technology people and institutions," Proceedings of the 12th Annual International Digital Government Research Conference: Digital Government Innovation in Challenging Times, College Park, MD, 2011, pp. 282 – 291

[5] "Traffic Signal Priority 101," Choose your Bellevue Blog, Oct. 2011. [Online] Available: http://blog.chooseyourwaybellevue.org/blog/2011/10/traffic-signal-priority-101/ [Accessed: 25-Feb-19]

[6] "Council Roundup: 'Smart City' Accomplishments," City News, City of Bellevue WA, [Online] Available: https://bellevuewa.gov/archived-news/city-council-archived-news/council-roundup-smart-city-accomplishments [Accessed: 25-Feb-19]

[7] "Everything You Need to Know About 5G - IEEE Spectrum." [Online]. Available: http://spectrum.ieee.org/video/telecom/wireless/everything-you-need-to-know-about-5g. [Accessed: 03-Aug-2017].

[8] Samsung Electronics, "5G Vision," 2015. [Online]. Available: http://www.samsung.com/global/business-images/insights/2015/Samsung-5G-Vision-0.pdf. [Accessed: 03-Aug-2017].

[9] Kaushik, "Camouflaged Cell Phone Towers," Amusing Planet, [Online] Available: https://www.amusingplanet.com/2010/01/camouflaged-cell-phone-towers.html [Accessed: 25-Feb-19]

[10] R. Blank, "Hiding Cell Phone Antennas in Plain Sight," Shield You Body LLC, Sep. 2014 [Online] Available: https://www.shieldyourbody.com/2014/09/cell-phone-antennas-hidden-in-plain-sight/ [Accessed: 25-Feb-19]

[11] TD. Brat, "Hotels in Ridgeland, Mississippi," Hotels.com [Online] Available: https://www.hotels.com/de1435057/hotels-ridgeland-mississippi/ [Accessed: 25-Feb-19]

[12] "mmWave channel modeling with diffuse scattering in an office environment," Remcom, 2019 [Online] Available: https://www.remcom.com/examples/2017/6/22/mmwave-channel-modeling-with-diffuse-scattering-in-an-office-environment [Accessed: 13-Mar-19]

[13] C. Tsakonas et al., "Optically transparent frequency selective window for microwave applications," Electron. Lett., vol. 37, no. 24, p. 1464, 2001.

[14] Y. M. Liu, B. Liu, J. B. Tan, Y. Han, J. Ma, and P. Jin, "Optical-transparent Wi-Fi bandpass mesh-coated frequency selective surface," Electron. Lett., vol. 50, no. 5, pp. 381–383, Feb. 2014.

[15] H. J. Song, J. H. Schaffner, K. A. Son and J. S. Moon, "Optically transparent Ku-band silver nanowire frequency selective surface on glass substrate," 2014 IEEE Antennas and Propagation Society International Symposium (APSURSI), Memphis, TN, 2014, pp. 2100-2101.

[16] A. A. Dewani, S. G. O'Keefe, D. V. Thiel, and A. Galehdar, "Optically transparent frequency selective surfaces on flexible thin plastic substrates," AIP Adv., vol. 5, no. 2, p. 27107, Feb. 2015.

[17] G. Clasen and R. J. Langley, "Meshed patch antenna integrated into car windscreen," Electron. Lett., vol. 36, no. 9, p. 781, 2000.

[18] T. Yasin, "Transparent antennas for solar cell integration," Ph.D. dissertation, Utah State Univ., Logan, 2013

[19] E. Mabrouk, "What are smallsats and cubesats?," Science Instruments, NASA, Feb. 2015. Available: https://www.nasa.gov/content/what-are-smallsats-and-cubesats

[20] T. Yasin, R. Baktur and C. Furse, "A comparative study on two types of transparent patch antennas," 2011 XXXth URSI General Assembly and Scientific Symposium, Istanbul, 2011, pp. 1-4.

[21] O. Yurduseven, D. Smith, N. Pearsall and I. Forbes, "A transparent solar patch antenna for 2.4/2.5 GHz WLAN-WiMAX applications," 2012 2nd International Symposium On Environment Friendly Energies And Applications, Newcastle upon Tyne, 2012, pp. 614-617.

[22] G. Clasen and R. Langley, "Meshed patch antennas," IEEE Trans. Antennas Propag., vol. 52, no. 6, pp. 1412–1416, Jun. 2004.

[23] Q. H. Dao, T. J. Cherogony and B. Geck, "Optically transparent and circularly polarized patch antenna for K-band applications," 2016 German Microwave Conference (GeMiC), Bochum, 2016, pp. 247-250.
[24] J. A. Arellano, “Inkjet-printed highly transparent solar cell antennas,” M.S. Thesis, Dept. Electrical and Computer Eng., Utah State University, Logan, UT, 2011.
[25] T. Yasin, “Optically transparent multifunctional patch antennas integrated with solar cells for small satellites.” Small Satellite Conference, Logan Utah, 2011.
[26] G. Clasen and R. J. Langley, “Gridded circular patch antennas,” Microwave and Optical Technology Letters, vol. 21, no. 5, pp. 311–313, Jun. 1999.
[27] G. Kontopidis, N. J. Kirsch, B. Turner, and E. R. Escobar, “5.5 GHz optically transparent mesh wire microstrip patch antenna,” Electron. Lett., vol. 51, no. 16, pp. 1220–1222, Aug. 2015.
[28] Q. H. Dao, R. Braun and B. Geck, "Design and investigation of meshed patch antennas for applications at 24 GHz," 2015 European Radar Conference (EuRAD), Paris, 2015, pp. 477-480.
[29] G. Andrasic and J. R. James, "Microstrip window array," in Electronics Letters, vol. 24, no. 2, pp. 96-97, 21 Jan. 1988.
[30] S. Hong, Y. Kim and C. Won Jung, "Transparent Microstrip Patch Antennas With Multilayer and Metal-Mesh Films," in IEEE Antennas and Wireless Propagation Letters, vol. 16, pp. 772-775, 2017.
[31] J. Hautcoeur, F. Colombel, X. Castel, M. Himdi and E. M. Cruz, "Optically transparent monopole antenna with high radiation efficiency manufactured with silver grid layer (AgGL)," in Electronics Letters, vol. 45, no. 20, pp. 1014-1016, September 24 2009.
[32] M. Kashanianfard and K. Sarabandi, "Vehicular Optically Transparent UHF Antenna for Terrestrial Communication," in IEEE Transactions on Antennas and Propagation, vol. 65, no. 8, pp. 3942-3949, Aug. 2017.
[33] O. Yurduseven, D. Smith and M. Elsdon, "A transparent meshed solar monopole antenna for UWB applications," The 8th European Conference on Antennas and Propagation (EuCAP 2014), The Hague, 2014, pp. 2145-2149.
[34] A. Martin, X. Castel, O. Lafond and M. Himdi, "Optically transparent frequency-agile antenna for X-band applications," in Electronics Letters, vol. 51, no. 16, pp. 1231-1233, 8 6 2015.
[35] N. Guan, H. Furuya, R. Hosono, H. Tayama and K. Yamagami, "A see-through wire-grid film antenna for WLAN applications," 2012 IEEE Asia-Pacific Conference on Antennas and Propagation, Singapore, 2012, pp. 273-274.
[36] M. M. Rabie, H. El-Henawy, F. El-Hefnawy and F. Ibrahim, "Meshed conductor and meshed substrate GPS L1 band microstrip antenna for Cubesat applications," *2018 35th National Radio Science Conference (NRSC)*, Cairo, 2018, pp. 55-62.
[37] S. H. Kang and C. W. Jung, "Transparent Patch Antenna Using Metal Mesh," in *IEEE Transactions on Antennas and Propagation*, vol. 66, no. 4, pp. 2095-2100, April 2018.
[38] Q. L. Li, S. W. Cheung, D. Wu and T. I. Yuk, "Optically Transparent Dual-Band MIMO Antenna Using Micro-Metal Mesh Conductive Film for WLAN System," in *IEEE Antennas and Wireless Propagation Letters*, vol. 16, pp. 920-923, 2017.
[39] T. Yasin and R. Baktur, "Bandwidth Enhancement of Meshed Patch Antennas Through Proximity Coupling," in IEEE Antennas and Wireless Propagation Letters, vol. 16, pp. 2501-2504, 2017.
[40] T. Yasin, R. Baktur, T. Turpin, and J. Arellano, “Analysis and design of highly transparent meshed patch antenna backed by a solid ground plane,” Progress in Electromagnetics Research M., vol. 56, pp. 133–144, 2017.
[41] H. J. Song, T. Y. Hsu, D. F. Sievenpiper, H. P. Hsu, J. Schaffner and E. Yasan, "A Method for Improving the Efficiency of Transparent Film Antennas," in IEEE Antennas and Wireless Propagation Letters, vol. 7, pp. 753-756, 2008.
[42] M. J. Roo-Ons, S. V. Shynu, M. J. Ammann, S. J. McCormack and B. Norton, "Transparent patch antenna on a-Si thin-film glass solar module," in Electronics Letters, vol. 47, no. 2, pp. 85-86, January 2011.
[43] Q. L. Li, S. W. Cheung, D. Wu and T. I. Yuk, "Optically Transparent Dual-Band MIMO Antenna Using Micro-Metal Mesh Conductive Film for WLAN System," in IEEE Antennas and Wireless Propagation Letters, vol. 16, pp. 920-923, 2017.
[44] T. Peter, R. Nilavalan, H. F. AbuTarboush and S. W. Cheung, "A Novel Technique and Soldering Method to Improve Performance of Transparent Polymer Antennas," in IEEE Antennas and Wireless Propagation Letters, vol. 9, pp. 918-921, 2010.
[45] T. Peter, T. I. Yuk, R. Nilavalan, and S. W. Cheung, “A novel technique to improve gain in transparent UWB antennas,” in 2011 Loughborough Antennas & Propagation Conference, 2011, pp. 1–4.

[46] A. Katsounaros, Y. Hao, N. Collings, and W. A. Crossland, “Optically transparent antenna for ultra wide-band applications,” in 2009 3rd European Conference on Antennas and Propagation, 2009, pp. 1918–1921.
[47] H. Liu, V. Avrutin, N. Izyumskaya, Ü. Özgür, and H. Morkoç, “Transparent conducting oxides for electrode applications in light emitting and absorbing devices,” Superlattices and Microstructures, vol. 48, no. 5, pp. 458–484, Nov. 2010.
[48] I. Kapilevich and A. Skumanich, "Indium shortage implications for the PV and LCD market: Technology and market considerations for maintaining growth," 2009 34th IEEE Photovoltaic Specialists Conference (PVSC), Philadelphia, PA, 2009, pp. 002055-002060.
[49] E. A. Alwan, A. Kiourti and J. L. Volakis, "Indium Tin Oxide Film Characterization at 0.1–20 GHz Using Coaxial Probe Method," in IEEE Access, vol. 3, pp. 648-652, 2015.
[50] P. Prajuabwan, S. Porntheeraphat, A. Klamchuen, and J. Nukeaw, “ITO thin films prepared by gas-timing RF magnetron sputtering for transparent flexible antenna,” in 2007 2nd IEEE International Conference on Nano/Micro Engineered and Molecular Systems, 2007, pp. 647–650.
[51] M. Bourry, M. Sarret, and M. Drissi, “Novel ITO alloy for microwave and optical applications,” in 48th Midwest Symposium on Circuits and Systems, 2005., 2005, p. 615–618 Vol. 1.
[52] N. Guan, H. Furuya, D. Delaune, and K. Ito, “Antennas made of transparent conductive films,” in Proc. PIERS, China, Mar. 2008, p. 720.
[53] N. He, Y. Yao, J. Yu, and X. Chen, “Design of novel optically transparent antenna for RFID applications,” in Microwave Theory and Techniques Society Asia-Pacific Microwave Conference, 26, Sendai, Japan, 2014, pp. 4–7.
[54] N. Outaleb, J. Pinel, M. Drissi, and O. Bonnaud, “Microwave planar antenna with RF-sputtered indium tin oxide films,” Microwave and Optical Technology Letters, vol. 24, no. 1, pp. 3–7, Jan. 2000.
[55] Y. Yao, N. He, W. Chen, J. Yu and X. Chen, "Novel optically transparent antenna for RFID smart fitting room application," 2015 Asia-Pacific Microwave Conference (APMC), Nanjing, 2015, pp. 1-3.
[56] N. Guan, Hirotaka Furuya, D. Delaune, and Koichi Ito, “Radiation efficiency of monopole antenna made of a transparent conductive film,” in 2007 IEEE Antennas and Propagation International Symposium, 2007, pp. 221–224.
[57] C.-T. Lee, C.-M. Lee, and C.-H. Luo, “The transparent monopole antenna for WCDMA and WLAN,” in 2006 IEEE Annual Wireless and Microwave Technology Conference, 2006, pp. 1–3.
[58] F. Colombel, X. Castel, M. Himdi, G. Legeay, S. Vigneron and E. M. Cruz, "Ultrathin metal layer, ITO film and ITO/Cu/ITO multilayer towards transparent antenna," in IET Science, Measurement & Technology, vol. 3, no. 3, pp. 229-234, May 2009.
[59] M. A. H. Khan, S. Ali, J. Bae, and C. H. Lee, “Inkjet printed transparent and bendable patch antenna based on polydimethylsiloxane and indium tin oxide nanoparticles,” Microwave and Optical Technology Letters, vol. 58, no. 12, pp. 2884–2887, Dec. 2016.
[60] A. Suzuki, T. Matsushita, T. Aoki, A. Mori, and M. Okuda, “Highly conducting transparent indium tin oxide films prepared by pulsed laser deposition,” Thin Solid Films, vol. 411, no. 1, pp. 23–27, 2002.
[61] O. Tuna, Y. Selamet, G. Aygun, and L. Ozyuzer, “High quality ITO thin films grown by dc and RF sputtering without oxygen,” Journal of Physics D: Applied Physics, vol. 43, no. 5, p. 55402, Feb. 2010.
[62] “USGS Minerals Information: Indium.” [Online]. Available: https://minerals.usgs.gov/minerals/pubs/commodity/indium/index.html. [Accessed: 15-Aug-2017].
[63] H. Agura, A. Suzuki, T. Matsushita, T. Aoki, and M. Okuda, “Low resistivity transparent conducting Al-doped ZnO films prepared by pulsed laser deposition,” Thin Solid Films, vol. 445, no. 2, pp. 263–267, Dec. 2003.
[64] B.-Z. Dong, H. Hu, G.-J. Fang, X.-Z. Zhao, D.-Y. Zheng, and Y.-P. Sun, “Comprehensive investigation of structural, electrical, and optical properties for ZnO:Al films deposited at different substrate temperature and oxygen ambient,” Journal of Applied Physics, vol. 103, no. 7, p. 73711, Apr. 2008.
[65] S.-M. Park, T. Ikegami, and K. Ebihara, “Effects of substrate temperature on the properties of Ga-doped ZnO by pulsed laser deposition,” Thin Solid Films, vol. 513, no. 1–2, pp. 90–94, Aug. 2006.
[66] H. Y. Liu, V. Avrutin, N. Izyumskaya, M. A. Reshchikov, Ü. Özgür, and H. Morkoç, “Highly conductive and optically transparent GZO films grown under metal-rich conditions by plasma assisted MBE,” Physica status solidi - Rapid Research Letters, vol. 4, no. 3–4, pp. 70–72, Apr. 2010.
[67] A. Tiburcio-Silver, A. Sanchez-Juarez, and A. Avila-Garcia, “Properties of gallium-doped ZnO deposited onto glass by spray pyrolysis,” Solar Energy Materials and Solar Cells, vol. 55, no. 1–2, 1998, pp. 3–10.

[68] T. Chen, C.-C. Chiang, and T.-Y. Chen, “The characteristic of GZO thin film deposited on flexible substrates by using RF magnetron sputtering,” in 2014 21st International Workshop on Active-Matrix Flatpanel Displays and Devices (AM-FPD), 2014, pp. 199–202.
[69] S. Ray, “Optical and dielectric properties of ZnO nanostructures at terahertz frequencies,” M.S. Thesis, Graduate College, Oklahoma State University, Stillwater, OK, 2001.
[70] Y. Liu and J. Lian, “Optical and electrical properties of aluminum-doped ZnO thin films grown by pulsed laser deposition,” Applied Surface Science, vol. 253, no. 7, 2007, pp. 3727–3730.
[71] J. Kim et al., “Optical properties of gallium-doped zinc oxide—a low-loss plasmonic material: first-principles theory and experiment,” Physical Review X, vol. 3, no. 4, 2013, p. 41037.
[72] J. R. Saberin and C. Furse, "Challenges with Optically Transparent Patch Antennas," in *IEEE Antennas and Propagation Magazine*, vol. 54, no. 3, pp. 10-16, June 2012.
[73] N.R. Aghamalyan, E.A. Kafadaryan, R. K. Hovsepyan, “Absorption and reflection analysis of transparent conductive Ga-doped ZnO films,” Semiconductor Science and Technology, vol. 20, no. 1, pp 80-85, Dec. 2004.
[74] M. E. Zamudio, M. Behzadirad, C. Christodoulou, and T. Busani, “Optimization of AZO films for integrating optically transparent antennas with photovoltaics,” Applied Physics Letters, vol. 110, no. 23, 2017, p. 234101.
[75] R. B. Green et al., “An alternative material for transparent antennas for commercial and medical applications,” Microwave Optical Technology Letters, vol. 59, no. 4, 2017, pp. 773–777.
[76] N. M. Jizat, S. K. A. Rahim, Y. C. Lo, and M. M. Mansor, “Compact size of CPW dual-band meander-line transparent antenna for WLAN applications,” in 2014 IEEE Asia-Pacific Conference on Applied Electromagnetics (APACE), 2014, pp. 20–22.
[77] C. Mias et al., "Optically transparent microstrip antennas," IEE Colloquium on Antennas for Automotives (Ref. No. 2000/002), London, 2000, pp. 8/1-8/6.
[78] G. Sun, B. Muneer, and Q. Zhu, “A study of microstrip antenna made of transparent ITO films,” in 2014 IEEE Antennas and Propagation Society International Symposium (APSURSI), 2014, pp. 1867–1868.
[79] B. M. Levin, “Transparent antennas,” Journal of Communications Technology and Electronics, vol. 57, no. 4, 2012, pp. 388–392.
[80] S. Hong, Y. Kim, C. Lee, and C. W. Jung, “A flexible and transparent antenna on a polyimide substrate for laptop computers,” in 2015 IEEE International Symposium on Antennas and Propagation & USNC/URSI National Radio Science Meeting, 2015, pp. 930–931.
[81] N. J. Kirsch, N. A. Vacirca, E. E. Plowman, T. P. Kurzweg, A. K. Fontecchio, and K. R. Dandekar, “Optically transparent conductive polymer RFID meandering dipole antenna,” in 2009 IEEE International Conference on RFID, 2009, pp. 278–282.
[82] R. G. Gordon, “Criteria for choosing transparent conductors,” MRS Bull., vol. 25, no. 8, pp. 52–57, Aug. 2000.
[83] J. R. Saberin and C. Furse, “Challenges with optically transparent patch antennas for small satellites,” in 2010 IEEE Antennas and Propagation Society International Symposium, 2010, pp. 1–4.
[84] P. P. Edwards et al., “Basic materials physics of transparent conducting oxides,” Dalton Transactions, vol. 90, no. 19, 2004, p. 2995.
[85] J. R. Saberin, “Optically transparent antennas for small satellites,” Dept. of Electrical and Computer Engineering, University of Utah, Salt Lake City, UT, 2010.
[86] L. Li, B. Zhang, B. Zou, R. Xie, T. Zhang, S. Li, B. Zheng, J. Wu, J. Weng, W. Zhang, W. Huang, F. Huo, "Fabrication of Flexible Transparent Electrode with Enhanced Conductivity from Hierarchical Metal Grids", *ACS Applied Materials & Interfaces*, vol. 9, no. 45, pp. 39110-39115, 2017.
[87] F.T. Ulaby, E. Michielssen, U. Ravaioli, *Fundamentals of Applied Electromagnetics*, 6th ed., USA, Prentice Hall, 2010.
[88] D.M. Pozar, *Microwave Engineering*, 3rd ed. Massachusetts: John Wiley and Sons, Inc., 2005.
[89] P. Hannan, "The element-gain paradox for a phased-array antenna," in IEEE Transactions on Antennas and Propagation, vol. 12, no. 4, pp. 423-433, July 1964.
[90] J. Hautcoeur, L. Talbi, K. Hettak and M. Nedil, "60 GHz optically transparent microstrip antenna made of meshed AuGL material," in IET Microwaves, Antennas & Propagation, vol. 8, no. 13, pp. 1091-1096, 21 October 2014.
[91] J. Donohoe, “Antenna Patterns’” [Online] Available: http://my.ece.msstate.edu/faculty/donohoe/6313_ch2_notes.pdf [Accessed: 14-Feb-19]

[92] P. S. Nakar, “Design of a compact microstrip patch antenna for use in wireless/cellular devices,” M.S. thesis, Dept. Elect. Comp. Eng. Florida State Univ., Tallahassee, FL, 2004.
[94] J.L. Volakis, *Antenna Engineering Handbook*, 4th ed., New York City, New York, McGraw-Hill, 2007.
[95] D. Sarkar, K. V. Srivastava and K. Saurav, "A Compact Microstrip-Fed Triple Band-Notched UWB Monopole Antenna," in IEEE Antennas and Wireless Propagation Letters, vol. 13, pp. 396-399, 2014.
[96] M. Chandak, *Design and Characterization of Circularly Polarized Cavity-Backed Slot Antennas in An In-House-Constructed Anechoic Chamber*, Logan, Utah, Utah State University, 2012
[97] C. Balanis, *Antenna Theory: Analysis and Design*, Hobroken, New Jersey, John-Wiley and Sons, Inc., 2005.
[97] R. Haupt, *Antenna Arrays: A Computational Approach*. Englewood Cliffs, New Jersey: Wiley, 2010.
[98] Munk B., “Frequency Selective Surfaces: Theory and Design”, Wiley-Interscience, ed. 1 (April 26, 2000)
[99] H. Rajagopalan, Y. Rahmat-Samii, and W. A. Imbriale, “Rf mems actuated reconfigurable reflectarray patch-slot element,” IEEE Transactions on Antennas and Propagation, vol. 56, pp. 3689–3699, December 2008.
[100] L. Liu, C. Yang, Q. Cao, H. Li and Y. Wang, "Smart-skins for radome using active frequency selective surface," *2016 IEEE International Workshop on Electromagnetics: Applications and Student Innovation Competition (iWEM)*, Nanjing, 2016, pp. 1-3.
[101] Remski R.; Gray B.; Ma L.; “Frequency Selective Surfaces,” Design and Analysis using the Ansoft Product Suite. http://citeseerx.ist.psu.edu/viewdoc/download?doi=10.1.1.225.7453&rep=rep1&type=pdf
[102] Rumpf R.C, “Frequency Selective Surfaces and Metasurfaces”, Class Notes: http://emlab.utep.edu/ee5390em21/Lecture%2020%20--%20FSS%20and%20Metasurfaces.pdf
[103] Hosseinipanah M, Wu Q., “Equivalent Circuit Model for Designing of Jerusalem Cross-Based Artificial Magnetic Conductors” Radioengineering, Vol 18, No 4, Dec 2009 http://www.radioeng.cz/fulltexts/2009/09_04_544_550.pdf
[104] C. White, H. R. and Khaleel, "Flexible Optically Transparent Antennas", WIT Transactions on State-of-the-art in Science and Engineering, 82, 2014, p. 59.
[105] Otis B.P., Parviz B. “Introducing Our Smart Contact Lens Project”. Alphabet; Mountain View, CA, USA: 2014
[106] Senior M. “Novartis signs up for Google smart lens”. Nat. Biotechnol. 2014;32:856
[107] Farandos NM, Yetisen AK, Monteiro MJ, Lowe CR, Yun SH, “Contact lens sensor in ocular diagnostics, ”Advanced Healthcare Matereroa;s. Vol. 4, is. (6), pp 792-810 (2015)
[108] S. De Smedt, “Noninvasive intraocular pressure monitoring: current insights,” Clinical ophthalmology, vol. 9, pp. 1385-1392, March 2015
[109] Y. Kim, J. Maeng, P. Irazoqui, “Eyeglasses-powered, contact lens-like platform with high power transfer efficiency,” in *Biomedical Microdevices*, vol. 17, no. 75, 2015
[110] C. Varel, Y. Shih, B. Otis, T. Shen, K. Bohringer, “A wireless intraocular pressure monitoring device with a solder-filled microchannel antenna,” in *Journal of Micromechanics and Microengineering*, vol. 24, no. 4, 2014
[111] E. Chow, S. Sanghani, V. Ramesh, “Emerging research in wireless and MEMS for medical applications,” in *Wireless MEMS Networks and Applications*, D. Uttamchandani, Ed, Woodhead Publishing, 2017, pp. 153-175.

Appendix A: Return Loss Results for GZO Antennas

A.1 Planar Dipole

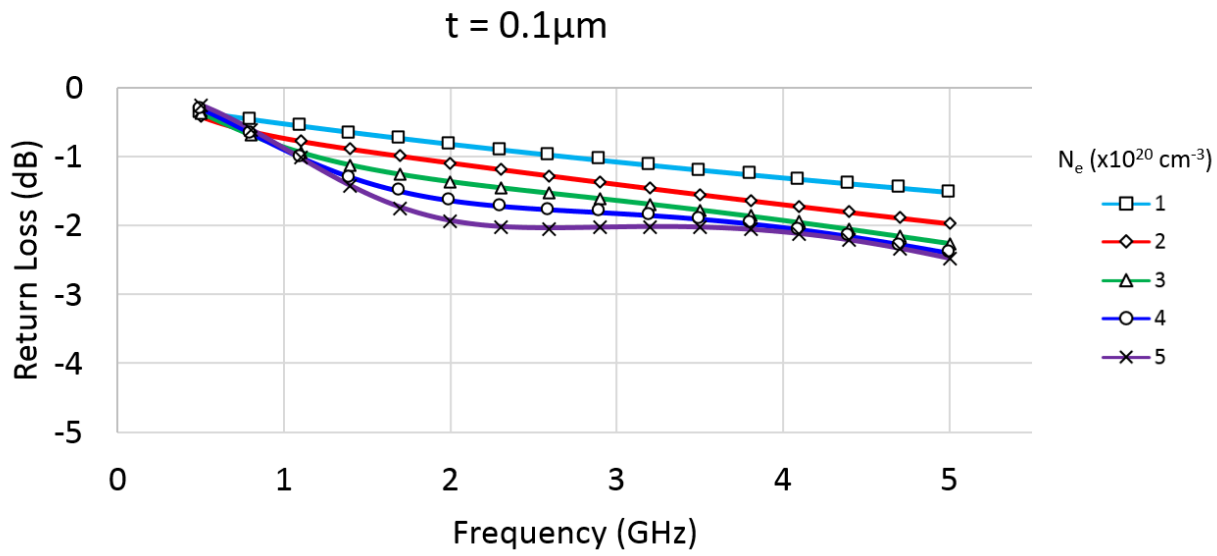

Figure A. 1 Return Loss of dipole antenna at t = 0.1µm

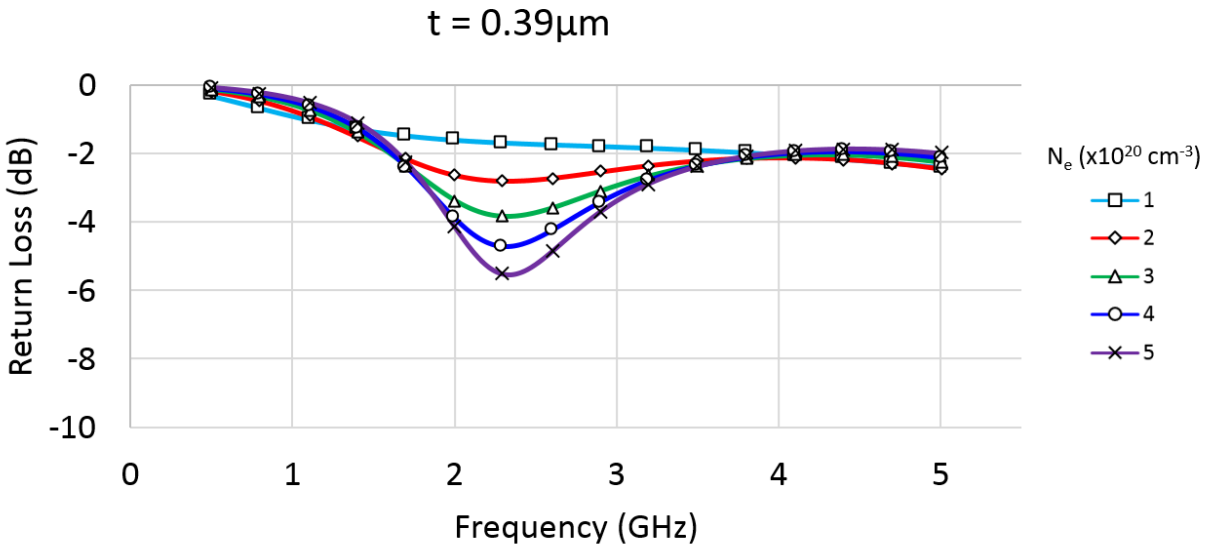

Figure A. 2 Return Loss of dipole antenna at t = 0.39µm

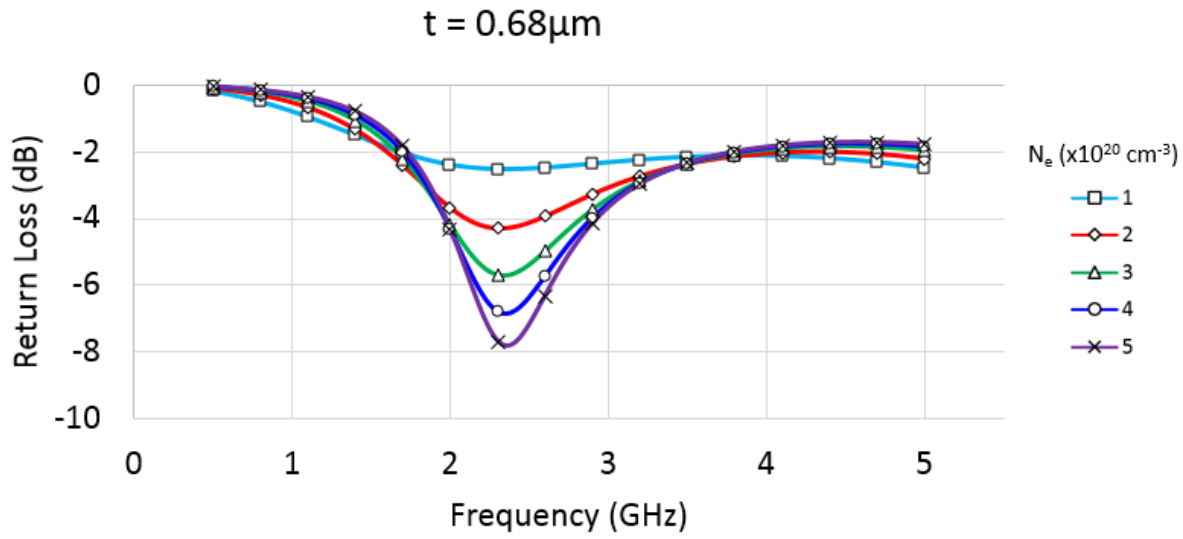

Figure A. 3 Return Loss of dipole antenna at t = 0.68µm

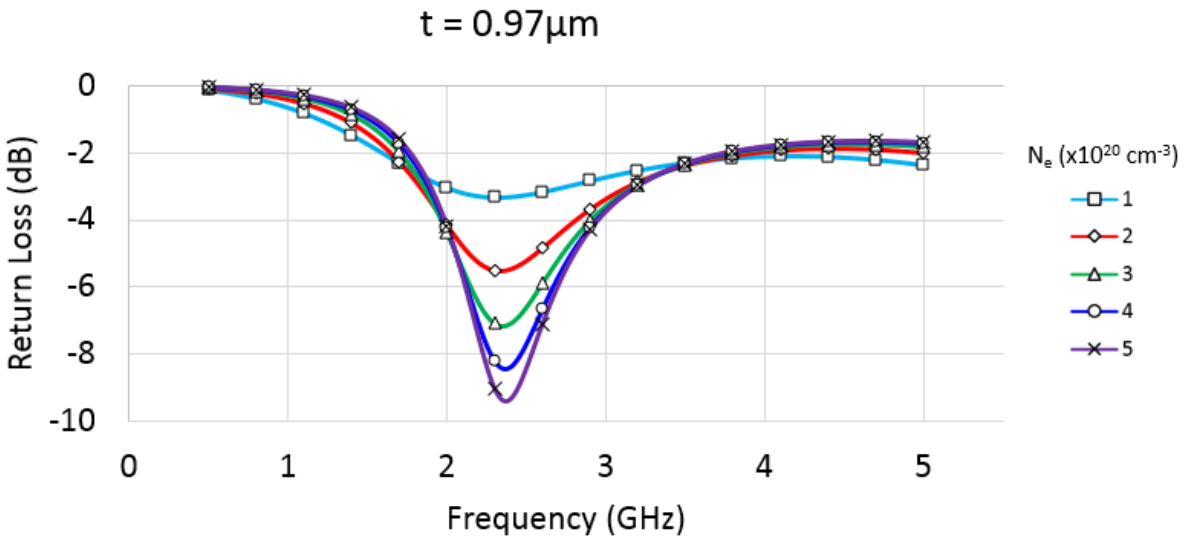

Figure A. 4 Return Loss of dipole antenna at t = 0.97µm

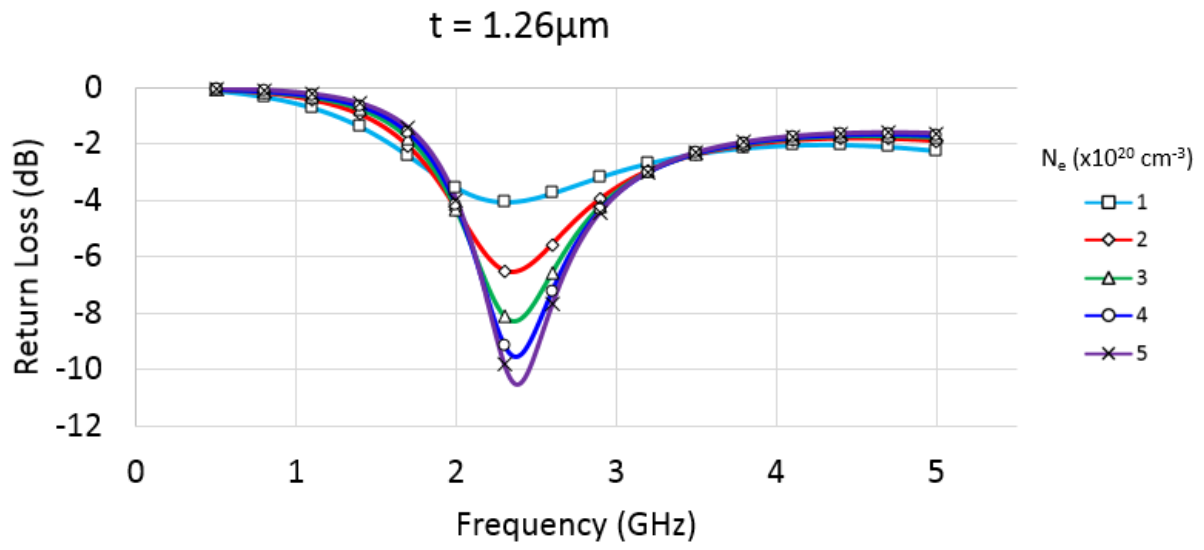

Figure A. 5 Return Loss of dipole antenna at t = 1.26µm

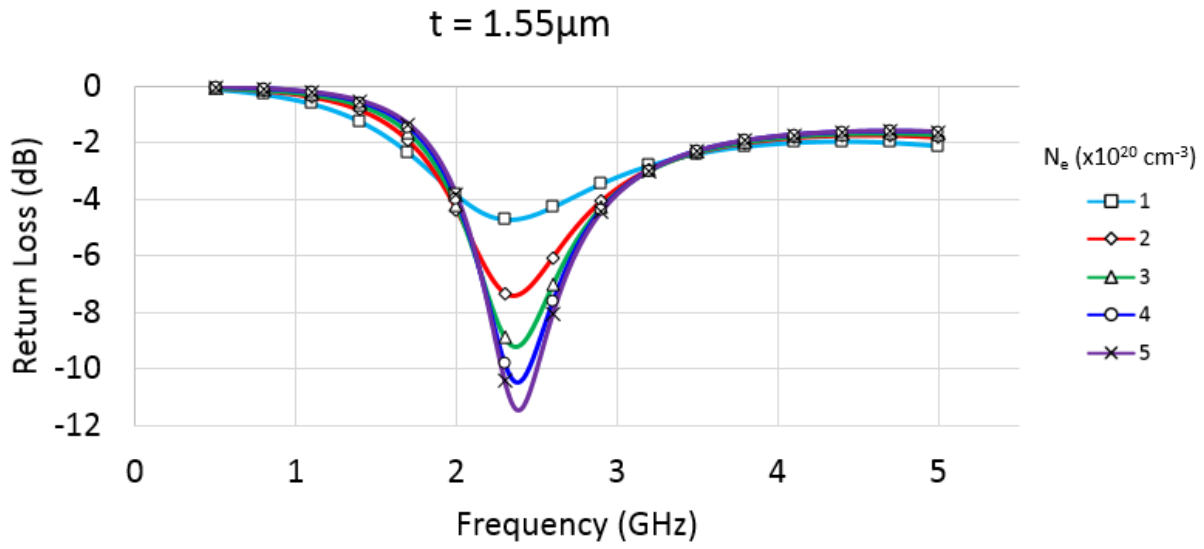

Figure A. 6 Return Loss of dipole antenna at t = 1.55µm

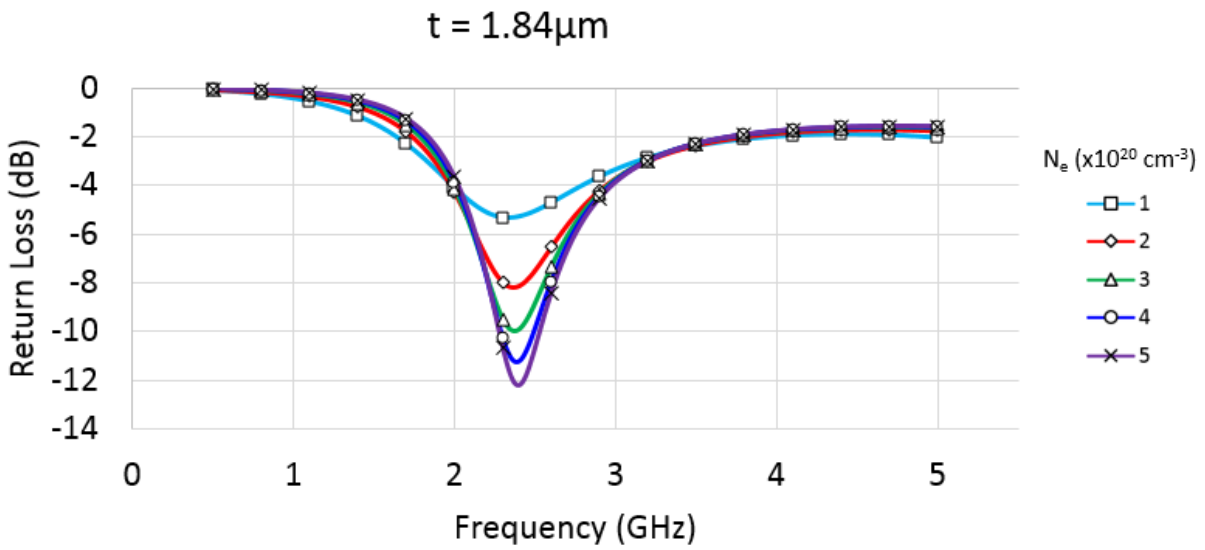

Figure A. 7 Return Loss of dipole antenna at t = 1.84µm

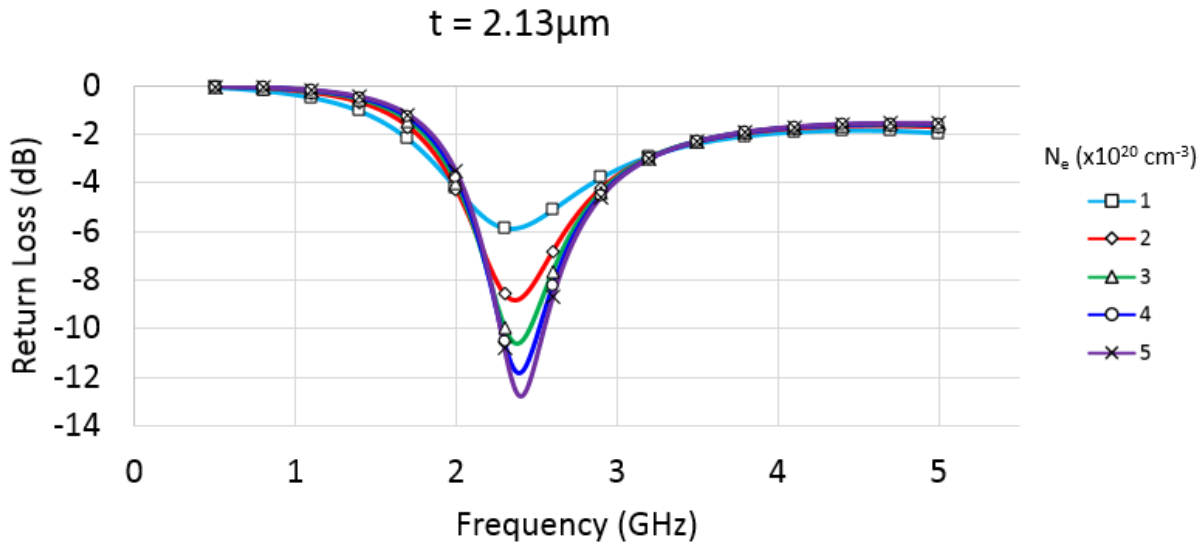

Figure A. 8 Return Loss of dipole antenna at t = 2.13µm

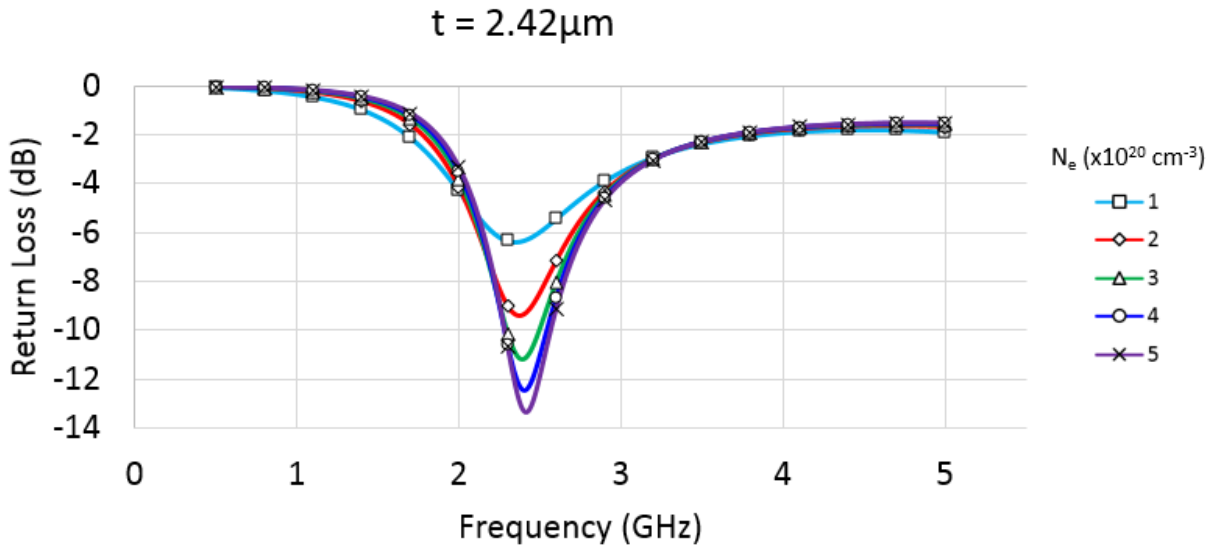

Figure A. 9 Return Loss of dipole antenna at t = 2.42µm

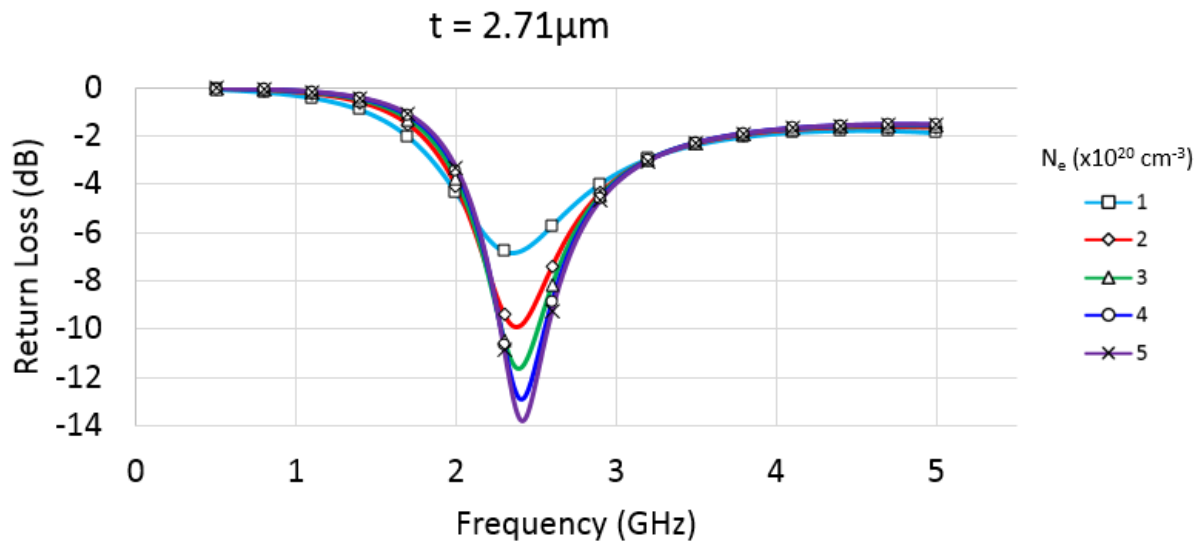

Figure A. 10 Return Loss of dipole antenna at t = 2.71µm

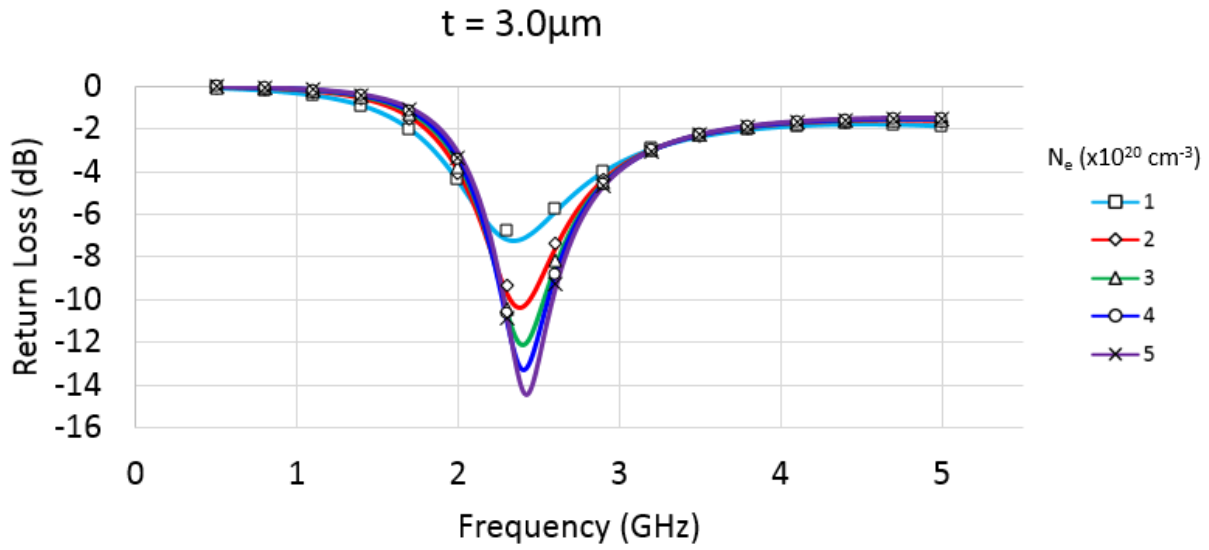

Figure A. 11 Return Loss of dipole antenna at t = 3.0µm

A.2 Planar Hourglass

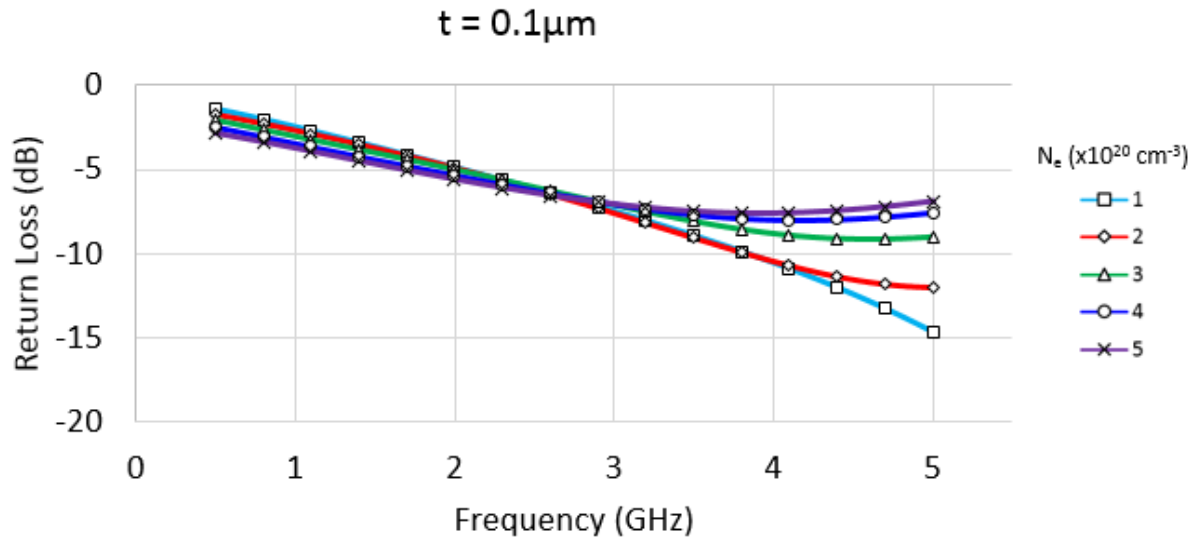

Figure A. 12 Return Loss of hourglass antenna at t = 0.1µm

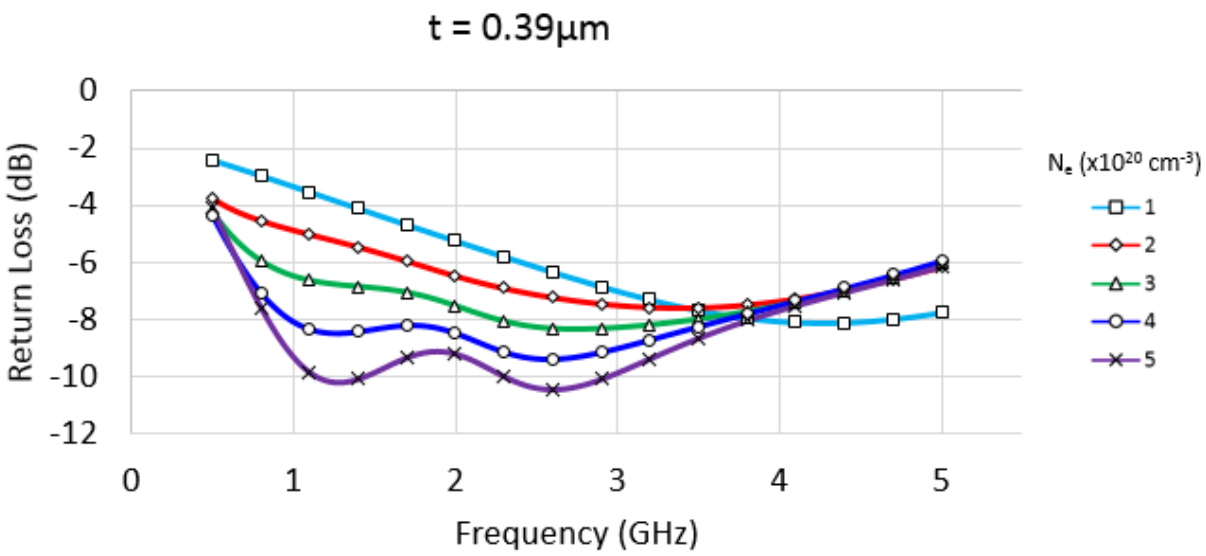

Figure A. 13 Return Loss of hourglass antenna at t = 0.39µm

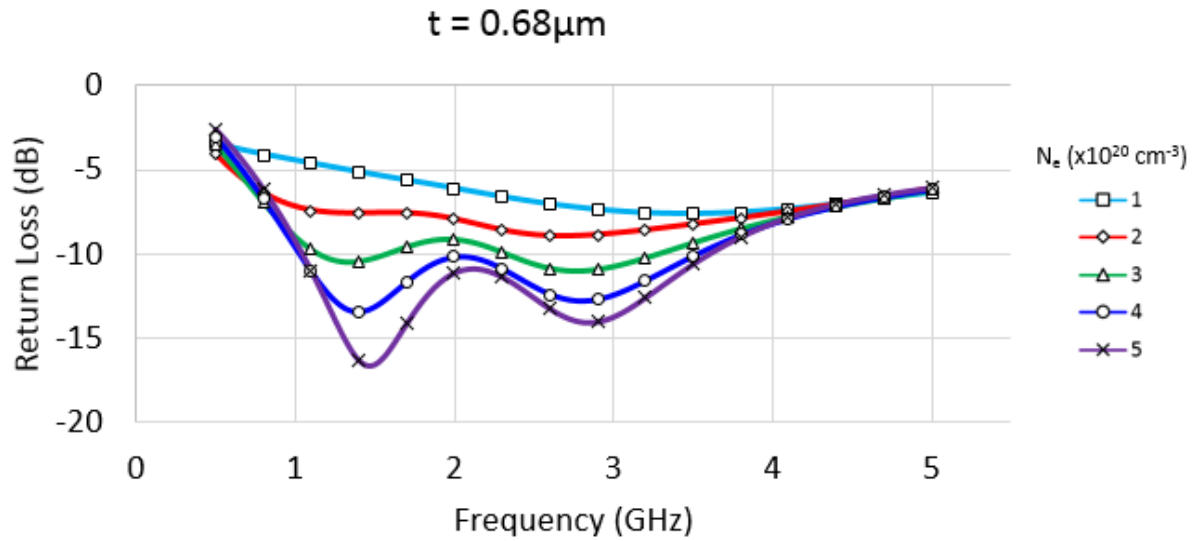

Figure A. 14 Return Loss of hourglass antenna at t = 0.68µm

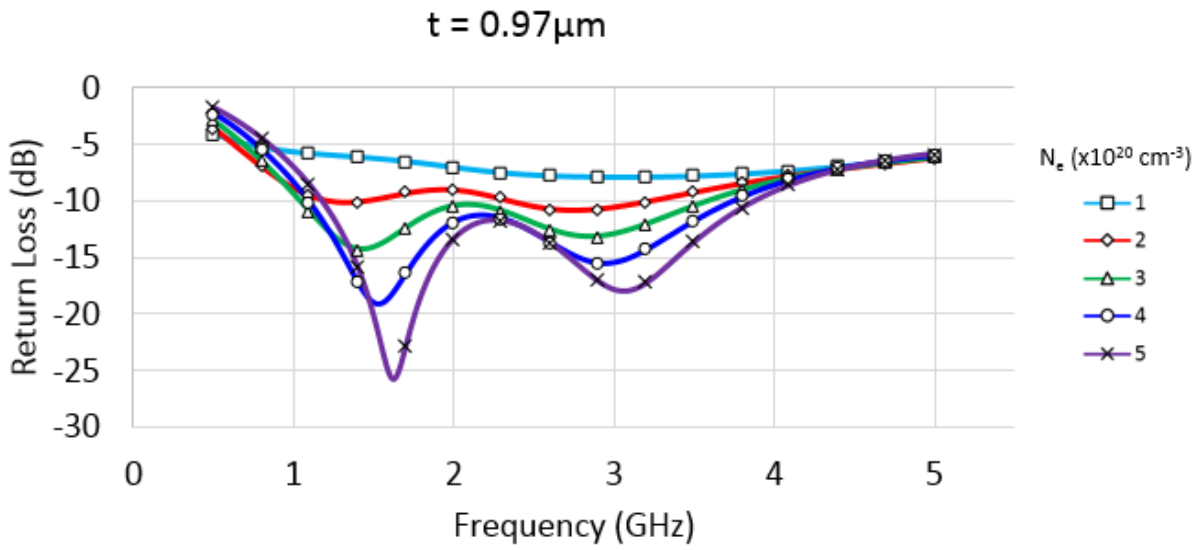

Figure A. 15 Return Loss of hourglass antenna at t = 0.97µm

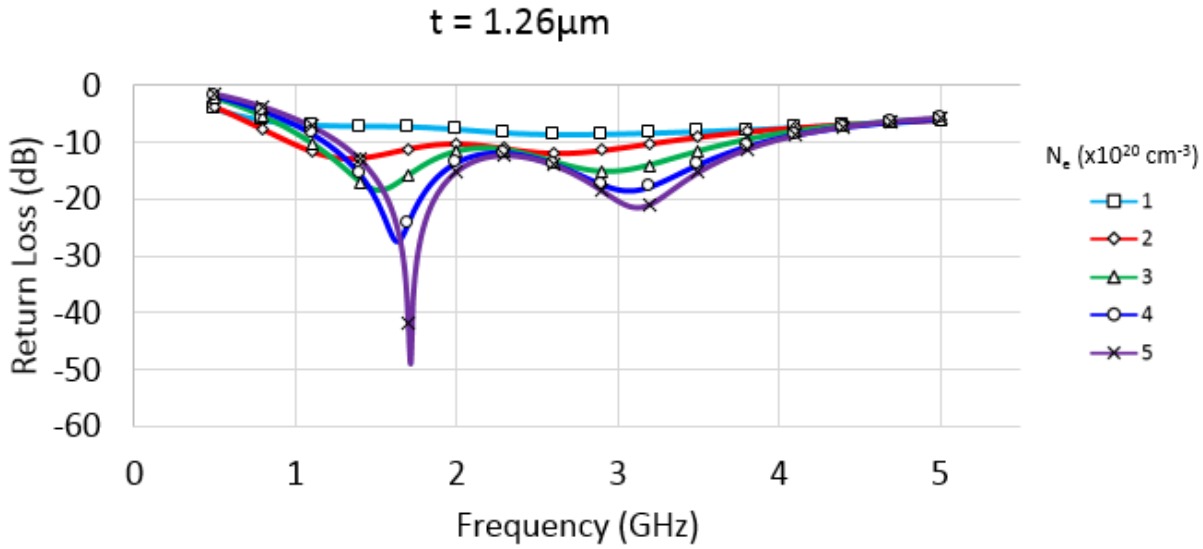

Figure A. 16 Return Loss of hourglass antenna at t = 1.26µm

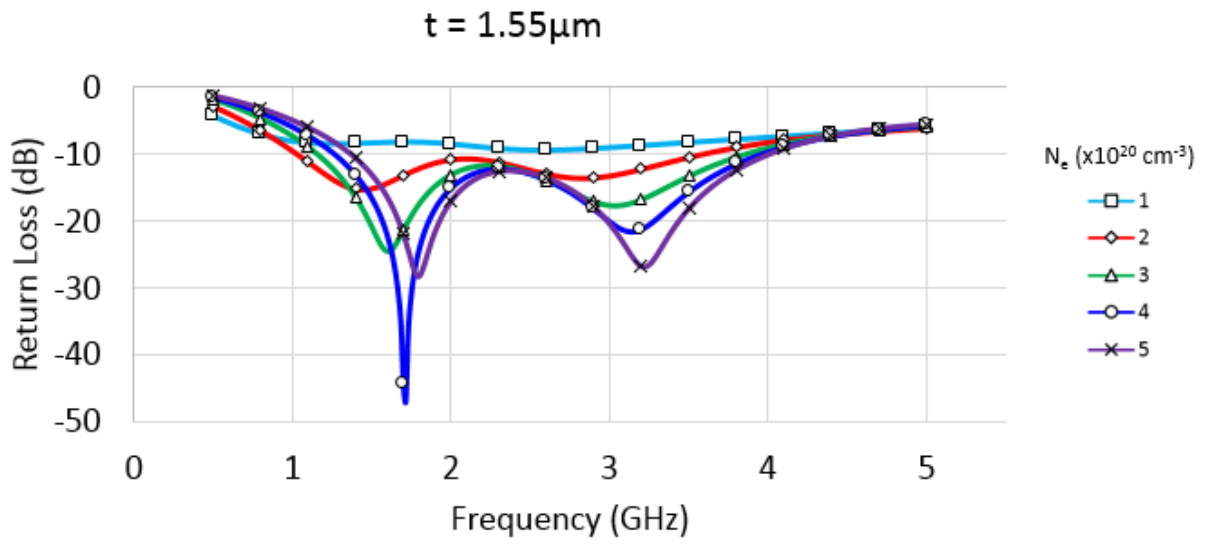

Figure A. 17 Return Loss of hourglass antenna at t = 1.55µm

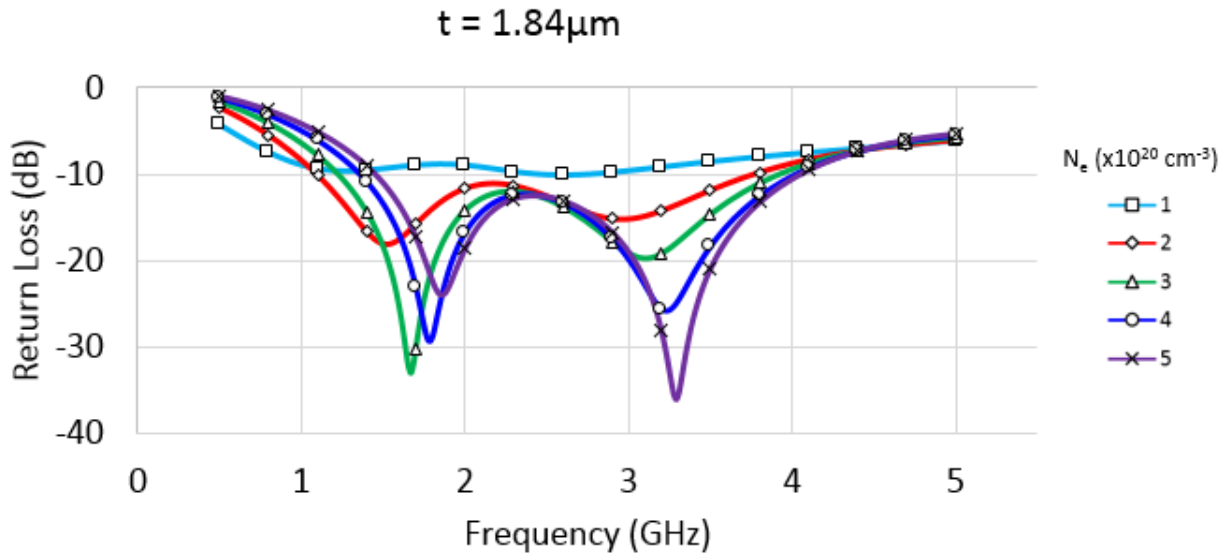

Figure A. 18 Return Loss of hourglass antenna at t = 1.84µm

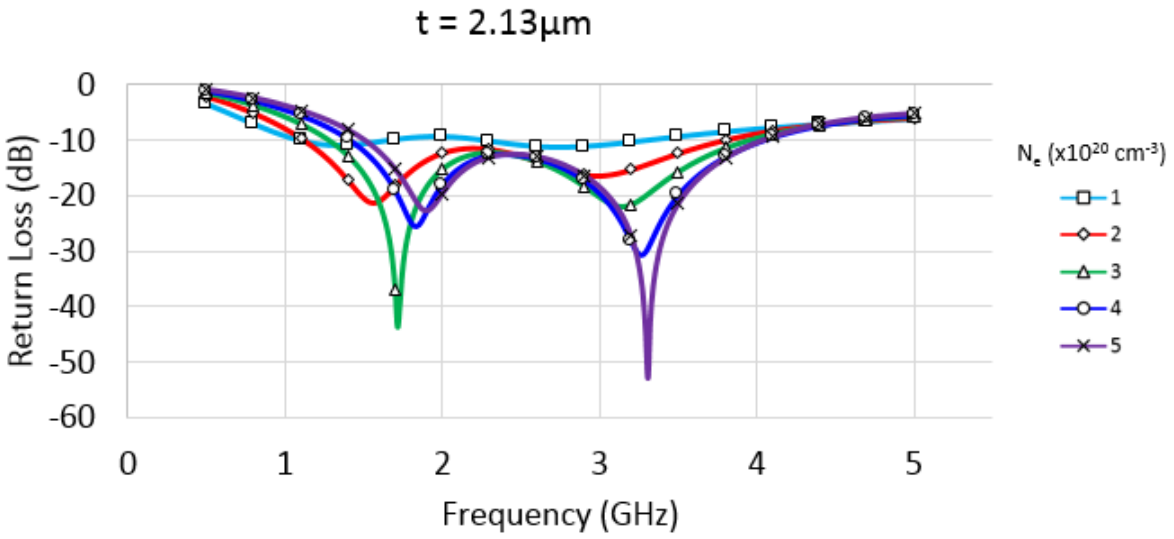

Figure A. 19 Return Loss of hourglass antenna at t = 2.13µm

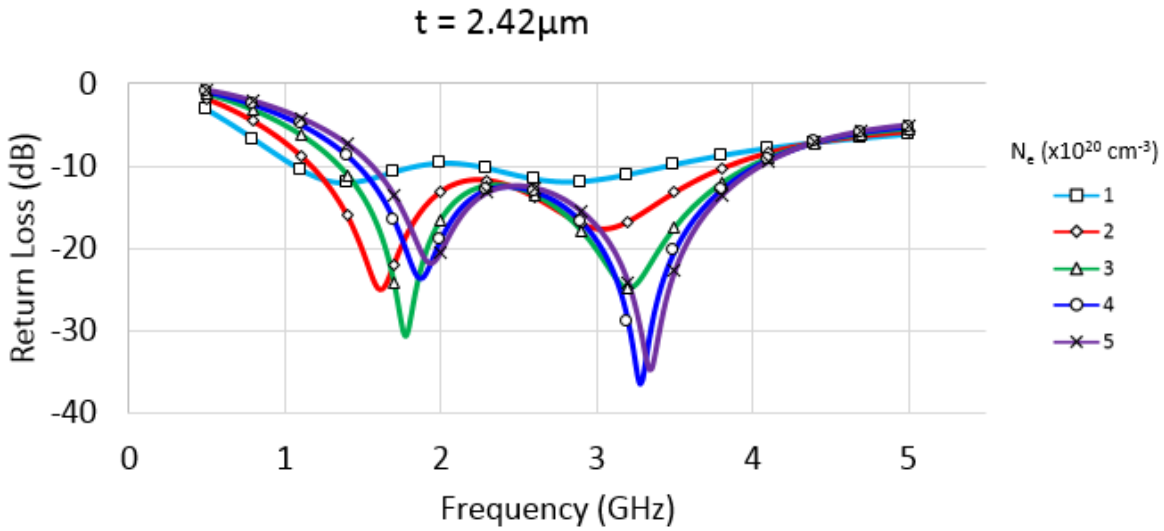

Figure A. 20 Return Loss of hourglass antenna at t = 2.42µm

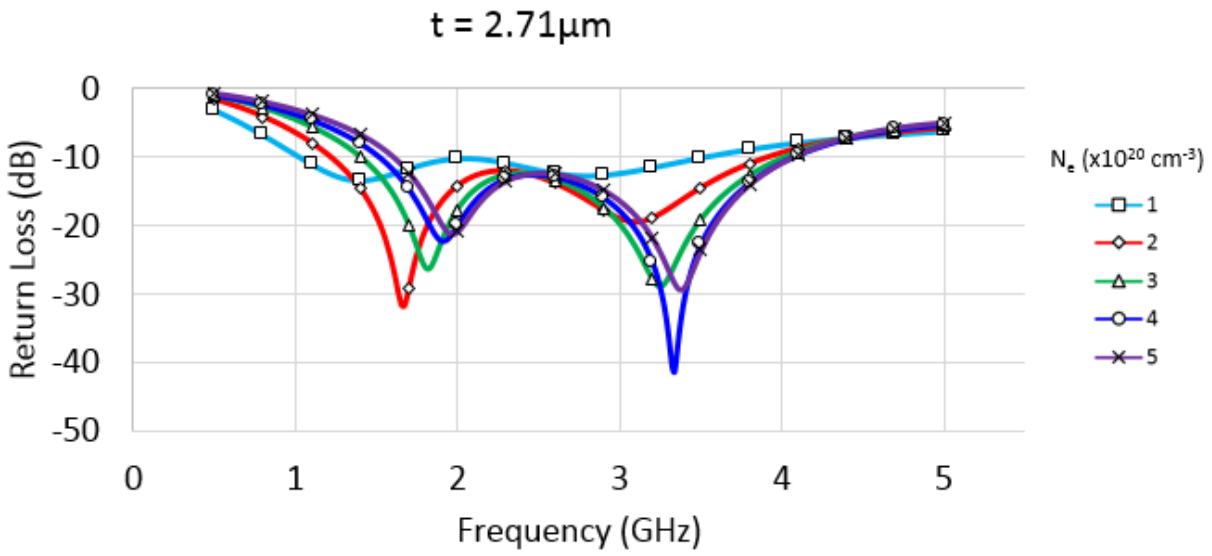

Figure A. 21 Return Loss of hourglass antenna at t = 2.71µm

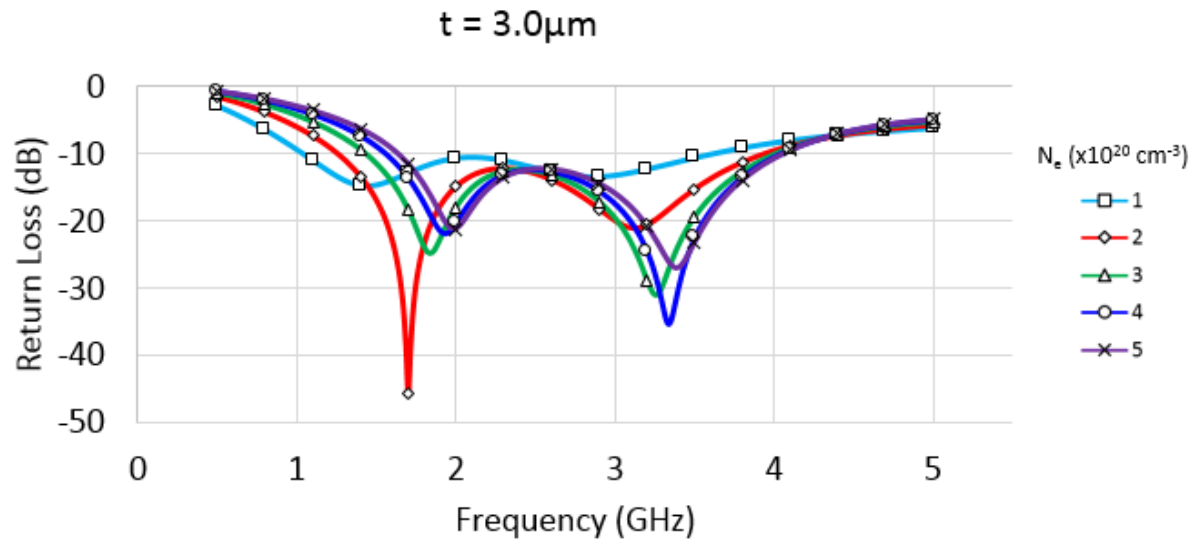

Figure A. 22 Return Loss of hourglass antenna at t = 3.0µm

A.3 Bowtie Slot

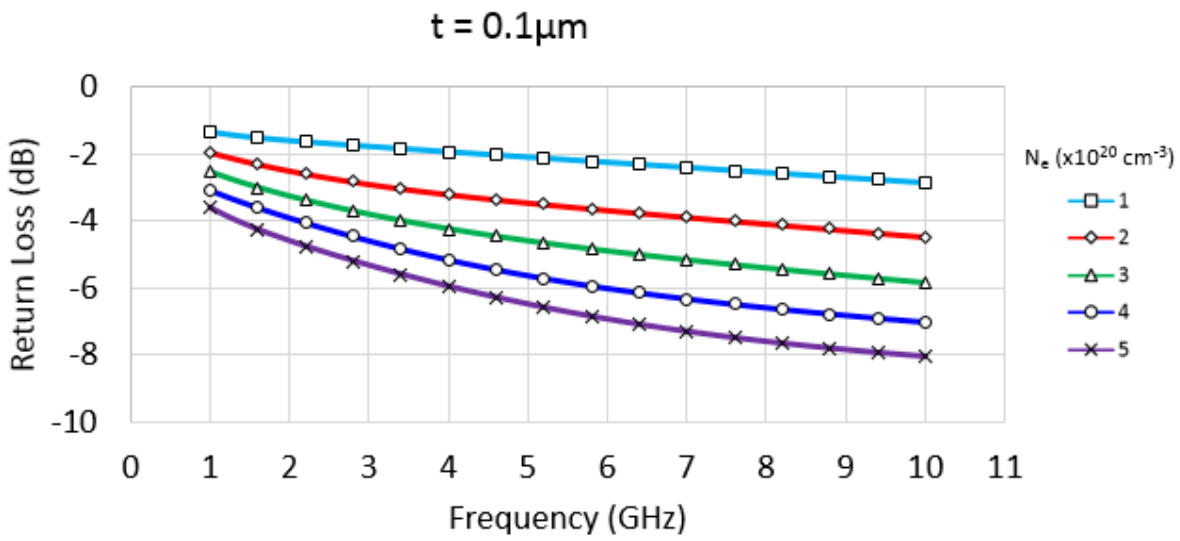

Figure A. 23 Return Loss of bowtie slot antenna at t = 0.1µm

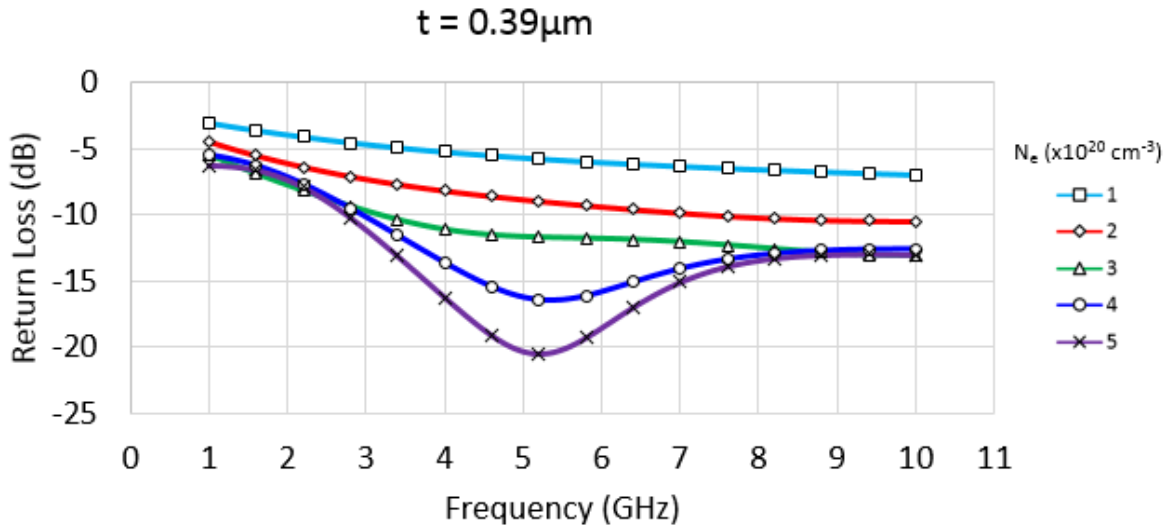

Figure A. 24 Return Loss of bowtie slot antenna at t = 0.39µm

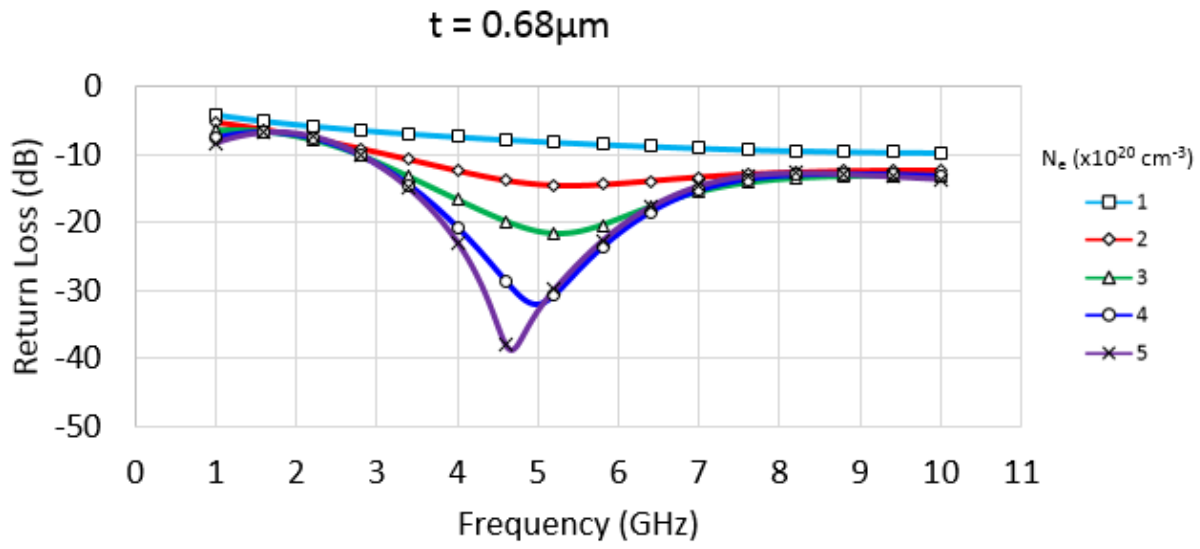

Figure A. 25 Return Loss of bowtie slot antenna at t = 0.68µm

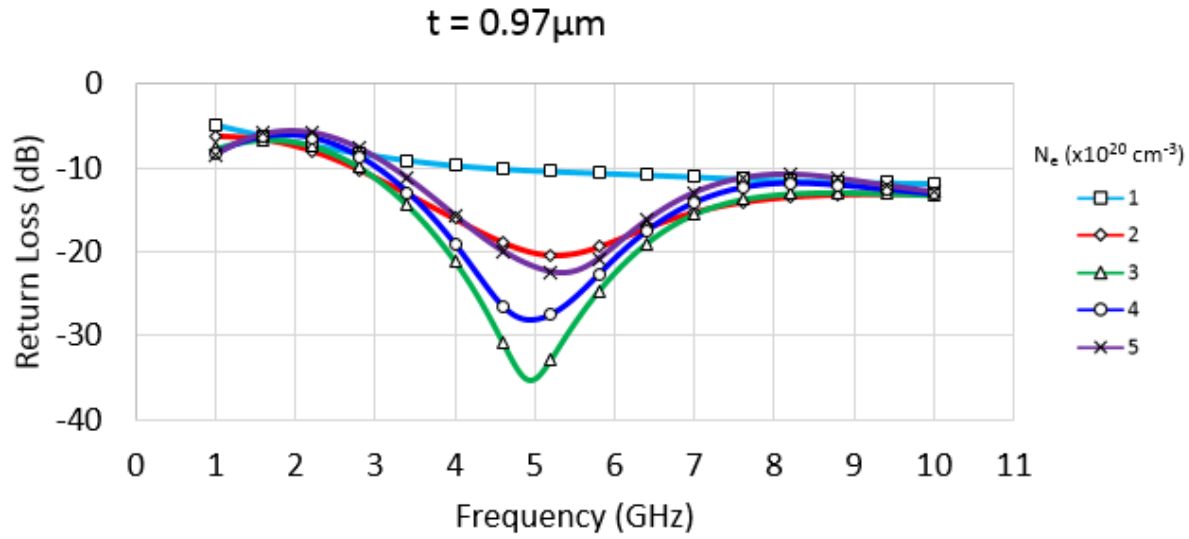

Figure A. 26 Return Loss of bowtie slot antenna at t = 0.97µm

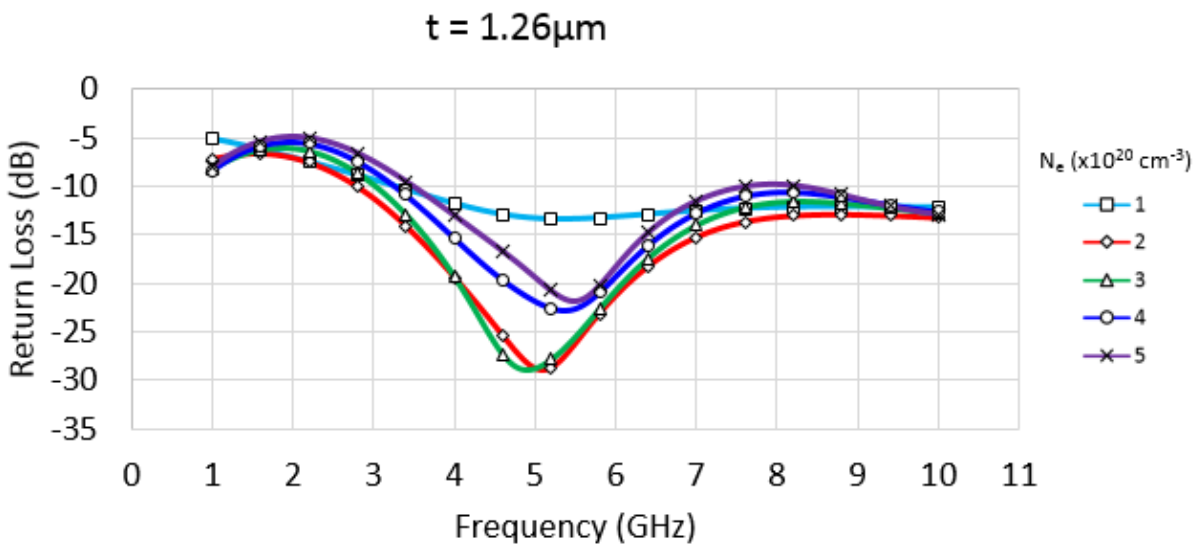

Figure A. 27 Return Loss of bowtie slot antenna at t = 1.26µm

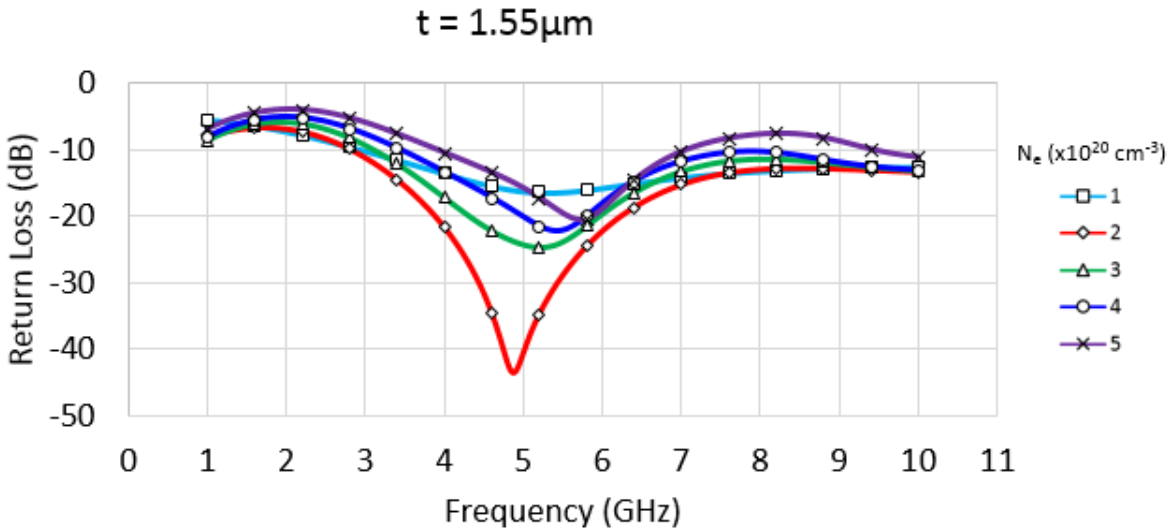

Figure A. 28 Return Loss of bowtie slot antenna at t = 1.55µm

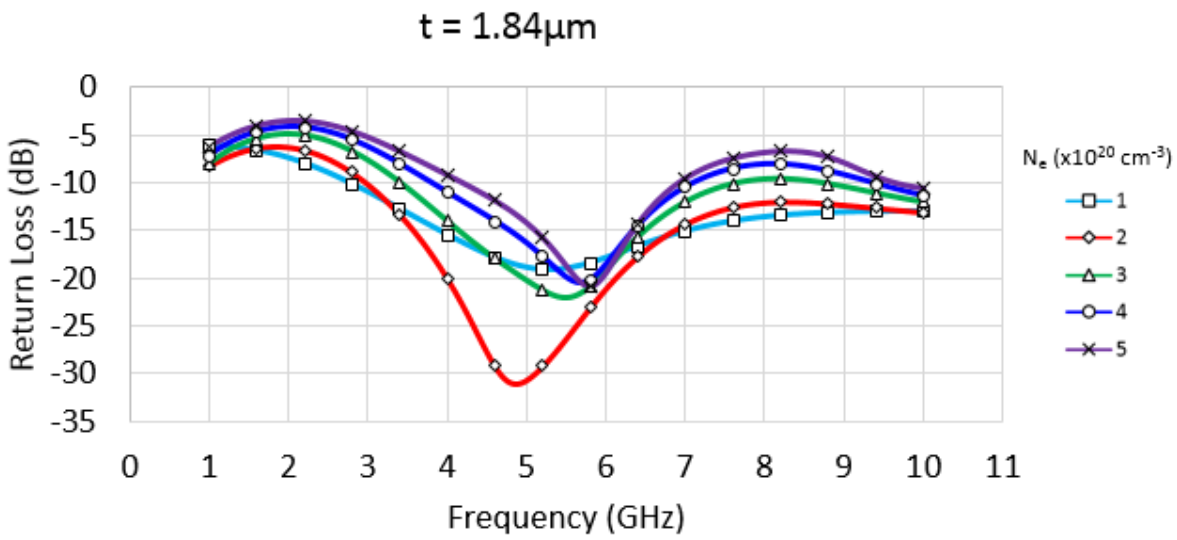

Figure A. 29 Return Loss of bowtie slot antenna at t = 1.84µm

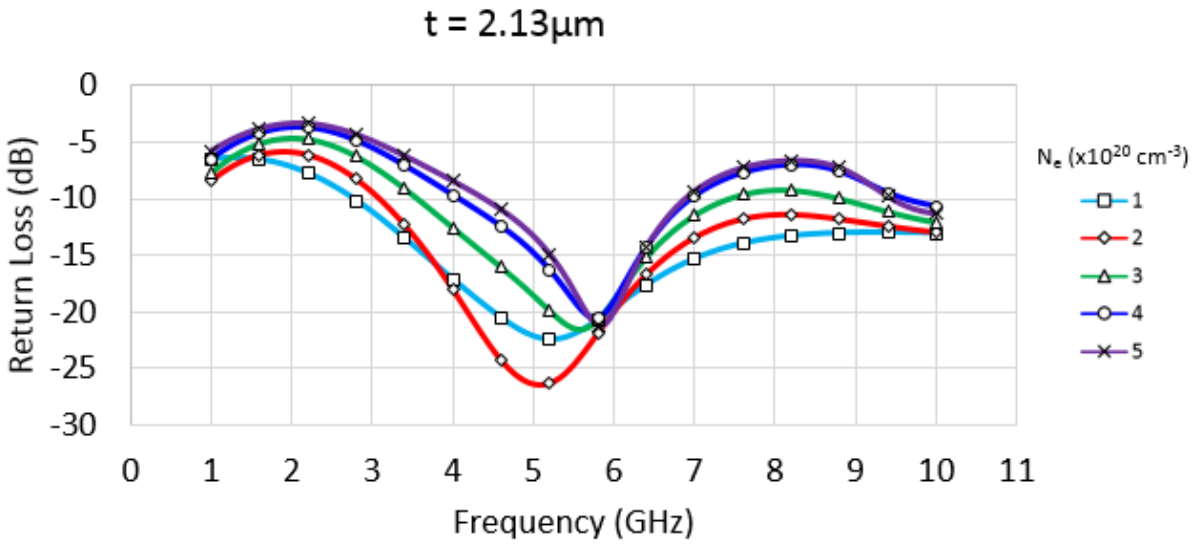

Figure A. 30 Return Loss of bowtie slot antenna at t = 2.13µm

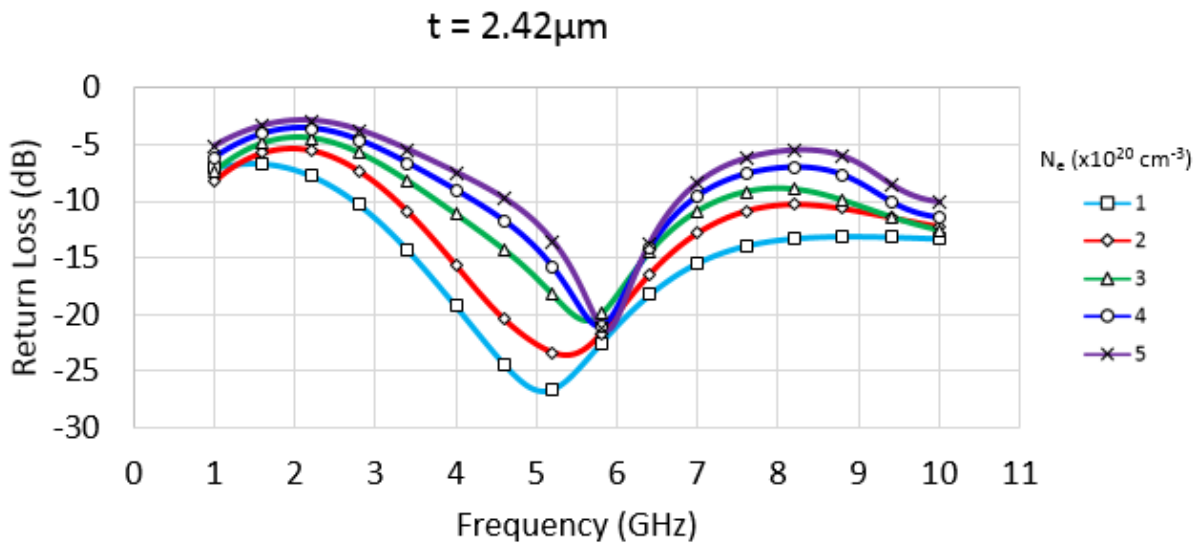

Figure A. 31 Return Loss of bowtie slot antenna at t = 2.42µm

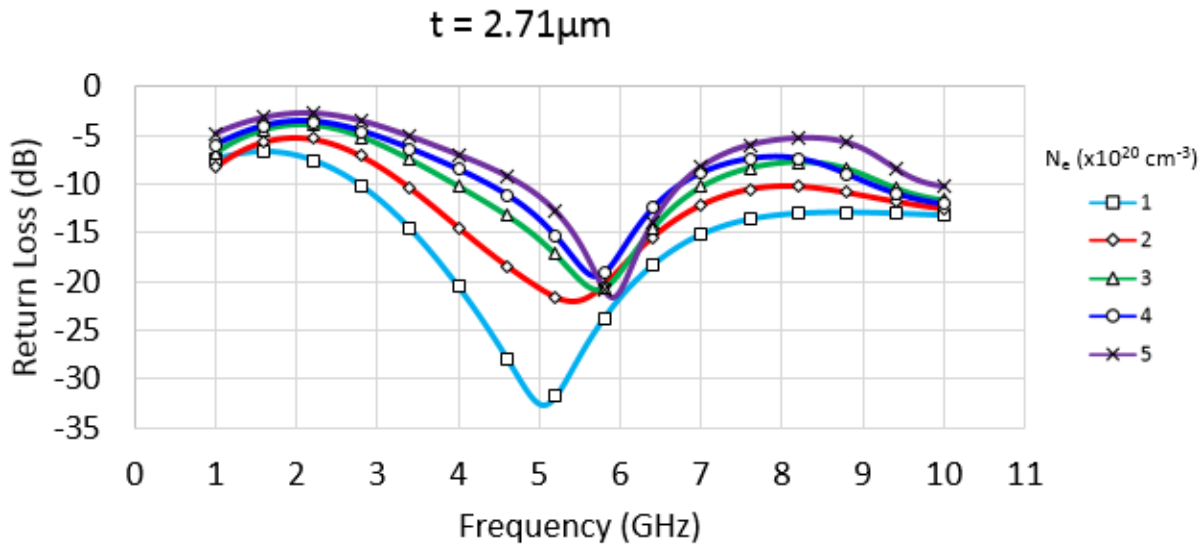

Figure A. 32 Return Loss of bowtie slot antenna at t = 2.71µm

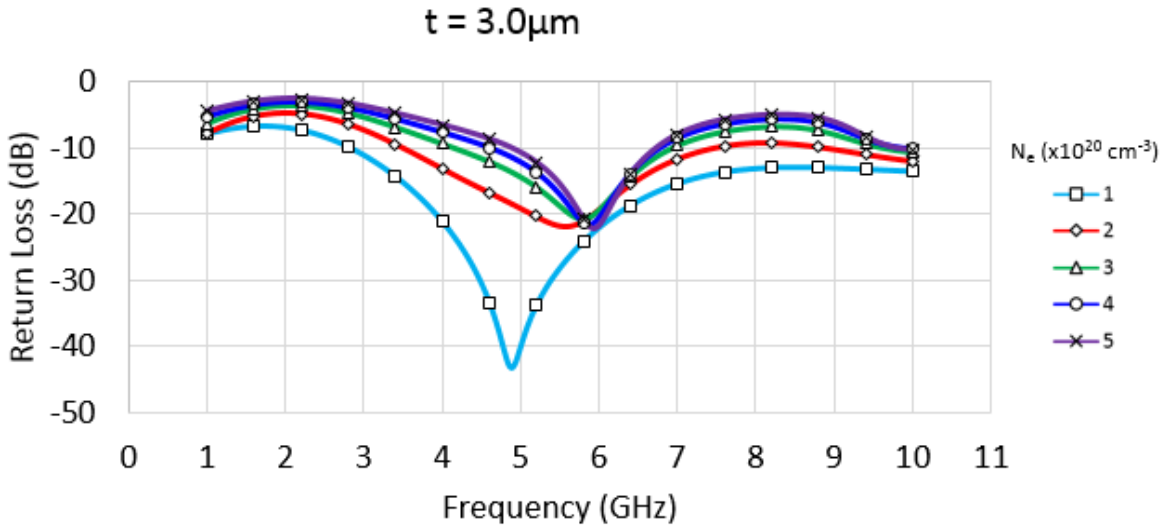

Figure A. 33 Return Loss of bowtie slot antenna at t = 3.0µm